University of Bath

UNIVERSITY OF
BATH

PHD

Determination of the thermal properties of materials utilising remote sensing techniques

Tytler, Duncan G. F.

Award date:
1995

Awarding institution:
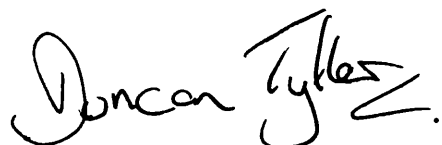University of Bath

Link to publication

DETERMINATION OF THE THERMAL PROPERTIES OF MATERIALS UTILISING REMOTE SENSING TECHNIQUES

Submitted by Duncan G.F. Tytler
for the degree of
Doctor of Philosophy
of the University of Bath
1995

COPYRIGHT

UMI Number: U539306

UMI

Dissertation Publishing

UMI U539306

ProQuest

Abstract

An experimental configuration, based around a Nd:YAG laser and a spectrograph/CCD combination, has been designed and constructed so that axially symmetric temperature distributions can be generated and measured remotely. The ability to accurately measure the spatial temperature distribution without physical contact to the sample is of importance to many areas of modern physics. The necessary physics and mathematics behind the conversion from the generated hot-spot's recorded spectral and spatial distribution to its corresponding radial temperature distribution is described.

The accuracy of the remote temperature measurement system has been validated by reproducing the spatial temperature distribution of a back-illuminated pinhole. When a NPL calibrated white light source is placed behind a pinhole, the spatial temperature distribution is analogous to a top hat shaped distribution with the peak temperature equal to the colour temperature of the lamp. By analysis of the measured temperature profiles produced by laser heating a polycrystalline iron sample, the melting point of the material was measured to be 1775 ± 29 K, which is comparable to the recommended value of 1808 K. Similarly, the melting point of polycrystalline uranium dioxide was measured to be 3120 ± 46 K, which equates to the recommended value.

A novel method involving nonlinearly fitting the measured radial temperature profile to a profile generated by a finite element analysis program, used to determine the thermal coefficients relating to the thermal conductivity of the sample, is discussed. Using this method, the measured thermal conductivity temperature dependence of the ceramic Pyroceram is presented, which agrees with the Thermophysical Properties Research Centre's (TPRC) recommended values. Finally, a technique for isolating the effects of external influences, such as pressure, on the heat conduction mechanisms is described.

Contents

II   Measurement of Thermal Properties.   77

5 Thermodynamical Analysis.   78

List of Figures

List of Tables

Acknowledgements.

I would like to thank the following people for their help and encouragement on this project:

- George Saunders, for his supervision and support.

- AEA Harwell, for financing the project, and for the valuable contributions of their Theoretical Studies department, especially Tony Harker.

- Dave Ladds, for his help in setting up the apparatus and development of the OMA2T analysis program.

Chapter 1

Introduction.

Knowledge of the temperature dependences of the thermal parameters, in particular the specific heat capacity, thermal expansion and thermal conductivity, is of fundamental significance to the understanding of the macroscopic and microscopic physics of materials.

- The specific heat capacity (C_p) reflects the overall energetic state of the energy levels, and hence characterises the density-of-states of the quasi-particles associated with the material, such as electrons, phonons, polarons and magnons.

- The coefficient of thermal expansion[1] is closely related to other thermal parameters, especially the specific heat capacity. When the thermal expansion (α_{cte}) is considered alongside the specific heat capacity, information relating to the lattice vibrations and bond strengths can be deduced.

---

[1]The thermal expansion is normally represented by the symbol α, but to avoid confusion with the thermal diffusivity, the symbol α_{cte} will be used.

- The thermal conductivity (κ) provides information relating to the scattering mechanisms of electrons, phonons and other quasi-particles.

When experimental values of all three of these thermal properties are known for any particular sample, reasonable predictions of the material's behaviour under heating can then be confidently made. For some materials, the environments in which they are expected to operate demand that the material is characterised to the extremes of temperature and pressure. The ability to characterise a material by making measurements of the thermal properties non-destructively and remotely has therefore become of interest to certain areas of industry, especially where the materials in question are used in hazardous environments. The measurement of the coefficient of thermal expansion can easily be modified to operate remotely [1], and the thermal conductivity (κ) and diffusivity (α) can also be measured remotely. Therefore, if the density (ρ) of a material is known, the specific heat capacity (C_p) can be calculated from the relationship:

$$\kappa = \alpha \rho C_p. \tag{1.1}$$

The measurement of the thermal conductivity alone is of great interest to the power generation industry, and the nuclear industry in particular. The reliability of any safety system lies in its ability to predict the course of an accident, so that preventative measures can be applied in time. In the prediction of a failure in the cladding of a nuclear reactor, the oxidation of the fuel pins would cause swelling [2] and a predicted reduction in the thermal conductivity [3], which in turn causes higher fuel temperatures. Higher fuel temperatures cause more oxidation, and a further reduced thermal conductivity, leading to a runaway sit-

uation. The upturn in the thermal conductivity [4,5] above 2000 K shown by un-irradiated, stoichiometric fuel may prevent this runaway *if* it is reproduced in the accident fuel pins. Therefore data obtained by remote measurement of the thermal properties of irradiated and oxidised fuels are among the many parameters required by the Health and Safety Executive (HSE) responsible for safety in the nuclear industry.

The properties of UO_2 have been much studied recently due to its importance as a nuclear fuel [6]. Uranium dioxide has the cubic fluorite structure as shown in figure 1.1, with the darker spheres representing the uranium ions. Other mate-
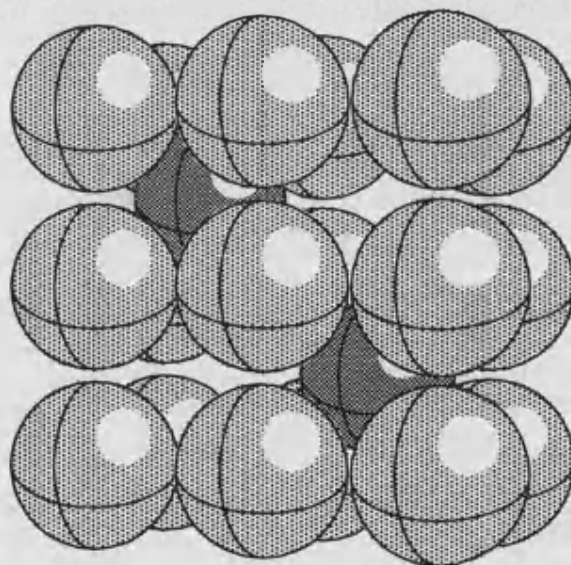
Figure 1.1: The fluorite structure.

rials which adopt this structure, such as strontium chloride ($SrCl_2$) and calcium fluoride (CaF_2 -fluorite), have been shown to undergo a transition to fast ion conductors at temperatures a few hundred degrees below their melting points [7]. This transition (the Bredig transition) is characterised by a lambda shaped peak in the specific heat capacity, or a sigmoid (S shape) in the enthalpy data [8].

Due to the high melting point (3120 K) of UO_2 compared to other members of the fluorite family, measurement of the specific heat capacity up to the melting point becomes inaccurate [9] at the highest temperatures, causing uncertainty as to the existence of fast-ion heat conduction in UO_2. The upturn in the thermal conductivity of UO_2 after 2000 K has been reproduced by molecular dynamics studies [10], after including a contribution to the heat conduction by small polarons, but this modelling shows no signs of fast-ionic conduction around the melting point.

Uranium possesses a divalent oxide which exhibits properties belieing its simple structure. At low temperatures, UO_2 can be described as a Mott insulator [11], while at room temperature, it can be described as a poor semiconductor with a band gap of 2eV [12]. Although the thermodynamical properties of UO_2 may not be well understood [13,14], especially at high temperatures, investigations into the thermodynamic properties of more 'common' materials have resulted in a detailed understanding of their microscopic and macroscopic physical properties. A good example of such a 'common' material is silicon, which has received considerable attention due to its use in the semiconductor electronics industry. The thermal conductivity of silicon has been measured [15] from cryogenic temperatures, right up to its melting point ($T_m = 1685$ K). The temperature dependence of the thermal conductivity at low temperatures (below the Debye temperature ($\theta_D = 674$ K)) can be fitted by theory derived from consideration of the phonon relaxation times [16] for various scattering mechanisms. In a perfect single crystal at very low temperatures, the only scattering of phonons needed to be considered, would be the recoil of phonons off the 'walls' of the finite sized crystal. At higher temperatures, the effects of scattering by crystal defects [17] becomes

more dominant. This defect scattering, along with the scattering of phonons by other phonons, dominates the thermal conductivity temperature dependence at medium temperatures for most materials, not just silicon. However, at high temperatures $(T > \theta_D)$, the thermal conductivity of silicon diverges from a theoretical dependence which assumes only lattice effects, and this divergence can be explained by the scattering of phonons off thermally excited electrons and electron-hole pairs.

In the high temperature region, the dependence of the thermal conductivity of silicon is comparable to that shown by metals [18]. Analysis of the thermal conductivity of metals normally makes use of the empirical law of Wiedemann-Franz [19], which is derived from an assumption that *all* the thermal 'current' is carried by conduction electrons, not phonons. Even though this analysis (based on the Drude theory of metals) is not completely accurate, the high temperature dependence of the thermal conductivity of metals [20] closely resembles that predicted by the Wiedemann-Franz law, due to the dominance of electron heat conduction [21] over phonons by an order of magnitude.

As the contribution by conduction electrons to the total thermal conductivity of metals can be modelled simply, the pressure dependence of the thermal conductivity provides an alternative method for studying the phonon anharmonicity of a metal. The pressure dependence of the electron contribution[2] can be obtained from the high temperature Bloch-Grüneisen expression [22], and when subtracted from the total thermal conductivity, the pressure dependence of the lattice con-

---

[2]Not to be confused with the *electronic* contribution κ_{elec} which relates to small polaron-phonon interactions.

tribution remains. This pressure dependence can be shown [21,23] to be related to the thermodynamic Grüneisen parameter. The Grüneisen parameter (γ_{th}) is related to the other thermal parameters, the specific heat capacity (C_p) and the coefficient of thermal expansion (α_{cte}), by the equation,

$$\gamma_{th} = \frac{3 B_m \alpha_{cte}}{C_p}, \tag{1.2}$$

where B_m represents the isothermal bulk modulus.

Conventional techniques for measuring the thermal conductivity of materials require some form of physical contact to be maintained with the sample [24]. This criterion has restricted the investigation of the effects of pressure on the thermal conductivity to the moderate pressures (maximum 2 GPa [25]) obtainable using conventional Bridgeman anvil cells. The thermophysical properties of materials at extreme pressures (2 Mbar, 200 GPa) are of interest to scientists, especially geophysicists, as the properties of materials at these pressures cannot be confidently extrapolated from lower pressure data due to the dramatic change the applied pressure has on the energetics of a material [26].

To generate the extreme pressures required by geophysicists, a diamond anvil cell must be used [27], which makes the measurement of properties which require electrical contacts impracticable. A group in Berkeley, led by Raymond Jeanloz, have had limited success in measuring electrical properties [28] using specialised gaskets containing the electrical contacts, and using a laser to heat a silicate perovskite sample $((Mg_{0.88}Fe_{0.12})SiO_3)$, they measured the phase diagram of this perovskite to a pressure of 127 GPa (1.3 Mbar) [29].

In this thesis, an experimental apparatus capable of remotely heating samples, and measuring the generated temperature distributions remotely is described in chapter 2. After construction of this apparatus from its individual components, the accuracy of the system as a whole and the subsequent computer analysis was tested by measuring the spatial temperature distributions of known sources (section 4.2). By subsequently analysing the radial temperature profiles generated on the test sample by the Nd:YAG heating laser, the melting points of polycrystalline materials can be remotely determined (section 4.5). Using a finite element analysis program to reproduce the radial temperature profiles from the given thermal properties, a method for determining the temperature dependence of the thermal conductivity from the measured radial temperature profiles is described in section 5.4. This apparatus has been constructed in such a way that all measurements can be undertaken remotely, and therefore the apparatus is ideally suited to diamond anvil cell work. With the methods for remotely determining the thermal conductivity detailed in chapter 5 of this thesis, it will become apparent that the measurement of the thermodynamic properties of materials under extreme pressures is now possible.

Part I

Development of the Techniques and Equipment Necessary to Measure Temperature Profiles Remotely.

Chapter 2

Experimental hardware design of the laser heating and detection systems.

The abilities to heat a sample remotely, or to measure the temperature of a sample remotely are both, on their own, very useful techniques in modern science. Combining both these abilities produces a powerful tool for remotely investigating the high temperature properties of materials.

Using a focused laser beam to remotely generate a 'hot-spot' on a sample, the radiation emitted from the 'hot-spot' is monitored by a CCD based spectral detection system, and the recorded data array can then be subsequently analysed. The apparatus shown in figure 2.1 can be separated into two major parts, namely the heating system based on an infra-red solid state laser, and the detection system based around the spectrograph-CCD combination. In between these two main stages, the invisible laser beam is steered firstly by a gold coated copper-nickel
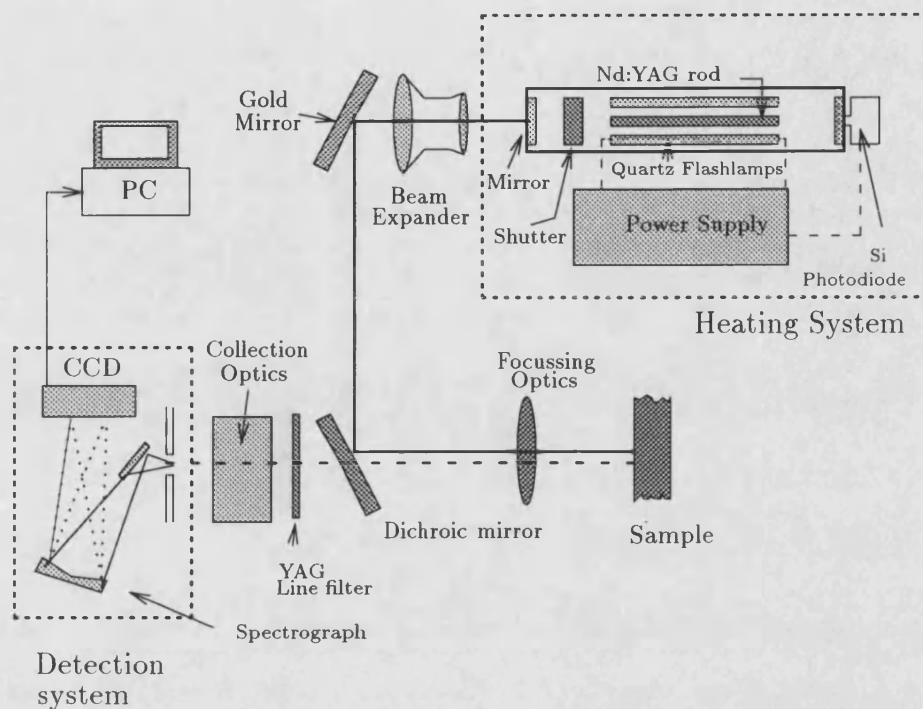
Figure 2.1: Diagram of the experimental apparatus.

mirror and then by a dichroic mirror to the focusing optics, which in turn focuses the laser beam onto the front face of the sample. The thermal radiation emitted from the front face of the sample by the laser generated hot spot is focused onto the entrance slit of the spectrograph by the collection optics. The emitted radiation is not reflected back towards the solid state laser as the dichroic mirror is designed to operate so that it reflects the infra-red laser radiation like a normal mirror, whilst allowing the visible radiation emitted from the sample to be transmitted through to the detection system. It is the wavelength and spatial distribution of the light emitted from the laser heated sample which is required for the subsequent analysis to produce a temperature profile.

2.1 The heating system.

There are many ways to heat a sample, which can vary from electrical resistive heating to gas burners. The object of this experiment is to investigate samples contained in isolated environments; therefore a non-contact method of heating is required. This criterion restricts the method of heating the sample to either inductive heating or the use of lasers.

The heating system we are employing is a solid state laser operating in the near infra-red part of the spectrum. Whilst this radiation is invisible to the human eye, conventional optics can still be used to focus the beam. However, there are several restrictions inherent in the use of lasers of this power which will be discussed later in section 2.4.

2.1.1 Laser heating.

Over the last decade, neodymium doped yttrium aluminum garnet (Nd:YAG) solid state lasers have been improved in terms of their output power and reliability, mainly in response to pressure from industry where they are used as welders. The laser used in our apparatus is a Quantronix series 100, continuous wave (CW) Nd:YAG laser, with a maximum rated power output of 32 Watts in the multimode configuration, or 16 Watts in the fundamental TEM_{00} mode. One modification from the standard model that has been made, is that a feedback system has been added to stabilise the power output. The effect of this on the
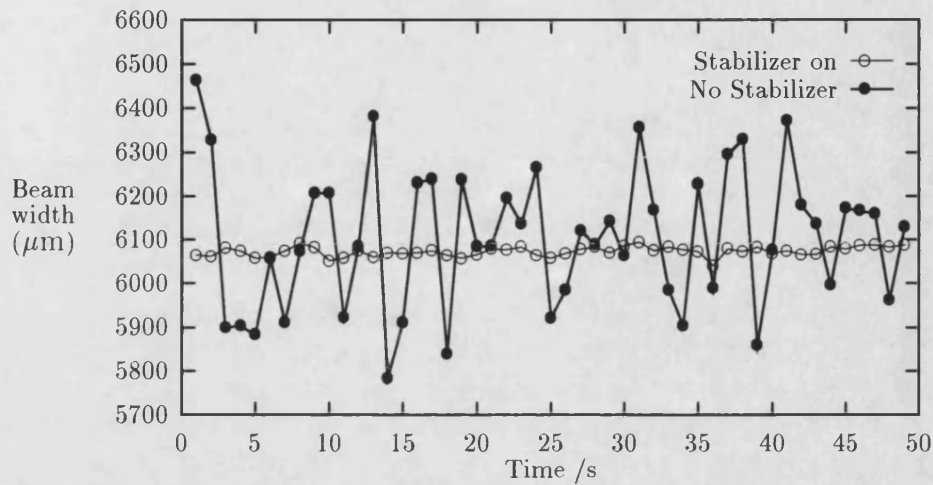
Figure 2.2: Effect of the stabiliser on the laser's TEM$_{00}$ Gaussian beam width.

beam width is shown in figure 2.2, where the operation of the stabiliser can reduce the standard deviation of the Gaussian beam width from 0.026% to 0.00175%, which equates to a fifteen-fold improvement.

2.2   Optics.

2.2.1   Laser focusing optics.

The sample depicted in figure 2.1 is mounted at the focal point of the focusing optics, which is a multi-element lens. The laser beam will therefore be focused to a point with a minimum radius (ω_0) which can be determined by Gaussian optics [30, 31]:

$$\omega_0 = \frac{4\lambda F}{2\pi D}.$$ (2.1)
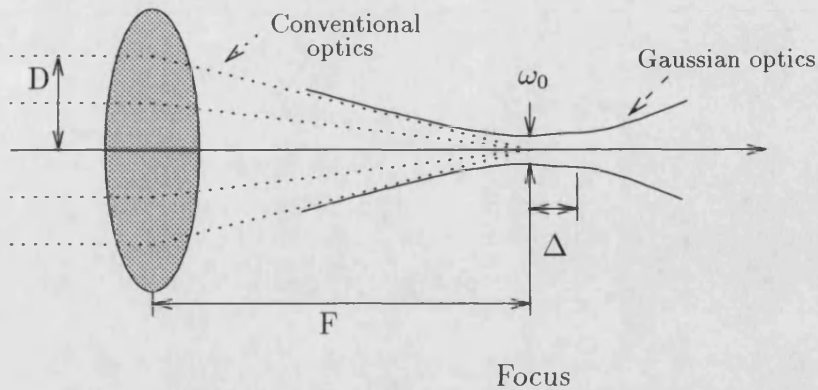
Figure 2.3: Gaussian optics compared to the conventional approach of ray tracing.

The symbol D in equation 2.1 represents the width of the beam entering the focusing lens, which can also be referred to as the effective aperture. The beam emitted from the laser cavity has a diameter of 0.4mm which is determined by the size of the exit aperture situated in front of the mirror. Using this value of D, and substituting in the values of the focal length of the lens ($F = 70$mm) and the wavelength of the laser radiation ($\lambda = 1.064\mu$m), we can calculate from equation 2.1 the expected beam waist (ω_0) of the laser beam projected onto the sample surface:

$$\omega_0 = \frac{1}{2} \cdot \frac{4 \times 1.064 \mu m \times 70 \text{mm}}{\pi \times 0.4 \text{mm}} = 118.5 \mu \text{m}. \tag{2.2}$$

This beam waist can be decreased by introducing a 10:1 beam expander into the position shown previously in figure 2.1. This results in the beam waist being reduced by a factor of ten as the effective aperture of the focusing optics is increased by a factor of ten with the introduction of the beam expander.

From figure 2.3 we can see that the beam takes on a parallel character close to the focus. Using Gaussian optics we can calculate a quantity called the depth of field (Δ) which is a measure of the distance from the focus that the beam width

becomes equal to $\sqrt{2}\omega_0$.

$$\Delta = \frac{8\lambda}{\pi} \cdot \left(\frac{F}{D}\right)^2 = 829.8\mu\text{m}. \tag{2.3}$$

The value calculated in equation 2.3 is quite large when compared to the sample size, so the heating of the sample can be considered to be uniform in radius through the depth of the material.

2.2.2 Collection optics.

The 'hot-spot' generated on the sample will emit radiation in all directions, but we are only able to collect the light emitted in the direction of the incoming laser. This means that the light is collected first by the focusing lens, which results in a parallel beam of light being propagated back to the collection optics. Before the light reaches the collection optics, it passes through the dichroic mirror and a filter to remove any reflected laser light. These two steps do not alter the physical shape of the beam, but reduce the intensity of the beam due to absorption. In the case of the dichroic mirror, a non-uniform wavelength response is imposed on the spectral distribution of the light emitted from the sample. This nonlinear response will be illustrated subsequently in section 2.3.3, but first different optical configurations used for the collection optics are discussed below.

Circular lens.

The simplest of the collection optic system used comprises a single circular lens, as shown by figure 2.4. This was the configuration employed by Jeanloz [32] in
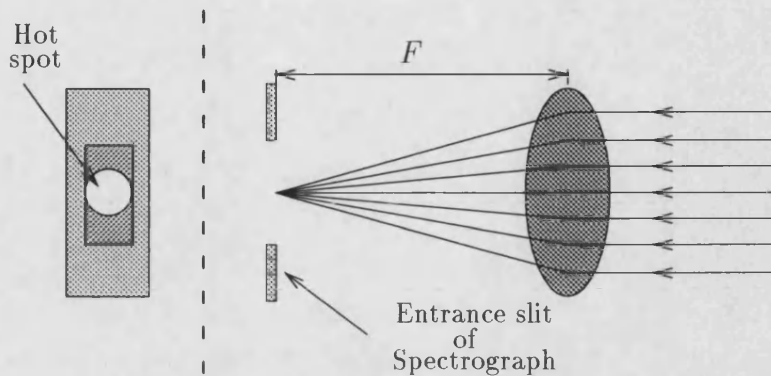
Figure 2.4: Circular lens used as the collection optics.

his original apparatus used to measure melting curves of upper mantle materials. The use of a single spherical lens results in a very bright spot, and minimises the absorption of light by the collection optics due to the use of only one lens. The major drawback of this system is that the height of the image recorded by the CCD is limited by the width of the entrance slit. It would be possible to make wider entrance slits, but then the effects of wavelength convolution (discussed in section 3.1) would make this approach impracticable.

Cylindrical lens.

The way that the spectrograph operates (described in section 2.3.1) means that it is possible to increase the spread of the spatial data without incurring any of the detrimental effects of wavelength convolution. This increase in the spatial resolution is achieved by careful design of the collection optics. In an ideal situation, we would have an image of the sample's hot-spot projected onto the entrance slit of the spectrograph so that it covers the whole height of the slit, and

(a) Plan view.   (b) '3D' view.
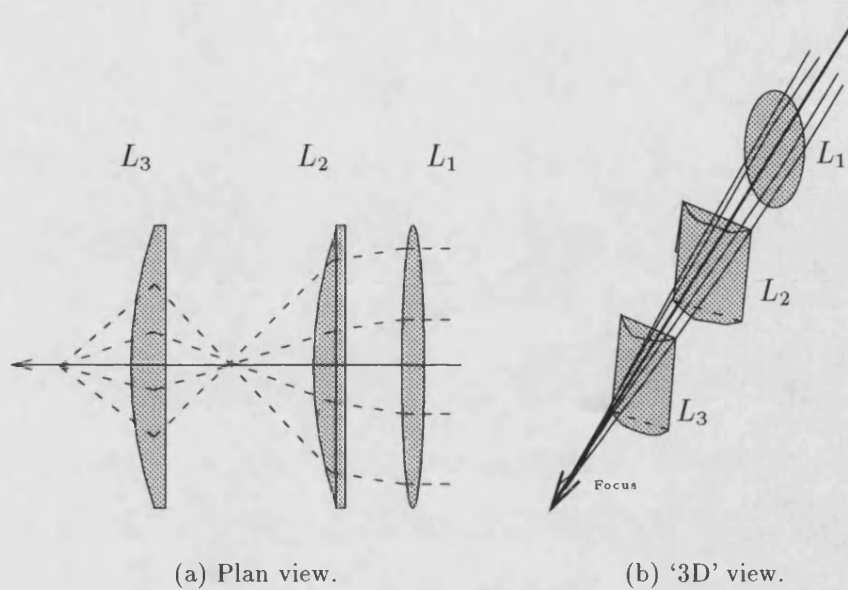
Figure 2.5: Layout of the collection optics using cylindrical lenses to focus the image.

ideally the image should be narrow enough to use as thin a slit as possible. If an optical design similar to that shown in figure 2.5 is used, then the ideal situation described above is approached, as the cylindrical lenses L_2 and L_3 squeeze the light into a line, while maintaining the height of the image produced by the long focal length circular lens L_1, which is required to produce an optical image of the 'hot-spot'.

Microscope objective.

If we take the reasoning for using cylindrical lenses one step further, we could expand the optical image produced by the circular lens (L_1 in figure 2.5a.) with a microscope objective lens to produce parallel light as demonstrated in figure 2.6. If the entrance slit is much narrower than the height of the image, then the sub-
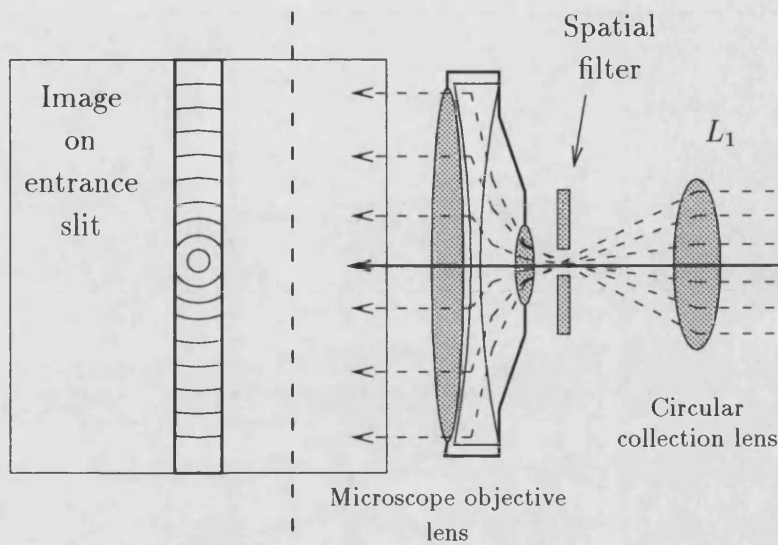
Figure 2.6: Layout of the collection optics using a microscope multi-element lens to focus the image.

sequent computer analysis is made easier by treating the recorded data as a slice section through the hot-spot. With a slice section rather than a complete disc, there is no need to implement the Abel inversion correction stage (section 3.3). However, the loss of light due to absorption in the microscope objective lens means that very intense hot-spots are required before this method can be implemented confidently.

The inclusion of the spatial filter shown in figure 2.6, is an optional step which could be employed to remove the effects of defects introduced in the manufacturing process of the focusing lens and surface defects on the mirrors. The reader should consult Hecht [33] for a further discussion on the use of spatial filters.

2.3   The optical detection system.

The detection system is designed to simultaneously collect and measure the spectral and spatial distribution of the radiation emitted from the surface of the sample. For this particular application the radiation is visible light, which enables us to take advantage of recent technological advances in the efficiency of silicon detectors, precision in the fabrication of charge coupled devices (CCD), and computer aided manufacturing of optical components as incorporated in the spectrograph.

2.3.1   The CCD detector array and spectrograph.

The workings of the spectrograph shown in figure 2.7, are hard to describe, and only marginally easier to visualise.

Let us consider the example of a 'hot-spot' emitting light; this light is focused down to a line incident on the entrance slit of the spectrograph by the system of cylindrical lenses as described earlier in section 2.2. This image on the entrance slit can then be thought of as divided into small segments equal in size to the height (23 μm) of the CCD pixels. The 'super-corrected' holographic grating in the spectrograph splits each of these segments into its spectral components, whilst retaining their spatial integrity, depicted in figure 2.8. The 2D data array of spatial position against wavelength data is then read from the CCD by the controlling computer via an IEEE interface. The data is then subsequently analysed

Focal plane

800nm

200nm

Adjustable
plane mirror

Super-corrected
holographic
concave grating

Image of sample

Entrance
slit
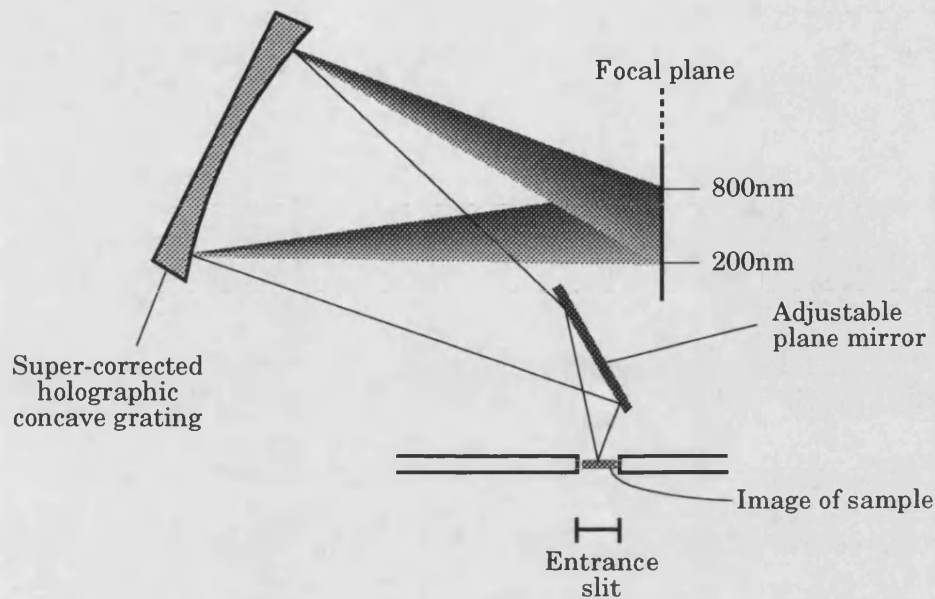
Figure 2.7: Schematic of the layout and optical path of the spectrograph.

using a FORTRAN program (OMA2T), outlined in section 3.6 of this thesis.

blue ← green → red

Spatial
position

← Wavelength →
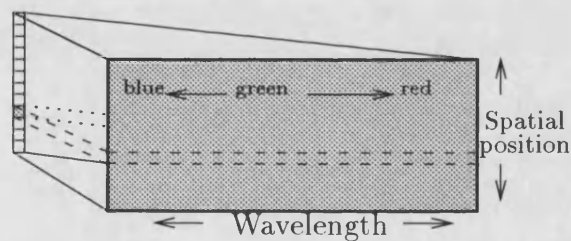
Figure 2.8: Spectral splitting of focused image.

The signal to noise ratio of semiconductor detectors can be vastly improved by operating the detector at low temperatures, preferably in the liquid nitrogen temperature region. This increased signal quality arises from the increase in electron mobility, in conjunction with a decrease in the thermal noise associated with the reduced ambient temperature.

For our application, it is not practical to operate the detector at liquid nitrogen temperatures, so the rear face of the CCD detector array is cooled with a Peltier cooler. To remove the heat generated by the *p-n* junction of the Peltier cooler, a continuous flow of chilled water is passed over the junction. As the Peltier cooler can reduce the temperature of the CCD to as low as -20°C, a continuous flow of oxygen free nitrogen is passed over the CCD's front face to prevent atmospheric moisture condensing, and forming ice crystals on the detector face.

2.3.2   Wavelength calibration of the spectrograph-CCD combination.

The manufacturers' of the spectrograph claim that the wavelength dispersion is linear, so in principle we could calibrate the system by measuring the spectrum of only two laser lines. To verify the manufacturers claims, we have measured the spectrum of a collection of laser and spectral emission lines which are listed in table 2.1.

Source	Wavelength /nm	Reference
Helium Neon laser	632.991	[34]
Mercury vapour lamp	435.956 546.227 577.119 579.226	[35]
Cadmium lamp	467.946 480.125 508.723 644.024	[35]

Table 2.1: Table of emission lines
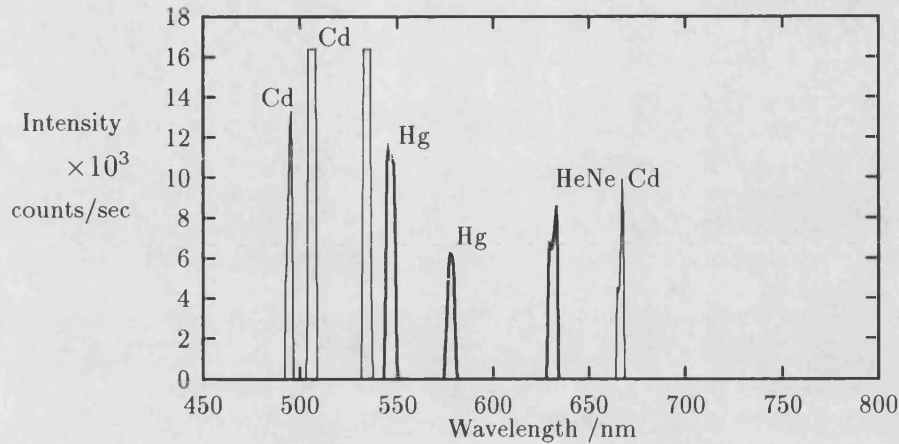
Figure 2.9: Wavelength calibration spectrum.

The spectra obtained are shown in figure 2.9, and can be fitted to a linear expression for wavelength against CCD pixel number with two adjustable parameters, namely the starting wavelength (λ_s) and the wavelength dispersion ($\Delta\lambda$).

$$\lambda = \lambda_s + (\Delta\lambda \times \text{pixel number}) \tag{2.4}$$

The expression which the OMA2000 software controlling the detector calculates is obtained by fitting the measured pixel positions to their tabulated wavelength values using a linear least squares analysis. The linear expression obtained can be written:

$$\text{Wavelength} = 447.296 \text{ nm} + 0.5797 \text{ nm} \times \text{ pixel number.} \tag{2.5}$$

The wavelength dispersion term ($\Delta\lambda$) agrees well with the manufacturers' specifications, which state a 190nm to 820nm wavelength range spread over 25mm. This equates to a dispersion of 0.5796nm compared to the measured value of 0.5797nm.
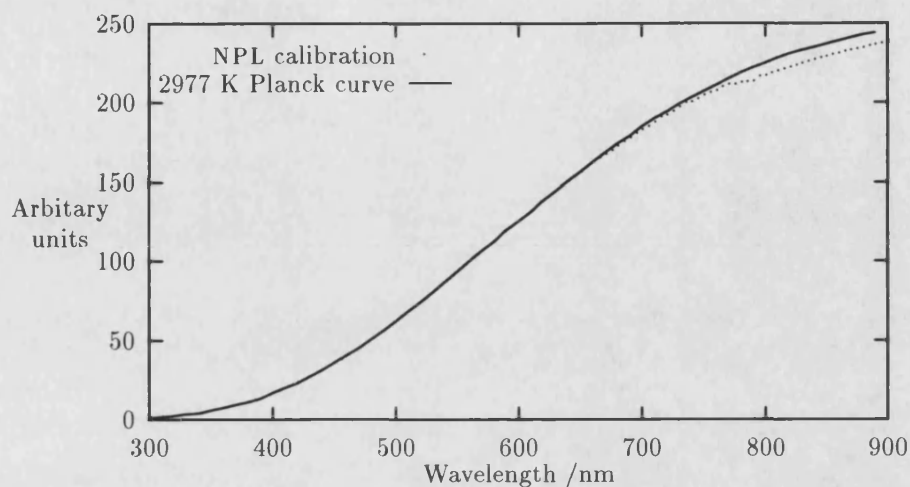
Figure 2.10: Comparison between the NPL calibration and the Planck curve.

2.3.3   Spectral response and correction.

Most optical components used in the apparatus absorb light, but it is the non-linear spectral absorption of light by the dichroic mirror and the spectrograph-CCD combination which dominates the shape of the spectral distribution as recorded by the CCD. To measure this wavelength dependent absorption, a white light source previously calibrated at the National Physical Laboratory (NPL) is positioned behind a pinhole situated where the sample would be mounted. The light emitted from the pinhole is collected by the CCD, and the system's spectral response curve is calculated by dividing the measured wavelength distribution of the tungsten lamp by the NPL calibrated curve [36] shown in figure 2.10. A series of spline coefficients are extracted from the obtained sensitivity correction factors shown in figure 2.11. To correct an obtained raw data set, the relevant sensitivity correction factor for any particular wavelength is calculated by inter-
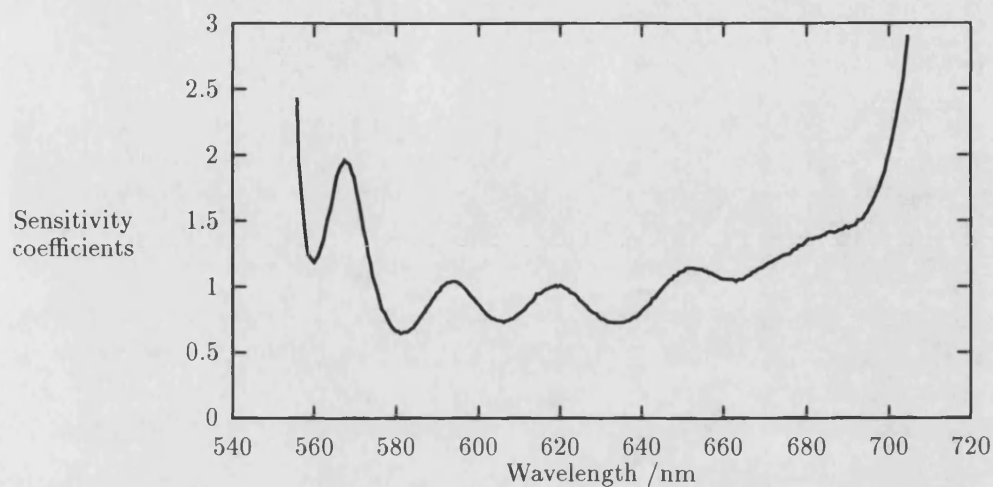
Figure 2.11: Sensitivity coefficients to correct for the system's spectral response by multiplication.

polation using the B-spline coefficients [37]. This method has been shown to be more computationally efficient than vector multiplying the 2D data set by a 1D matrix of precalculated sensitivity coefficients.

2.4 Safety considerations.

The Nd:YAG laser we are using is classed 4b according to the Health and Safety Executives guidelines. Because of this classification, there are certain restrictions on its location, and on its *modus operandum* that need to be observed.

One requirement is that the laser should be interlocked in such a way that it is impossible to walk into the laboratory when the laser is lasing. Legislation does not require that this interlock be 'latching' in design, but this was deemed
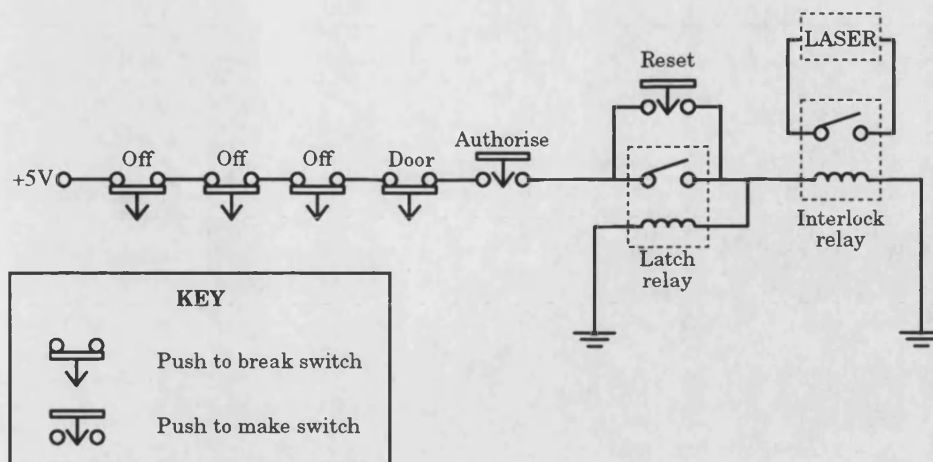
Figure 2.12: Laser safety interlock circuit.

a logical precaution, and can be seen included in the safety circuit shown in figure 2.12.

Other precautions include the wearing of safety goggles at all times that the laser flash lamps are illuminated, and not just when the laser is lasing, as the infra-red radiation emitted from the flashlamps can damage the retina of your eyes.

2.5 Sample mounts.

In figure 2.1, the sample is depicted as a free standing piece of material. This is only symbolic, as the samples are mounted in a specially designed 'gas chamber', christened the "Controlled Atmosphere Chamber" (CAC) and shown in figure 2.13. This piece of equipment ensures that an inert atmosphere can be maintained around the sample while it is being heated, thus preventing the sample oxidising or changing its stoichiometry. When experiments with hyper-
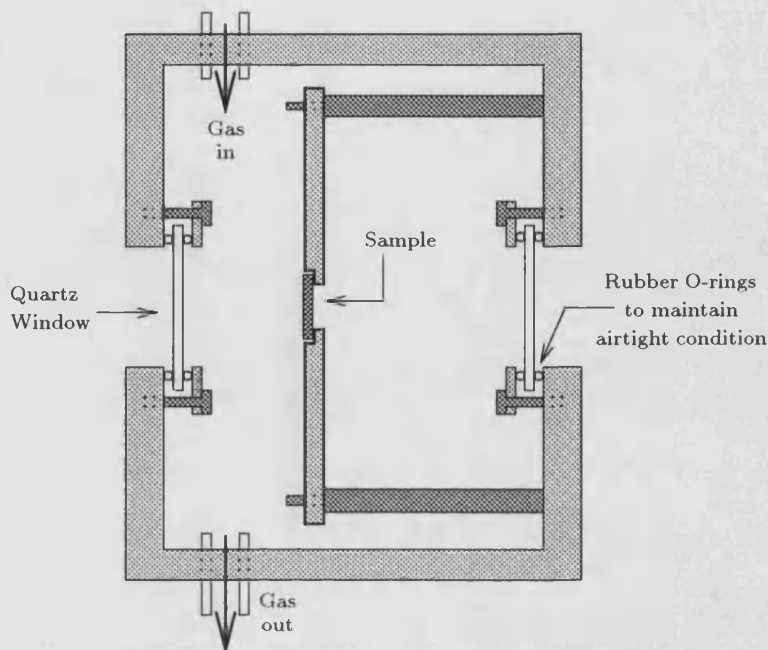
Figure 2.13: Schematic layout of a sample mounted inside the CAC.

stoichiometric uranium dioxide (UO_{2+x}) are being carried out, it is necessary to pass a mixture of carbon monoxide and carbon dioxide gas over the sample to maintain the relevant stoichiometry. The precise mixture depends on the initial stoichiometry and the expected peak temperature to be generated on the sample. Experiments on purely stoichiometric UO_2 are made easier because a mixture of 4% hydrogen in argon or helium is used, which is a standard mixture readily available from BOC™.

Other sample holders can be used depending on the aim of the experiment being undertaken. For example, a "Diamond Anvil Cell" (DAC) would be used in experiments needing high pressures. The configuration of the Mao and Bell [38] DAC is shown in figure 2.14a, with a close up view of the method of sample containment shown in figure 2.14b.
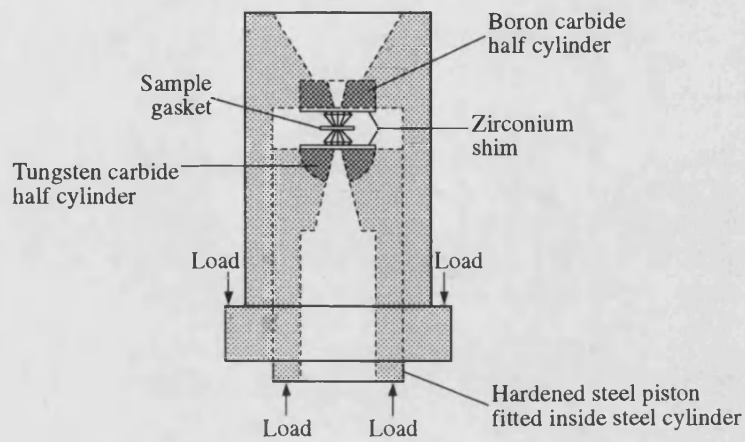
(a) Mao and Bell DAC.
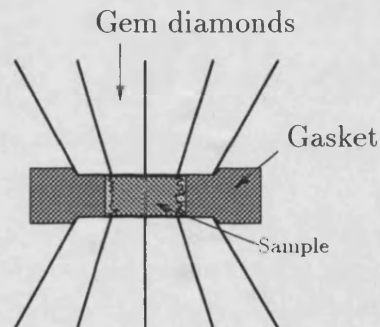
(b) Expanded view of sample containment.

Figure 2.14: Schematic diagram of a "Diamond Anvil Cell" with an expanded view of the sample containment.

The extreme pressures (0.5-1.8 Mbar) generated by DAC devices [27, 39] are achieved by using a lever and fulcrum to force a piston into a cylinder. Only moderate forces are required to be applied to the steel piston, as the small surface area of the diamond facets results in large pressures being generated. With such large stresses being imposed on the gem diamonds, it is important that the facets forming the 'point' of the diamonds are aligned parallel with each other (as depicted in figure 2.14b.), as incorrect alignment results in the diamonds shattering. Measurement of the pressure generated on the sample is achieved by

measuring the change in the fluorescence wavelength of ruby [40, 41], but care needs to be taken to measure the fluorescence at ambient temperature due to large temperature dependence of the ruby R_1-line shift [42]. Crystals of other compounds have been suggested [43, 44] to replace ruby in the measurement of the pressures inside a DAC. The suggested compounds all exhibit a smaller pressure induced fluorescence wavelength shift, but have little or no temperature dependent wavelength shift.

Chapter 3

Mathematical foundations for reconstruction of temperature profiles.

In this chapter, the steps and mathematics needed to reconstruct the radial temperature distribution from the image recorded on the CCD are outlined. The collection optics normally used to focus the image onto the spectrograph are of the cylindrical type discussed in section 2.2, and therefore Abel inversion correction stage will normally be needed to be implemented.

The intensity distribution incident upon the CCD detector array is converted to a 2D array of numbers by the OMA2000 software. In the raw form, these numbers are meaningless; but by applying the linear wavelength calibration previously obtained using a mercury lamp and laser emission lines (described in section 2.3.2), and correcting for the non-linear spectral response of the system, we obtain an array of numbers which represent wavelength against intensity data. This corrected

distribution can then be viewed using a software package called the Utah Raster Toolkit (URT). This program converts the data to a Run Length Encoded (RLE) greyscale picture as shown in figure 3.1. The data in its present form cannot be used to directly determine the temperature distribution, as further analysis is required.
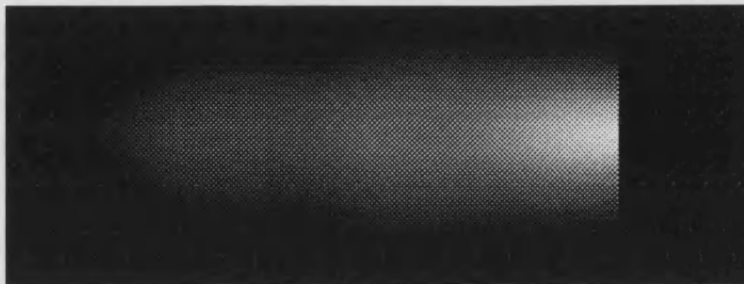
Figure 3.1: RLE picture of an array of sensitivity corrected data.

To obtain a true temperature profile, we need to reconstruct the radial emitted intensity distribution from the array of recorded 'line profiles'. This is achieved by using the Abel inversion, which is described subsequently in section 3.3. We can then fit the spectral distribution to the Planck radiation law, as is described in section 3.4, and obtain the radial temperature profile.

3.1 Wavelength deconvolution of spectrographic data.

The concave holographic grating in the CP200 spectrograph is designed to ensure that all the spatial information is mapped onto the focal plane of the spectrograph with its spatial integrity preserved. So far, no manufacturer has managed to pre-
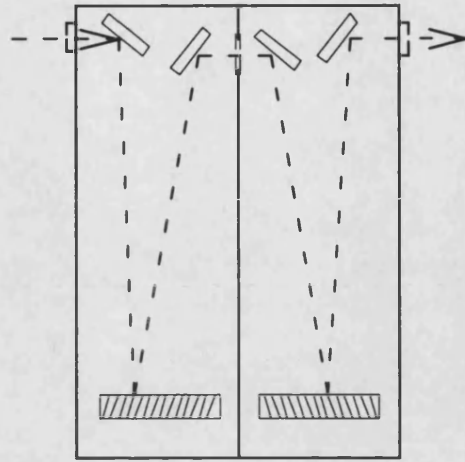
Figure 3.2: Schematic diagram of a twin slit spectrometer.

vent a spectrograph or spectrometer from 'smearing' the wavelength information. This smearing is actually an image of the entrance slit spread over the wavelength domain, and will be subsequently referred to as wavelength convolution.

Precision spectrometers minimise the effect of wavelength convolution by using two gratings, as illustrated in figure 3.2. The first grating has a small dispersion and a small exit slit, which corresponds to a narrow entrance slit for the second grating, which has a larger angular dispersion than the first grating. The increased precision comes from the combination of the angular dispersion of the second grating and the narrow entrance slit, which minimises any wavelength convolution.

The CP200 spectrograph used in our experiment has a 1:1 aspect ratio, which means that if an image of height 1cm is incident on the entrance slit, the image at the focal plane would also be 1cm high. If this image consisted solely of monochromatic light, then the width of the image in the wavelength domain would be the
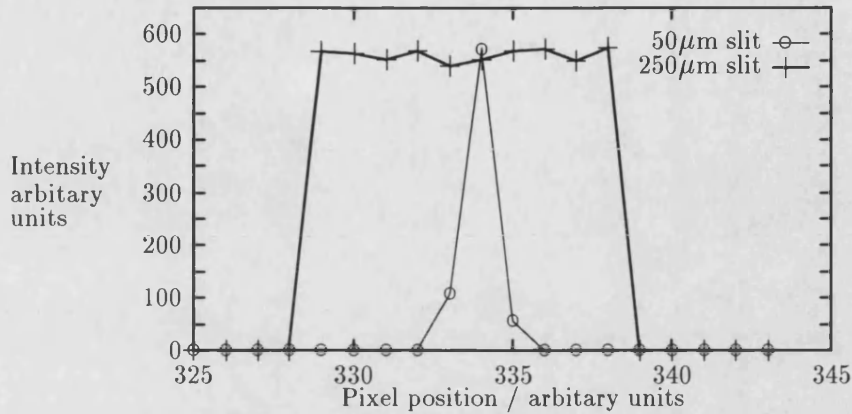
Figure 3.3: Comparison of laser line resolution using 250μm and 50μm slits.

width of the entrance slit. For the CP200, we have three interchangeable entrance slits which can be used (250μm, 100μm and 50μm); of these, the 250μm slit is normally used.

Flooding the entrance slit with light from a helium-neon (HeNe) laser, operating at its red wavelength (632.8 nm), we would expect to measure an image width of 250μm on the CCD. The CCD detector array consists of 'pixels' with an area of 23μm $\times$ 23μm, which corresponds to an image of the slit covering 11 pixels. This can be seen in figure 3.3, along with the same measurement taken using a 50μm slit. If the spread of light over the whole of the slit was uniform, then it would be relatively simple to correct for the convolution [45], but because we are measuring the emitted intensities from a circular hot spot, we face two problems:

1. The light is not monochromatic, but is distributed in the wavelength domain according to the Planck radiation law (equation 3.23).

2. The slit is not evenly illuminated, as we are using a cylindrical focusing
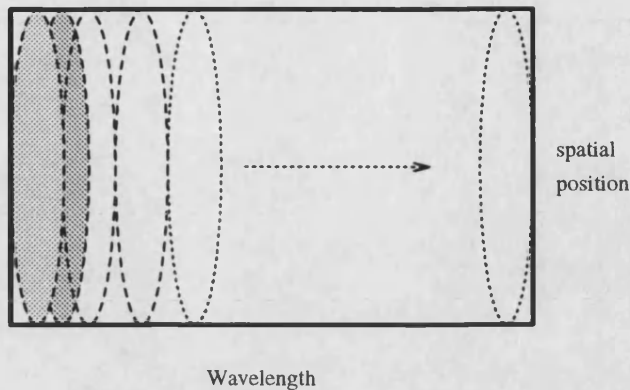
Figure 3.4: Superposition of slit images.

system to compress the data into an elliptical distribution.

This means that our raw data is a superposition of images of the slit, spread over the wavelength domain, similar to that shown in figure 3.4.

Let us suppose that the intensity of the incident light is uniform for all wavelengths, then from figure 3.4, it can be seen that we would have to compensate less at the edges in the spatial direction. If an exponential type distribution along the wavelength domain is included, the raw distribution between two 'cut-off' frequencies would resemble figure 3.5. After we have convoluted this raw data assuming a 250μm slit and an elliptical spatial intensity distribution, the difference between the true data and that recorded on the CCD can be calculated, and is shown in figure 3.6. Note that the largest differences are at either end, adjacent to the two 'cut-off' frequencies.

From the RLE picture shown in figure 3.1, we can see that for a measured data set, the intensity drops off gradually at the blue end of the wavelength range, which means that the effects of wavelength convolution are not significant for our
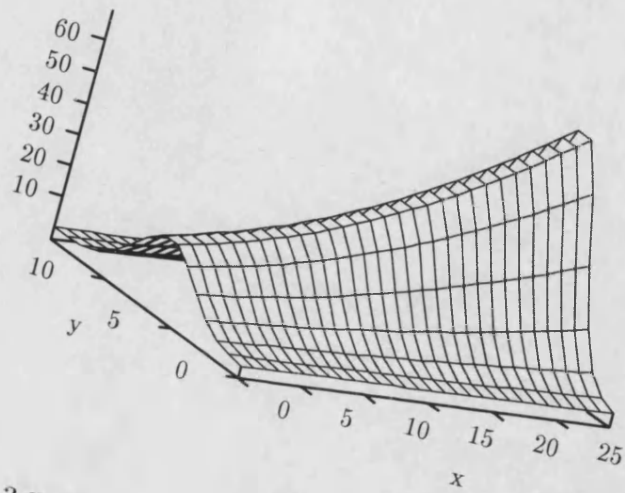
Figure 3.5: Functional form of data before convolution.
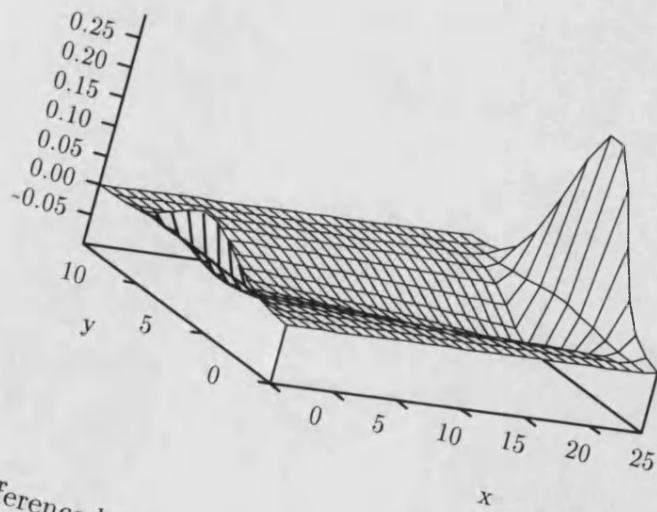
Figure 3.6: Difference between the convoluted data and the functional form.

particular application, as this drop off is mirrored in the long wavelengths before the sensitivity correction occurs.

3.2   The Radon transform.

The ability to obtain 'true data' from a set of line profiles has many applications. One particular example, that most people will be familiar with, is Computed Tomography (CT), which is used primarily in medical scanner technology. In CT, X-rays of a known strength are emitted from a source, and the attenuation μ is measured across a section of the sample. The source and detector are then rotated to a different angle θ, and the process is repeated. With the attenuation known for a complete set of angles $\mu(\theta)$, the distribution of absorbing elements $a(x)$ can be mapped by the method of back projection (equation 3.1), where ϕ and p define the position in the sample in polar coordinates.

$$a(x) \; = \; \frac{-1}{2\pi^2} \int_0^\pi \partial\theta \int_{-\infty}^\infty \frac{\mu(\theta)}{p - r\cos(\phi - \theta)} \partial p. \qquad (3.1)$$

This equation has been shown [46] to be a simplified form of the Radon transform [47], and can be efficiently implemented [48] using Fast Fourier Transforms (FFT's) by computers, so that the measured attenuations can be rapidly converted to a graphical representation of the sample. Consider an example of the forward Radon transform. When a 3D unit square (figure 3.7) is viewed face on ($\theta = 0°$ or 90°), the Radon transform would simply be a square of height 10. If the observer is positioned at an angle of 45 degrees, then the Radon transform resembles figure 3.8. With Computed Tomography, the samples (normally people) are of an arbitrary geometry so it is necessary to take information from a range of
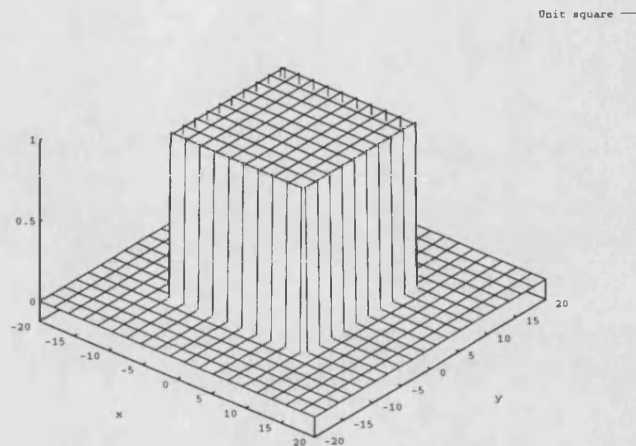
Unit square —

Figure 3.7: A 3D unit square in Cartesian space.

angles. However, if we know that we have a circularly symmetric distribution, then we need only to take data from one viewpoint as the Radon transform is the same for all angles. It is because of this fact that the Abel inversion, used in problems with axially symmetric distributions, is considered a subset of the Radon transform.

3.3   The Abel inversion.

The Abel inversion has been widely used in plasma diagnostics [49, 50, 50–52] to determine the 'true' radial data from the projected 2D linear data obtained experimentally. To try and understand the need for these mathematical algorithms, let us consider a sphere. If we were to take a photograph of a grey sphere, the picture would be of a grey filled circle, which is the surface projection of the sphere. However, in optical experiments the projection will not be of the surface,
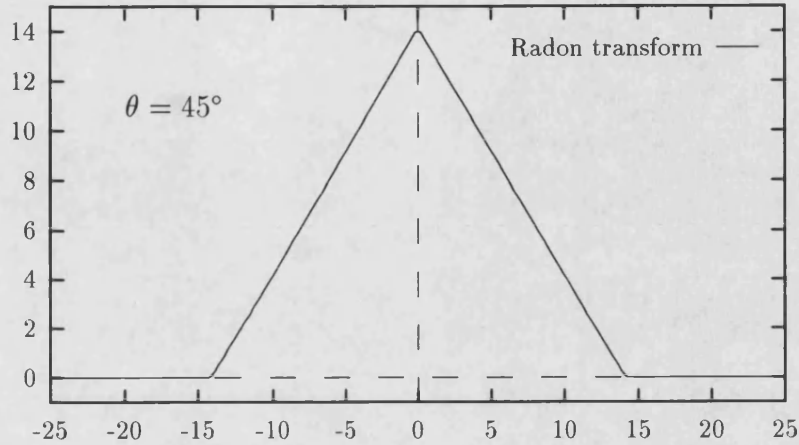
Figure 3.8: The Radon transform of a unit square viewed at 45°.
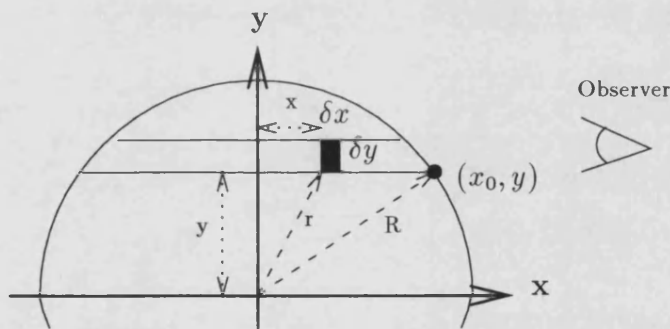
Figure 3.9: Configuration for the forward Abel transform derivation.

but an integrated representation of the 3D object, so the picture would now still be a circle, but the centre of the circle would be more 'grey' than the edges.

Consider a circular disc of thickness δz (shown in figure 3.9), with the radial distribution described by the function $f(r)$. The observed intensity along the x axis for the cross-section $\delta y \delta z$ can then be written:

$$I(y)\,\delta y\,\delta z \;\; = \;\; \sum_{x_0}^{-x_0} f(r)\,\delta x\,\delta z\,\delta y. \tag{3.2}$$

Reducing the small element size $(\delta x \delta y)$ to an infinitesimal size, and introducing the substitution $y = \sqrt{r^2 - x^2}$, we arrive at the expression for the forward transform.

$$I(y) = 2 \int_y^R \frac{f(r)r}{(r^2 - y^2)^{1/2}} \cdot dr \qquad (3.3)$$

$$f(r) = \frac{-1}{\pi} \int_r^R \frac{dI(y)}{dy} \frac{1}{(y^2 - r^2)^{1/2}} \cdot dy. \qquad (3.4)$$

R is the radius of the sample, or the point beyond which the function $f(r)$ can be thought to be zero. The inverse of this transform, shown in equation 3.4, can be obtained by considering a circular symmetric case of the Radon transform. For a full explanation, the reader should consult Deans [46] or Bracewell [53] who detail the mathematical proof.

The relationship between $I(y)$ and $f(r)$ can be visualised graphically (figure 3.10), by considering a "hot-spot" with a radius R which is viewed along one axis. What the eye sees is a 2D image which is in reality constructed out of a set of line integrals. In practice each pixel of the detector has a finite width a, so the collected image is not a set of line integrals, but a set of volume integrals $I(y)$, from which we wish to calculate the radial distribution $f(r)$.

If the expression for $I(y)$ were a known function such as $I(y) = 1 - y^2$ then the distribution $f(r)$ could be directly evaluated using equation 3.4. However we have a discrete data set, not an analytical expression, which means that we have to use numerical approximations. Outlined below is the simplest numerical method for obtaining the radial distribution using the Abel inversion.
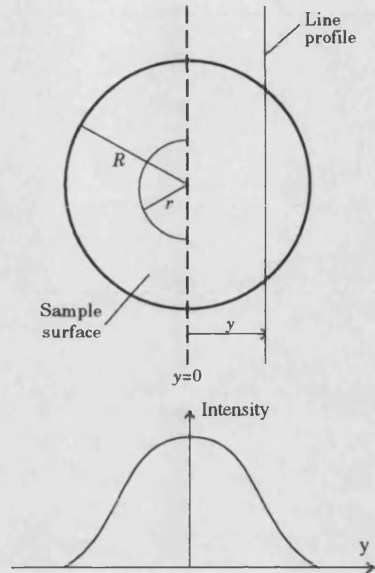
Figure 3.10: Sample surface and its 2D visualisation

3.3.1 The Nestor and Olsen method for Abel inversion.

The Nestor and Olsen method [54] is considered by many to be the simplest to implement, but is only accurate for smooth data sets due to the susceptibility of this method to noise .

The starting point for the Nestor and Olsen algorithm is the Abel inversion equation. This can be converted into a linear form by using a transformation of variables, $u = y^2$ and $v = r^2$. Equation 3.4 can be now written:

$$f(r) = \frac{-1}{\pi} \int_{r^2}^{R^2} (u - v)^{-1/2} \frac{dI(u)}{du} \, du \; . \tag{3.5}$$

The y axis is now be subdivided into N strips, each of width a, with the position of the nth strip being determined by $y_n = na$. Similarly, the radius can be subdivided into k radial sections[1] as shown in figure 3.11. The integral in equation 3.5 only

---

[1] Note that the subscript k corresponds to radial sections, and n the linear.
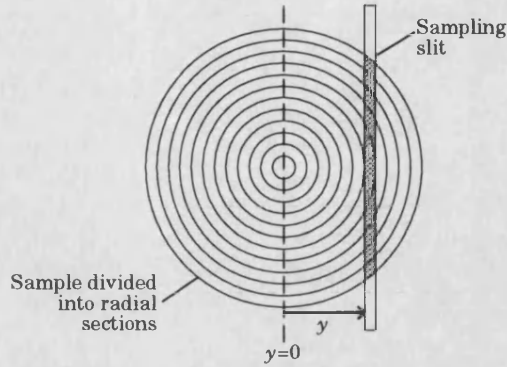
Figure 3.11: Sample surface subdivided into radial sections.

requires the radial components from the desired radius $(r = k)$ to the edge $(r = R)$; therefore the equation can be rewritten as a sum over the strips in the y direction from the strip at $r = k$ to the edge strip:

$$f(v_k) = \frac{-1}{\pi} \sum_{n=k}^{N-1} \frac{dI(u)}{du} \int\limits_{(an)^2}^{(a(n+1))^2} (u - (ak)^2)^{-1/2} \, du \, . \tag{3.6}$$

As the above equation stands, the exact functional form of $I(u)$ needs to be known. To make the inversion algorithm globally applicable, we need to substitute in an approximate expression for the gradient $dI(u)/du$:

$$\frac{dI(u)}{du} \approx \frac{I_{n+1}(u) - I_n(u)}{(a(n+1))^2 - (an)^2}. \tag{3.7}$$

Finally, as $(ak)^2$ in equation 3.6 is constant for a given radius, we can evaluate the integral:

$$\int (u - (ak)^2)^{-1/2} du \equiv 2(u - (ak)^2)^{1/2}. \tag{3.8}$$

Substituting the expressions 3.8 and 3.7 into equation 3.6, we obtain an expression for $f(v_k)$ which is a sum of forward differences. The terms in equation 3.6 are all in terms of the transformation variable u, therefore we can transform back to the y and r ordinates:

$$f(r_k) = \frac{-1}{\pi} \sum_{n=k}^{N-1} A_{kn}(I_{n+1}(y) - I_n(y)) \tag{3.9a}$$

$$A_{kn} = \frac{((n+1)^2 - k^2)^{1/2} - (n^2 - k^2)^{1/2}}{2n+1}. \qquad (3.9b)$$

This summation was expanded and rewritten by Nestor and Olsen [54] in such a way that the difference between subsequent data points is no longer required, but instead the difference in the A_{kn} coefficients is used as a multiplying factor.

$$f(r_k) = \frac{-2}{\pi a} \begin{pmatrix} I_k(-A_{kk}) \\ +I_{k+1}(A_{kk} - A_{kk+1}) \\ + \cdots \\ +I_{N-1}(A_{kN-2} - A_{kN-1}) \\ +I_N A_{kN-1} \end{pmatrix}. \qquad (3.10)$$

This can rearranged to give a more manageable summation:

$$f(r_k) = \frac{-2}{\pi a} \sum_{n=k}^{N} B_{kn} I_n \qquad (3.11)$$

$$\text{where} \quad B_{kn} = -\delta_{kn} A_{kk} + (1 - \delta_{kn})[A_{kn-1} - A_{kn}].$$

3.3.2 Polynomial fitting schemes for Abel inversion.

Various methods of approximating the experimentally obtained 'linear' data $I(y)$ as a polynomial have been tried, with the aim of benefiting from the ease of calculating the differential, and hence evaluating the inversion. These methods can be separated into two parts: simple polynomials, and orthogonal polynomials.

Cubic and Quartic polynomials methods.

Many authors [55–58] have tried fitting their measured linear data to simple polynomials. Some methods are more elaborate than others, but all are based on

the same principle: obtaining an approximation to the linear function $I(y)$ which can then be differentiated using conventional calculus.

The method employed by Barr [59] is different in that numerical analysis techniques were used to 'change' the order of the integration and the differential. If the functions $f(r)$ and $I(y)$ are mathematically well behaved [60], then the Abel inversion can be rewritten as,

$$f(r) = \frac{-1}{2\pi r} \frac{\partial \mathcal{F}(r)}{\partial r} \tag{3.12a}$$

where, $$\mathcal{F}(r) = 2 \int_r^R \frac{I(y)\,y}{(y^2 - r^2)^{1/2}} \cdot \partial y. \tag{3.12b}$$

The function $\mathcal{F}(r)$ is approximated to a numerical data set F_k, which represents the measured data set $I(y)$ multiplied by a coefficient set obtained by a method similar to that used in Nestor and Olsen's method outlined previously in section 3.3.1.

$$F_k = a \sum_{n=k}^{N} \alpha_{kn} I_n \tag{3.13a}$$

$$F(k) = a\,(A_k + B_k k^2 + C_k k^4) \equiv \mathcal{F}(r). \tag{3.13b}$$

The numerical distribution F_k is then fitted to a quadratic polynomial (the right hand side of equation 3.13b), using linear least squares about a five point spread (F_{k-2} to F_{k+2}) to produce an approximating polynomial $F(k)$. When $k \leq 2$, F_k is fitted to $F(k)$ through the points F_0 to F_4. Once the polynomial coefficients have been obtained for each radial position k, the radial distribution can be calculated using combinations of the B_k and C_k polynomial terms, as the A_k term disappears in the differentiation.

Orthogonal polynomial methods.

The advantage of using orthogonal polynomials, in particular Chebyshev polynomials, lies in their accuracy in replicating a function using a relatively small number of coefficients. Their use also facilitates rapid calculation without introducing serious truncation errors.

The mathematical definition of an orthogonal function is

$$\int_a^b Q_m(y)\, Q_n(y)\, dy = \left\{ \begin{array}{ll} 0 & \forall m \neq n \\ h_n^2 & \forall m = n \end{array} \right. . \tag{3.14}$$

The h_n^2 term is called the *norm* of the function, and will be real and positive if the function $Q(y)$ is real. If a weighting function is introduced, then the limits can be extended to $\pm\infty$, as long as the weights are zero outside the region (a, b).

The name *orthogonal* comes from an analogy with vector algebra. Two vectors **a** and **b** are said to be orthogonal if their scalar product vanishes (equation 3.15a). For three dimensional space $(l = 3)$, the scalar product will vanish if **a** and **b** are mutually perpendicular vectors.

$$\mathbf{a} \cdot \mathbf{b} = \sum_{k=1}^{3} a_k\, b_k = 0 \tag{3.15a}$$

$$\Rightarrow \mathbf{Q}_m \cdot \mathbf{Q}_n = \sum_{k=1}^{l} Q_{mk}(y)\, Q_{nk}(y) = \left\{ \begin{array}{ll} 0 & \forall m \neq n \\ h_n^2 & \forall m = n \end{array} \right. . \tag{3.15b}$$

The Chebyshev polynomial of degree n is generated by equation 3.16a, and satisfies the orthogonality condition 3.16b where $w(y)$ is the weighting function shown in equation 3.16c.

$$T_n(y) = \cos(n \arccos y) \tag{3.16a}$$
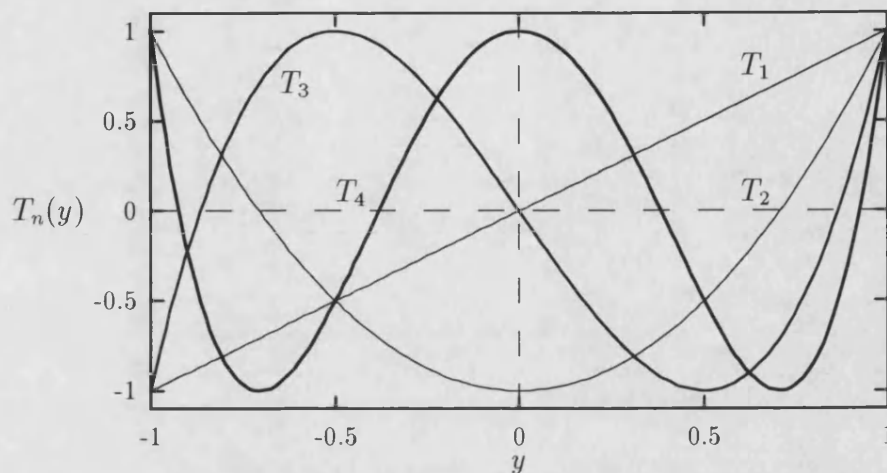
Figure 3.12: Chebyshev polynomials of degrees $n = 1$ to 5.

$$\int\limits_{-1}^{1} w(y)\, T_i(y)\, T_j(y)\, dy \;=\; \begin{cases} 0 & i \neq j \\ \pi/2 & i = j \neq 0 \\ \pi & i = j = 0 \end{cases} \qquad (3.16b)$$

$$w(y) \;=\; \frac{1}{\sqrt{1 - y^2}}. \qquad (3.16c)$$

The first five Chebyshev polynomials are shown in figure 3.12. If we have a large data set of N points, then the data can be exactly reproduced by the sum of N Chebyshev polynomials. However, calculation of this many polynomials would be time consuming, but truncation of the series to a lower degree m would introduce an error no larger than the first neglected term. As the maximum admitted value of the Chebyshev polynomials is unity, the size of the truncation error will be no larger than the first omitted approximating coefficient a_{m+1}. The rapidly decreasing magnitudes of the a_k coefficients generated by a conventional fitting routine means that the truncation error will be small.

$$f(y) \approx \left[\sum_{k=1}^{m} a_k T_{k-1}(y) \right] - \frac{1}{2} a_1. \qquad (3.17)$$

To fit to the 'linear' data $I(y)$ using Chebyshev polynomials, we need to change

the experimental range of $R \geq y \geq 0$ to match the Chebyshev orthogonality interval [-1:1]. Using a conventional curve fitting method [61], $I(y)$ can be approximated by the polynomial $P_m(y)$.

$$I(y) \equiv P_m(y) = (y^2 - R^2) \left(\left[\sum_{k=1}^{m} a_k T_{k-1}(2\frac{y^2}{R^2} - 1) \right] - \frac{1}{2}a_1 \right). \quad (3.18)$$

Next we make a change of variable,

$$y^2 = \frac{1}{2}(R^2 - r^2)u + \frac{1}{2}(R^2 + r^2) \quad (3.19)$$

which enables the Abel inversion equation to be rewritten as [62]:

$$f(r) = -\frac{1}{\pi}\sqrt{\frac{1}{2}(R^2 - r^2)} \int_{-1}^{1} \frac{\phi(u)}{\sqrt{u+1}} \partial u \quad (3.20a)$$

where

$$\phi(u) = \zeta \left(\frac{R^2 - r^2}{R^2}u + \frac{r^2}{R^2} \right)$$
$$+ \frac{R^2 - r^2}{R^2}(u - 1)\frac{\partial \zeta}{\partial x} \left(\frac{R^2 - r^2}{R^2}u + \frac{r^2}{R^2} \right) \quad (3.20b)$$

and

$$\zeta(z) = \left[\sum_{k=1}^{m} a_k T_{k-1}(z) \right] - \frac{1}{2}a_1. \quad (3.20c)$$

3.4 Fitting to the Planck radiation law.

3.4.1 Linear least square methods - the Wien approximation.

The simplest case for linear least squares regression is the fitting of a straight line to a data set in order to obtain the gradient and intercept. In mathematical terms; if we have a data set of N data points, represented by $d(x)$ then m and

c in equation 3.21 are varied such that the sum of all the residuals, squared is minimised.

$$f(x) \quad = \quad mx \ + \ c \tag{3.21}$$

$$\Rightarrow \quad Min \quad \left\{ \sum_{x=1}^{N} [f(x) - d(x)]^2 \right\}. \tag{3.22}$$

For our particular application, we are trying to fit an array of wavelength (λ) versus intensity to the Planck radiation law shown in equation 3.23.

$$I_p(\lambda, \varepsilon, T) \quad = \quad \frac{2\pi hc^2 \varepsilon}{\lambda^5} \frac{1}{\exp(hc/\lambda kT) - 1}. \tag{3.23}$$

This equation represents the wavelength distribution emitted from a body at a temperature T with an emissivity ε. The minus one in the denominator of equation 3.23 means that it is not possible to describe the wavelength distribution in a linear form of the type shown in equation 3.21.

If we look back into history, circa.1900, there were many eminent physicists trying to explain the radiation spectrum emitted from a thermal cavity. Rayleigh and Jeans postulated that the radiation was due to standing waves inside the cavity, resulting in an expression which fitted the available data well at long wavelengths, but seriously disagreed at shorter wavelengths. This became known as the ultraviolet catastrophe. Max Planck was subsequently awarded the Nobel physics prize in 1919 for his work in applying quantum theory to this problem, and the derivation of equation 3.23.

In 1911, Wilhelm Wien was awarded the Nobel prize for demonstrating that the product of the wavelength at maximum intensity and the temperature was
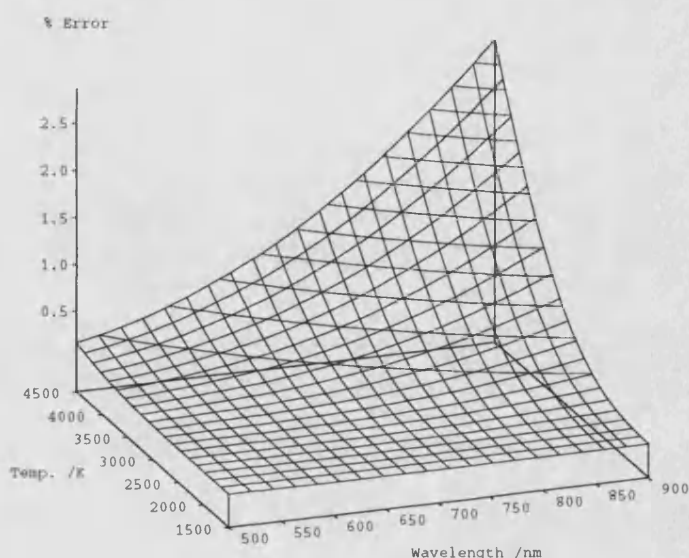
Figure 3.13: Error between Planck distribution and the Wien approximation.

a constant. This in turn led to an expression for the intensity, which can be linearised (equation 3.24b), called the Wien approximation:

$$I_w(\lambda, \varepsilon, T) = \frac{2\pi hc^2 \varepsilon}{\lambda^5} \frac{1}{\exp(hc/\lambda kT)} \qquad (3.24a)$$

$$\Rightarrow \ln\left(\frac{I_w \lambda^5}{2\pi hc^2}\right) = -\frac{1}{T} \cdot \frac{hc}{\lambda k} + \ln \varepsilon. \qquad (3.24b)$$

Although not as precise as Planck's expression, the errors in the visible part of the spectrum only reach the order of 2% at the long wavelength and high temperature limits, as demonstrated by figure 3.13.

Using the linearised Wien approximation (equation 3.24b), we can fit our data using a conventional linear least squares analysis. The disadvantage of this method is that any point with an associated large error can 'pull down' the regression line, as the analysis does not weight the points according to their errors. This

is demonstrated in figure 3.14, along with an improved method which will be described in the following section.

3.4.2 Iterative reweighting fitting to the Planck curve.

In our application, data from the edge of the sample has much smaller intensities than the central tracks. The effect of this reduced intensity can manifest itself as a ripple after we have corrected for the sensitivity, and thus cause the fitted line to be too steep as shown in figure 3.14.
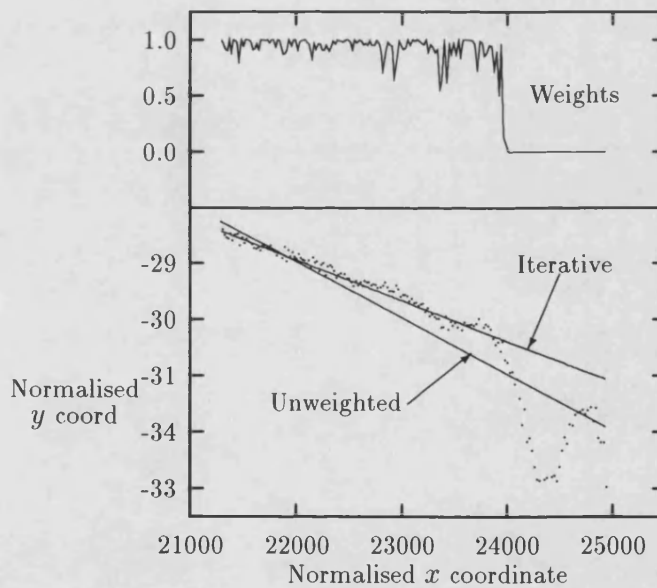
Figure 3.14: Fits with conventional least squares and iterative reweighting analysis.

Once an initial linear least squares analysis has been performed on the data set, we recalculate the weights of each point so that they are proportional to the

distance of the data point to the fitted line, and then the weights are normalised

relative to the standard deviation of residuals (σ):

$$w(x) = w\{d(x) - f(x)\} \qquad (3.25a)$$

$$\sigma = \frac{1}{0.6745} \cdot \text{median}\left(|d(x) - f(x)|\right). \qquad (3.25b)$$

The new weighting function (w_{new}) is then calculated from the normalised weights

(u), and includes a 'cut-off' constant (c).

$$w_{new} = \begin{cases} \left[1 - (\frac{u}{c})^2\right]^2 & |u| \leq c \\ 0 & |u| > c \end{cases} . \qquad (3.26)$$

This process is repeated until the new weights are identical to those obtained

from the previous step. The weights finally obtained by this method are also

shown in figure 3.14.

3.4.3   Non-linear least square fitting methods.

The method of iteratively reweighting a linear least squares analysis is applicable

only to those functions which are linearly reducible. However, some functions

are non-linear, and to fit a set of data to these functions we need to employ

non-linear least square fitting methods. Let us consider a general function with

α parameters $(m^1, m^2 \cdots m^\alpha)$, which we shall write as $g(m)$. In trying to fit the

observed data (d^i_{obs}) to the function $g(m)$, the difference between the observed

data and the function is monitored, so that when the parameters are correct, the

difference will be ideally zero.

If our initial guesses for the parameters (m_{prior}) are not exactly correct, then we
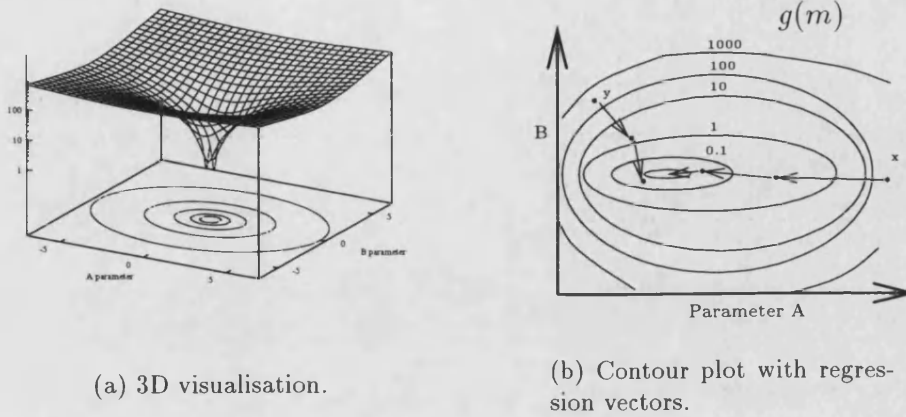
(a) 3D visualisation.

(b) Contour plot with regression vectors.

Figure 3.15: Visualisation of steepest descent non-linear regression.

can calculate a *misfit* function $S(m)$:

$$S(m) = \frac{1}{2}\left[\sum_i \frac{(g^i(m) - d^i_{obs})^2}{(\sigma^i_d)^2} - \sum_\alpha \frac{(m^\alpha - m^\alpha_{prior})^2}{(\sigma^\alpha_m)^2}\right]. \qquad (3.27)$$

For any given $g^i(m)$, the fitting routine converges to a minimum using the method of steepest descent. If the initial estimates of the A and B parameters are m^A_{prior} and m^B_{prior} respectively, then the starting point for the regression will be at the point with coordinates $(m^A_{prior}, m^B_{prior})$, marked as **x** in figure 3.15b. By calculating the residuals in a small radius surrounding the starting point, the direction of the steepest descent can be determined. After the regression routine has moved along this direction by a length determined by the local gradient, the process is repeated until the minimum is reached. A similar case is also shown in figure 3.15b with a starting position labelled as **y**, which may appear to be nearer to the minimum than **x**, but will still require the same number of iterations to converge. One way of visualising the regression routines workings is to imagine a marble placed at the starting point. From figure 3.15a, we would see the marble roll downwards, and come to rest at the minimum.

If $g^i(m)$ is differentiable with respect to all points and parameters, then a derivative of the misfit function can be obtained. At the desired minimum, the gradient of the misfit function will be zero:

$$\left[\frac{\partial S}{\partial m}\right]_{m_n} = 0. \tag{3.28}$$

The existence of local minima, and/or saddle points, means that the converse of the above is not always true. To check for convergence to the global minimum, different starting points (m_{prior}^{α}) are needed, and confirmation that the routine converges to the same minimum, with the derivative of the misfit function being zero.

When the gradients can be easily calculated, a more efficient scheme of regression can be employed. In the Gauss-Newton method of regression, subsequent parameters from the starting point are calculated by the algorithm:

$$m_{n+1} = m_n - \left[\frac{\partial^2 S}{\partial m^2}\right]_{m_n}^{-1} \left[\frac{\partial S}{\partial m}\right]_{m_n}. \tag{3.29}$$

3.5   Techniques for smoothing data sets.

In the many steps needed to convert experimental data to a temperature profile, the presence of noise can lead to major errors at two stages of the analysis:

1. the conversion of the data from a linear form to a radial form (Abel inversion, section 3.3),

2. the fitting of the irradiance distribution to the Planck radiation law (section 3.4).

Localised irregularities can be seen in figure 3.16a where the dark spots are ice

crystals and the bright spots are water droplets. In this case we can distinguish

(a) Data showing local 'drop-
outs'.

(b) After smoothing.
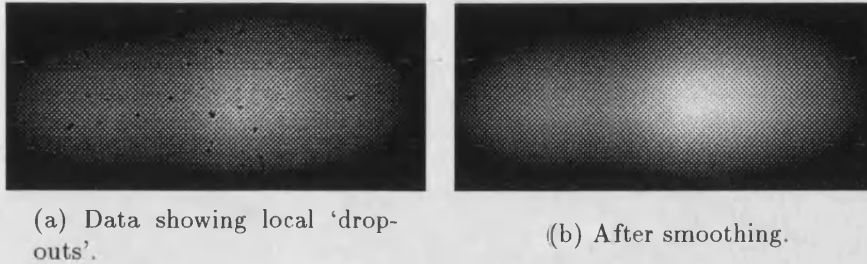
Figure 3.16: Demonstration of smoothing to remove localised irregularities.

between the ice crystals and the water droplets because the water droplets act

as a miniature lens focusing the light to a small bright spot with a darker ring

around it, whilst the ice crystals reflect light away from the CCD. The effect of

the irregularities can removed by smoothing using either moving averages (sec-

tion 3.5.1) or Fourier techniques (section 3.5.2) to produce a smoothed output

similar to that shown in figure 3.16b. In the case of the Abel inversion, the data

also needs to be symmetric; symmetrisation can be achieved by simply averaging

the data from each side of the centre point, or by a more elegant method outlined

in section 3.5.3.

3.5.1   Spline approximations and moving average smooth-ing methods.

If we were trying to obtain the value of a single constant from a large number of

similar readings, we would naturally sum all the readings and then divide by their

total number, ie average the data. For a data set with an unknown functional

form, averaging is obviously unsuitable, but the variation known as nine point

smoothing can be used. If we take any point n, we can smooth the data by averaging over a nine point spread centred around the point n, but a weighting function is introduced to reduce the emphasis of points further away from n.

$$
\begin{aligned}
5f(n) \quad = \quad & f(n) + \frac{4}{5}f(n-1) + \frac{3}{5}f(n-2) + \frac{2}{5}f(n-3) + \frac{1}{5}f(n-4) \\
+ \quad & \frac{4}{5}f(n+1) + \frac{3}{5}f(n+2) + \frac{2}{5}f(n+3) + \frac{1}{5}f(n+4).
\end{aligned} \tag{3.30}
$$

Alternatively, with the advent of computer efficient algorithms, it is fairly easy to fit a smooth curve through a data set using splines. We can determine the amount of smoothing used by limiting the maximum number of B-spline coefficients used to reconstruct the data.

3.5.2 Fourier techniques for data smoothing - convolution with specialised lag windows

By far the most powerful tool used for image processing is the use of Fast Fourier Transforms (FFT's), which are most computationally efficient for data sets of size 2^n, where n is an integer. If we consider a noisy data set, the noise will be replicated in the higher frequency components of the FFT relating to the harmonics of the sampling frequency.

The most obvious method to remove the noise would be to pass the Fourier coefficients through a high-pass filter where only the FFT coefficients corresponding to frequencies under a 'cut-off' value of M are passed onto the reconstruction routine. The computer implementation of the high-pass filter is more commonly known as the Heaviside lag window.
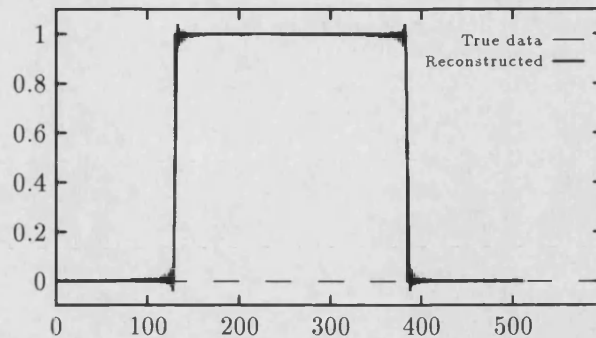
Figure 3.17: Reconstructed square pulse showing effects of series truncation caused by convolution with a Heaviside lag window.

Consider the construction of a square wave $\prod(x)$ from the sum of sin waves:

$$\prod(x) = \sum_{n=1}^{\infty} a(n) \sin\left((2n-1)x\right) \tag{3.31}$$

If we truncate this series so that the upper limit is lowered to a finite value, ripples will be introduced into the reconstructed square wave, which can be seen in figure 3.17. To avoid this problem, we can use two specialised lag windows, namely the Parzen and Tukey-Hanning windows which have the functional forms shown below:

$$
\begin{aligned}
\text{Parzen} \qquad \lambda(k) \;=\;& 1 - 6\left(\tfrac{k}{M}\right)^2 + 6\left(\tfrac{k}{M}\right)^3 \quad && k \in [0, M/2] \\
& 2\left(1 - \tfrac{k}{M}\right)^3 \quad && k \in [M/2, M]
\end{aligned} \tag{3.32}
$$

$$\text{Tukey-Hanning} \quad \lambda(k) \;=\; \tfrac{1}{2}\left(1 + \cos(\tfrac{\pi k}{M})\right) \qquad k \in [0, M].$$

The three lag windows described above are depicted in figure 3.18, with the 'cut-off' frequency M set to 100 for all cases.
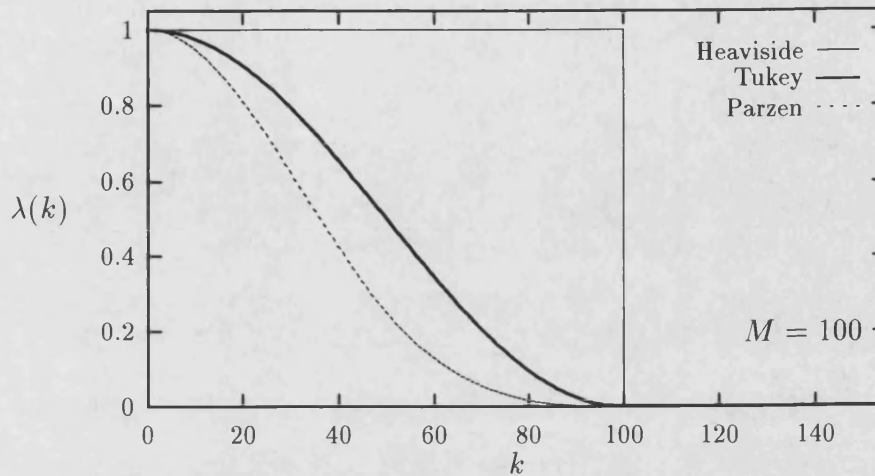
Figure 3.18: Graphical representation of three lag windows.

3.5.3   Fourier symmetrisation.

The Abel inversion (section 3.3) is only valid for data which is axially symmetric. To ensure that this condition is met, the measured 'linear' data obtained is symmetrised before being inverted. A method to symmetrise real data sets using FFT's is outlined below.

Any function $f(x)$ can be written as a sum of an even and an odd function:

$$f(x) = e(x) + o(x). \tag{3.33}$$

The definitions of an even function $e(x)$ and and odd function $o(x)$ are,

$$e(x) \;\; = \;\; e(-x) \tag{3.34a}$$

$$\text{and} \qquad o(-x) \;\; = \;\; -o(x). \tag{3.34b}$$

Using these definitions, equation 3.33 can also be written:

$$f(-x) = e(x) - o(x). \tag{3.35}$$

Equating the even terms in equations 3.33 and 3.35, and relating to a discrete data set $I(x)$ with its centre point at $x=c$, the method known as two-sided averaging can be derived:

$$I_{sym}(x + c) = \frac{1}{2}\left(I(c - x) + I(c + x)\right). \tag{3.36}$$

A more elegant method is to take the Fourier transform of equation 3.33:

$$F(s) = 2\int_0^\infty e(x)\cos(xs)dx \ - \ 2i\int_0^\infty o(x)\sin(xs)dx, \tag{3.37}$$

where s is the spatial frequency. It can be seen from equation 3.37 that the even part of the function is represented by the real part of the Fourier spectrum, and conversely, the odd part manifests itself in the imaginary part of the Fourier spectrum. Therefore to obtain just the symmetric form of function $f(x)$, we take the Fourier transform of the data, and reconstruct using only the real components of the Fourier spectrum.

$$f_{sym}(x) = \text{FFT}\left[\Re\left(F(s)\right)\right]. \tag{3.38}$$

The effectiveness of this simple method is shown in figure 3.19 where Fourier symmetrising and smoothing by convolution with a Tukey lag window is used on a noisy data set to produce a clean Gaussian signal.
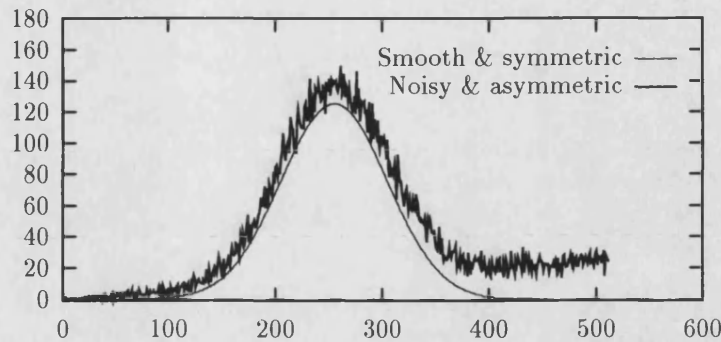
Figure 3.19: The effect of Fourier smoothing and symmetrisation.

3.6 Computer implementation for calculation of temperature profiles.

To implement the methods of analysis outlined in the preceding sections, a computer analysis program (OMA2T) was written in FORTRAN with each mathematical stage previously discussed written as a subroutine. The division of the main program makes it easier to change the ordering of the analysis. Changing the order of the spectral sensitivity correction and the Abel inversion does not violate the legitimacy of the analysis, because the Abel inversion only affects the spatial distribution, whilst the spectral sensitivity correction operates in the wavelength domain. A flow chart of the steps needed to correct from the raw data obtained from the CCD to the temperature profile is shown in figure 3.20.
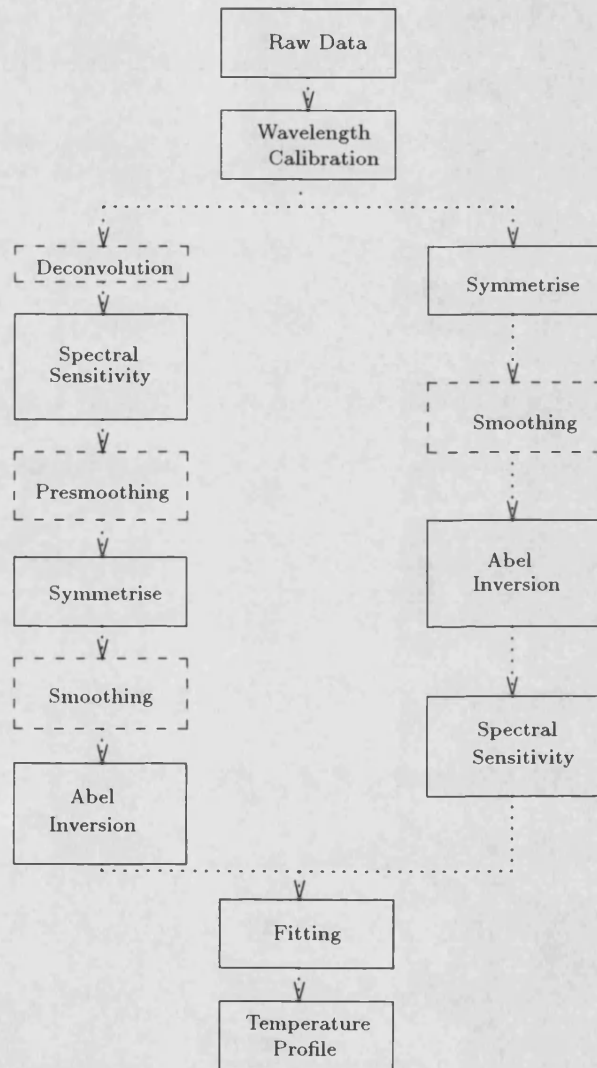
Figure 3.20: Flowchart of the OMA2T program.

Chapter 4

Results validating the accuracy of the laser heating apparatus.

After the laser heating apparatus had been constructed, the next step was to calibrate the system. This calibration process produced results which have been used to validate the accuracy of the measured temperature distributions. Firstly, the power distribution delivered by the laser needs to be characterised (section 4.1) so that the thermal parameters of the material being heated can be determined. To test that the computer routines calculating the temperature are producing accurate results, the temperature distribution of a known source (section 4.2) was measured and compared to the calibrated distribution. As a secondary check of the accuracy of the temperature measuring system, melting point measurements were made by analysis of the temperature profiles generated on 'standard' materials (section 4.4). Finally, having calibrated and tested the system, temperature profiles produced by the Nd:YAG laser on stoichiometric uranium dioxide (UO_2) were measured.

4.1   Characterisation of the laser beam.

Before any meaningful thermal data can be obtained, the exact distribution and quantity of heat being supplied to the sample by the laser needs to be known. To accomplish this task, an *Optilas Beamscan*™ beam profiler was used to measure directly the laser beam's characteristics at the focus. The beam profile data is built up by scanning a slit across the laser beam, and recording the image on a silicon photodiode. This enables powerful laser beams to be measured without destroying or swamping the silicon detector.
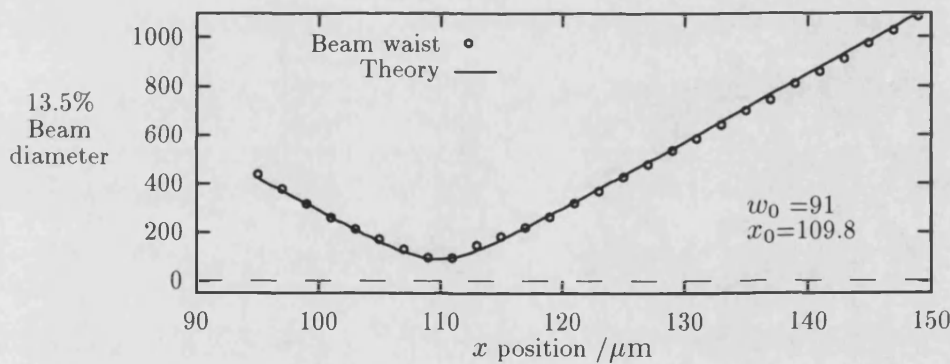
Figure 4.1: Beam width through the focus, as a function of distance from the focusing lens.

When the laser is operating in the monomode configuration, the spatial distribution at the focus of the beam can be modeled with Gaussian optics. A comparison between theory and the data obtained for the Gaussian $1/e^2$ beam width through the focus is shown in figure 4.1. A similar comparison for the measured peak irradiance as a function of position through the focus is shown in figure 4.2. When the theoretical values for the minimum beam waist (ω_0) and focus point (x_0)
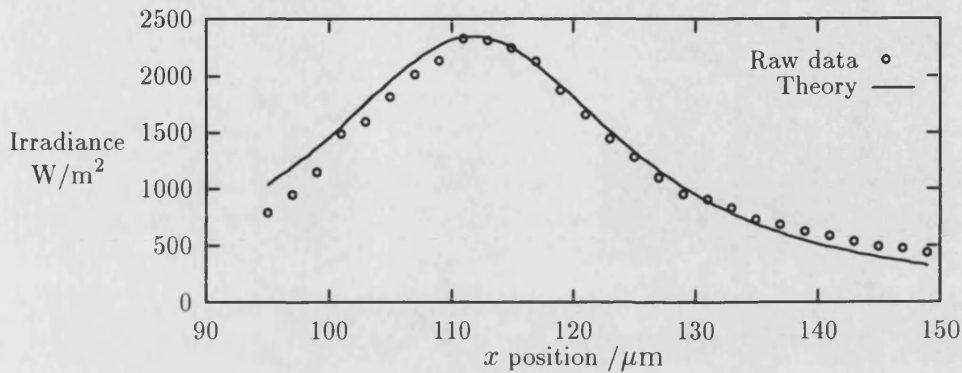
Figure 4.2: Peak irradiance Gaussian beam characteristics.

have been extracted from the measured data, the expected irradiance distribution through the focus can be drawn (figure 4.3). Finally, the monomode peak
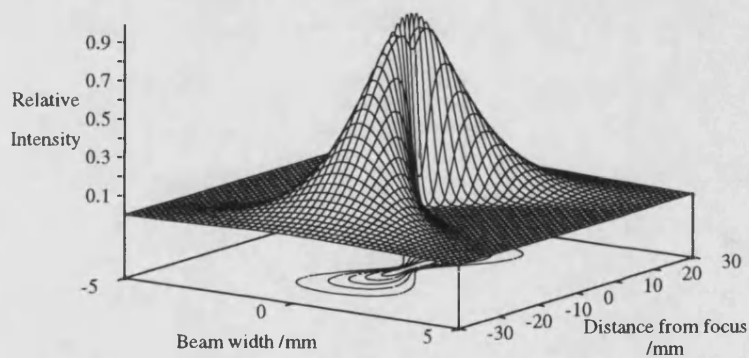
Figure 4.3: Irradiance profile of laser beam through focal point.

irradiance incident on the sample can be predetermined by setting the current supplied to the laser to the value calculated from figure 4.4.

The combination of two mirrors and a multi-element lens in the laser's optical
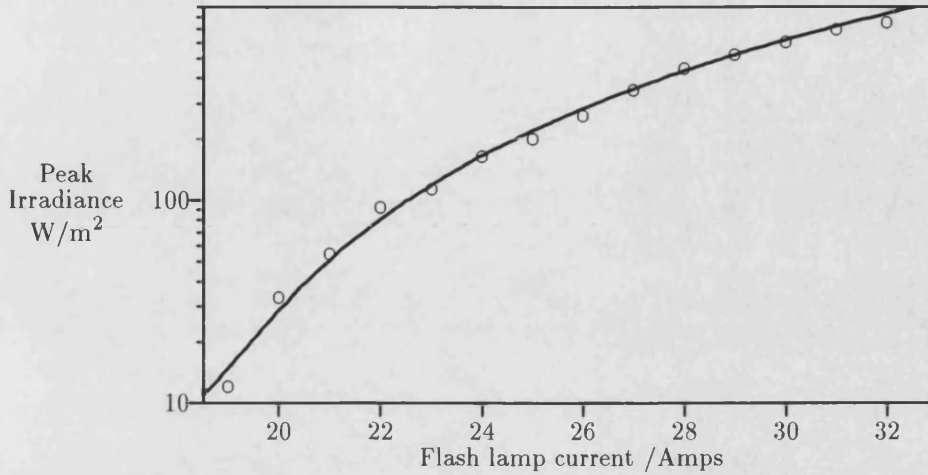
Figure 4.4: Peak irradiance dependence on power supply current.

path means that aberrations in the beam might manifest themselves if the system were not properly aligned. One such aberration is a 'coma' caused by the focusing lens not being properly aligned, as illustrated in figure 4.5a. Profiles of the laser beam taken during the initial alignment of the optics show a 'textbook' example of such an aberration, with the coma being labeled in figure 4.5b.

A less serious aberration can occur from misalignment of the dichroic and gold mirror combination causing the beam to be propagated along a direction other than the optic axis. This can be seen from the set of results taken using the *Beamscan* shown in figure 4.6, which shows how the position of the peak changes through the focus. This divergence corresponds to a deviation from the optic axis of only 0.2 seconds of arc, illustrating the sensitivity of the *Beamscan* and its usefulness in constructing and testing optical assemblies.
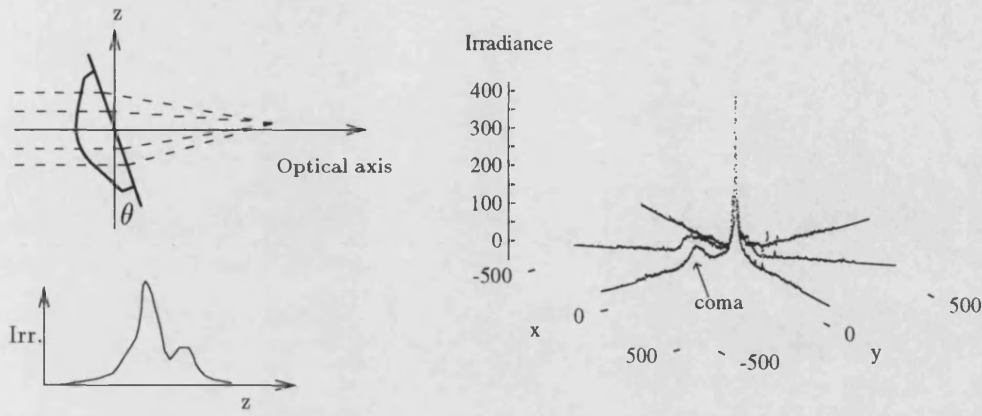
(a)   The   effect   of
skew mounting the focusing
lens.

(b) Profile of monomode laser beam.

Figure 4.5: Development of a 'coma' produced by misaligned optics.

4.2 White light calibration experiments.

To determine the wavelength dependent absorption of the system, the spectral distribution of a tungsten lamp, previously calibrated at NPL, was measured using the same optical system used to produce and measure the 'hot-spots'. The measured spectral distribution can then be compared to the calibrated distribution
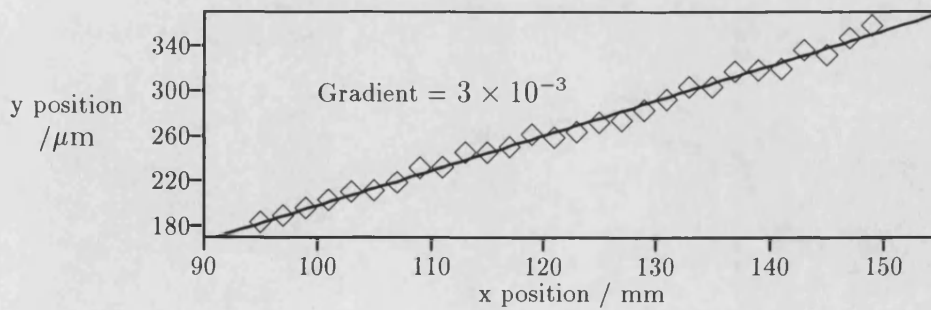
Figure 4.6: Beam divergence from the optic axis caused by mirror misalignment.

of the lamp, and the absorption of the system obtained, as has been described earlier in section 2.3.3.

The tungsten lamp emits a spectral distribution of light identical to that which would be emitted from a 'black-body' radiator, with a colour temperature [36] of 2977 K. Therefore, the accuracy of our analysis can be tested by measuring the spectrum emitted from a pinhole placed at the focus of the multi-element objective lens, with the tungsten lamp illuminating the rear. The temperature profile measured for a back illuminated 100μm pinhole is shown in figure 4.7.
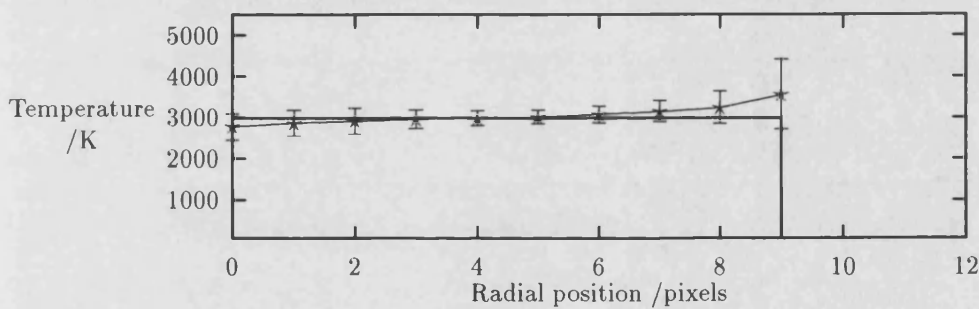
Figure 4.7: Temperature profile of 100μm pinhole.

In figure 4.7, the slight upward trend in temperature from the centre can be explained by the pinhole not being placed exactly at the focus of the laser focusing lens. The displacement caused the blue part of the emitted spectrum to be more sharply focused in the centre, and the red light to be biased at the edges. These biases will respectively lower and raise the temperature when measured by fitting to the Planck radiation law. To avoid these complications, a steel shim was mounted in the sample holder (CAC), and the laser was used to 'drill'
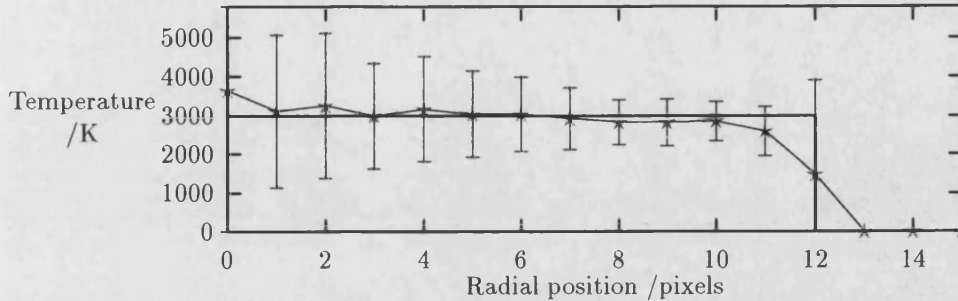
Figure 4.8: Temperature profile of laser drilled steel shim.

a hole through the shim. The pinhole thus formed is known to be at the laser focus, but the diameter of the hole is not immediately known, and needs to be subsequently measured by a travelling microscope. The temperature profile for a back illuminated laser drilled shim, with a measured width of 12 pixels, is shown in figure 4.8. The size of the image for the 100μm pinhole produced on the CCD detector is 207μm, therefore the magnification factor for the focusing optics is 4.37, which compares to 4.286 calculated from geometric optics. Using this magnification factor, the measured width of 12 pixels corresponds to a hole diameter of 131μm; the width subsequently measured by a travelling microscope was the same, within experimental error.

Ideally, measuring the temperature distribution of the white light shone through an annulus would present no problems, but from figure 4.9, it can be seen that although the analysis produces the correct widths of the annulus rings, the measured temperatures are inaccurate. These inaccuracies result primarily from the Abel inversion stage of the mathematical analysis, which has to resolve discontinuities in the gradient of the 'linear' data set produced by the forward transform
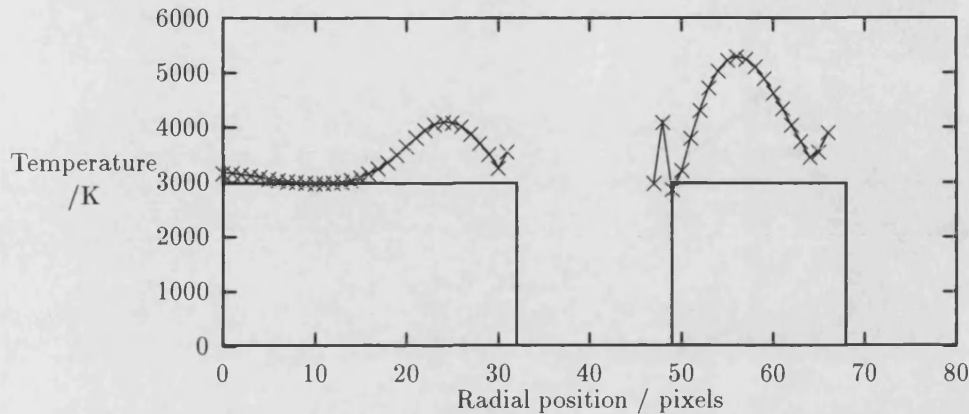
Figure 4.9: Temperature profile of an annulus (error bars omitted for clarity).

of an annulus distribution. Any numerical inversion scheme will always have difficulty reproducing these types of distributions, whereas monotonically decreasing distributions, such as Gaussian distributions, present no such problems.

4.3   Multimode heating.

The characteristics of the beam emitted from a laser are determined by the design of the laser cavity. A good example is a helium neon gas laser. The energy level diagram for the helium-neon mixture suggests that there will be four wavelengths at which the device will naturally lase; green (543nm), yellow (594nm), orange (612nm) and red (633nm). To select the red line alone, the optical length of the cavity is constructed so that a resonance condition occurs for $\lambda = 633$nm. Similarly, by placing a small aperture in front of the mirrors of the Nd:YAG laser, we can restrict the laser to operate in the fundamental TEM_{00} mode, or monomode as it is commonly known. Restricting the amount of radiation lasing

will naturally reduce the power of the emitted beam, therefore the maximum power available in the monomode is only 17 Watts compared to the 32 Watts available in the multimode configuration.

4.3.1 Heating of vitreous carbon as a test material.

With the laser operating in the multimode configuration and the current supplied to the flashlamps set to a minimum, a sample of vitreous carbon was heated. Initially a very bright spot was observed, which subsequently subsided to a red/orange coloured spot. The initial bright spot was attributed to the burning of the glassy surface characteristic of the manufacturing process, and was at such intensity that it was impossible to measure without saturating the CCD detector system.
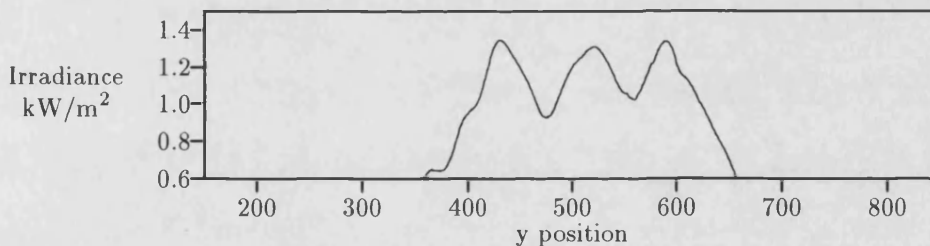
Figure 4.10: Multimode beam profile as measured at the beam focus.

A profile of the multimode laser beam is shown in figure 4.10, and the corresponding temperature profile produced on the vitreous carbon sample is shown in figure 4.11. It is believed that the dip in the centre of the profile was caused by the excessive power of the laser vaporising portions of the sample, producing a hollow. The bottom of the hollow produced would be further from the focus of
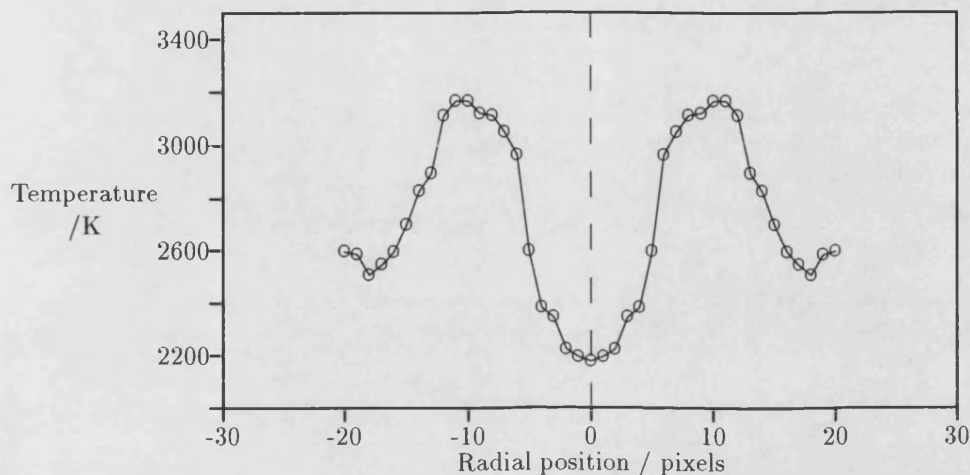
Figure 4.11: Temperature profile produced on vitreous carbon.

the laser beam, and therefore would be subjected to lower power densities, and hence would not reach such high temperatures as its surrounding areas.

4.4 Monomode heating (TEM$_{00}$).

The large power densities obtainable in the multimode configuration have caused some samples to disintegrate. This fact, allied with inaccuracies in the analysis caused by the presence of three peaks in the power distribution (demonstrated in figure 4.10), means that the use of the monomode configuration is recommended, and all further measurements discussed in this thesis used this configuration. A beam profile measured with the laser operating in the TEM$_{00}$ mode is shown in figure 4.12 with the characteristic Gaussian parameters (I_{max},w_0) also shown.
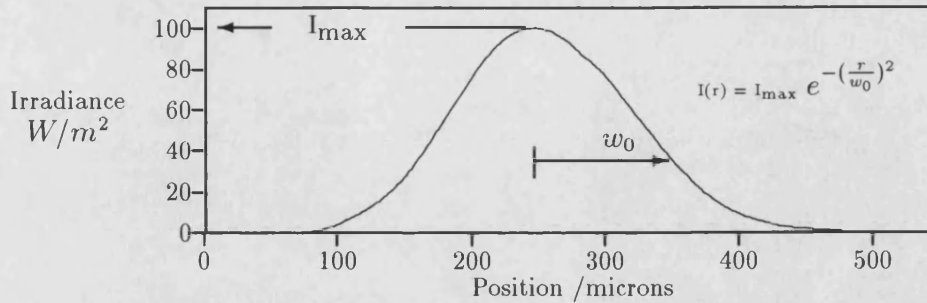
Figure 4.12: Measured TEM$_{00}$ mode Nd:YAG laser beam profile, and the corresponding mathematical form of the Gaussian distribution.

4.4.1   Temperature measurements on a silicon wafer.

After calibrating the system and measuring the temperature of a known source, measurement of temperature profiles generated on a 'standard' material with a well documented thermal conductivity is the next step needed to assess the accuracy of the system. The ideal test material should satisfy several criteria:

1. A high melting point, so that temperatures can be generated in the solid phase which are large enough to be detected. Ideally the melting point should be above 3000 K.

2. The material has to be opaque to the laser radiation, 1.064 μm.

3. Non-combustible, for obvious reasons!

4. Easily manageable, so that special handling equipment is not required.

5. A well documented thermal conductivity up to the melting point.

For the above reasons, silicon (melting point 1650 K) was selected as a suitable material. Other materials were originally tried, but some absorbed so much energy from the beam that it was hard to control the heating, and others, for example vitreous carbon, where portions of the sample were vaporised.

After the raw data has been recorded by the CCD , the array of numbers read from the detector are saved under a filename (eg. lc0930aa) with the extension *.asc* added to the end. When the temperature profile for this data set has been calculated, the results are saved in a file with an extension *.pqrs* which corresponds to the different mathematical analysis methods used by the OMA2T program. The effects of different analysis methods listed in table 4.1 on the resulting temperature profiles are shown in figure 4.13. The profiles shown in figure 4.13 agree

p	**Smoothing method**	Reference
1	No external smoothing	
3	Fourier smoothing	section 3.5.2
6	Unweighted 9-point moving average	section 3.5.1
q	**Symmetrisation**	
1	No symmetrisation	
2	Fourier symmetrisation	section 3.5.3
3	Two side averaging	
r	**Inversion**	
1	Nestor and Olsen method	section 3.3.1
s	**Fitting**	
1	Unweighted linear least squares	section 3.4.1
2	Weighted linear least squares	
3	Iterative reweighting regression	section 3.4.2
4	Non-linear least squares	section 3.4.3

Table 4.1: Types of analysis signified by file extension *.pqrs*.

well with each other in the centre region of the hot-spot, but diverge at the edges where the errors increase due to a reduction in the measured intensity of the

light.
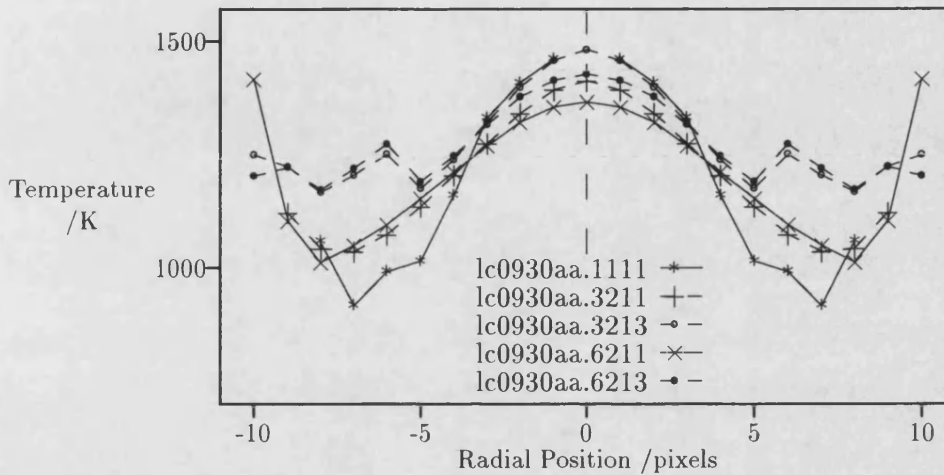
Figure 4.13: Temperature profile generated on silicon, demonstrating differnt analysis techniques.

The profiles generated have a peak temperature of 1430 K, which is below ihe melting point. When the laser power was increased, the silicon wafer crack:d, preventing a determination of the melting point to cross-reference to publisled values.

4.5   Melting point measurements obtained from temperature profiles.

4.5.1   Polycrystalline iron melting point determinatior.

A common experiment used by teachers to demonstrate the latent heat of fusion
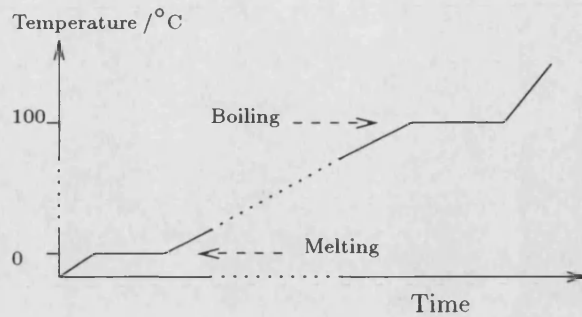
Figure 4.14: Demonstration of the latent heat of fusion and vaporisation of ice.

and vaporisation is to chart the temperature rise of a piece of ice as a constant heat is supplied to it. The recorded curve resembles that shown in figure 4.14, and the two flat sections of the curve coincide with the melting and boiling points of H_2O. By applying the same physical principles, the melting point of a sample can be determined from the flat section of the temperature profile generated by the Nd:YAG laser.
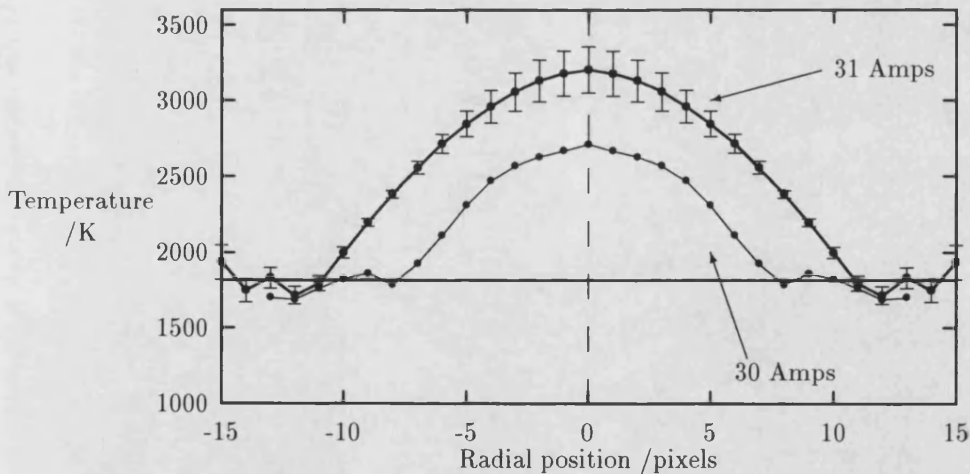
Figure 4.15: Temperature profile produced on iron showing melting.

The temperature distributions produced on a polycrystalline iron sample by the

laser operating at two different supply currents are shown in figure 4.15. From these two curves, it can be seen that there is a flattening of the profiles around 1800 K. The values of these temperatures, and their respective errors, are shown in table 4.2. The statistically averaged value of 1772 K ±30 K was produced for

Polycrystalline iron					
30 Amps			31 Amps		
Pixel	Temperature /K	+/−	Pixel	Temperature /K	+/−
			8	1784	154
			9	1858	350
			10	1822	435
11	1794	51	11	1762	533
12	1714	58	12	1686	617
13	1829	66	13	1703	1178
14	1748	78			
	1772.3	30.4		1790.4	125.9

Table 4.2: Melting point measurements for polycrystalline iron.

the profile generated with a laser flash lamp current of 30 Amps, and 1790 K ±126 K for the profile generated with a current of 31 Amps. The melting points for pure iron quoted in Kaye & Laby [63] and the 'Rubber Bible' [64] are 1813 K and 1808 K respectively. These values are within the margin of error for the melting points we have observed.

4.5.2 Melting point determination of stoichiometric uranium dioxide (UO_2).

Uranium dioxide does not meet the previously stated requirements for a 'standard' material, not only because it is toxic, but also because of the ease with

which UO_2 oxidises.

$$2UO_2 + O_2 \rightleftharpoons U_2O_3 + 1/2\,O_2. \tag{4.1}$$
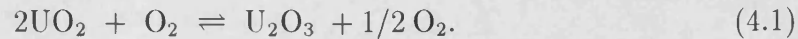
As long as correct procedures are adhered to in the handling of the uranium samples, the stoichiometric samples can be investigated in an atmosphere of argon and hydrogen so as to prevent the samples changing their composition. A decision by the Atomic Energy Authority (AEA) to build pressured water reactors has resulted in the physical properties of uranium dioxide being widely researched. The accepted melting point is that measured by Rand [65] at a temperature of 3120 K.
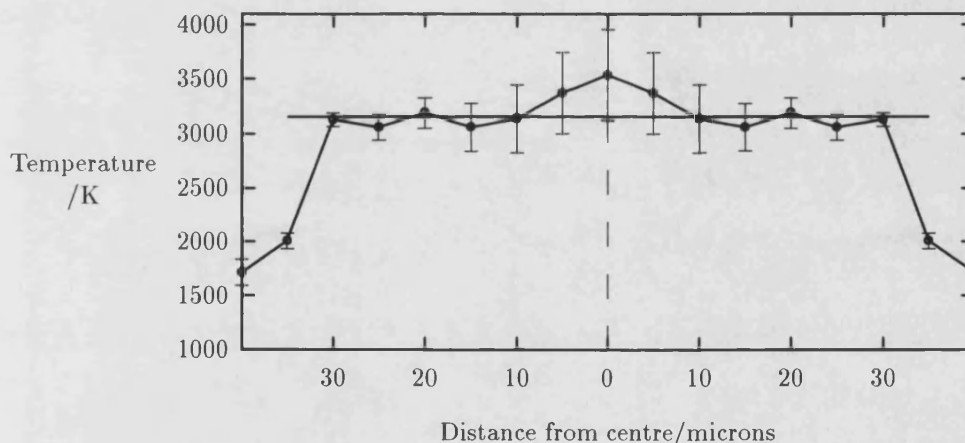
Figure 4.16: Temperature profile produced on UO_2 showing melting.

Uranium dioxide is a hard black material, and absorbs the laser radiation readily, and a current of 25 Amps supplied to the laser is all that is required to melt a sample. A temperature profile showing the characteristic flat section characteristic of melting is shown in figure 4.16. Statistical analysis of the melting temperatures shown in table 4.3 produces a value for the melting point of 3120 K ± 46 K, which equates to the value recommended by Rand [65].

Uranium dioxide		
25 Amps		
Pixel	Temperature /K	+/−
2	3139	309
3	3056	219
4	3189	138
5	3055	121
6	3126	56
	3120	46

Table 4.3: Measured melting point temperatures for UO_2.

4.6 Preliminary conclusions.

In the search for 'standard' materials with which to cross-check the accuracy of the OMA2T program, many radial temperature profiles were generated. Section 4.4.1 described measurements taken on a silicon wafer, which subsequently disintegrated under the power of the laser. Temperatures profiles generated on more robust samples of polycrystalline iron demonstrated that melting points could be determined.

Temperature profiles were generated on other samples, for instance uranium selenide and tungsten shown in figures 4.18a and 4.18d. As far as the author is aware, the melting point of uranium selenide does not seem to have been reported before. In our measurements (figure 4.18a) melting was not observed, therefore the melting point is expected to be greater than 1550±230 K. When these profiles for uranium selenide and tungsten are considered alongside profiles for uranium dioxide (figure 4.17) and silicon (figure 4.18b) which were all measured prior to melting, a characteristic 'bell' shape distribution can be ascribed to these profiles. If the Gaussian $1/e^2$ width of these 'bell' shape distributions are correlated
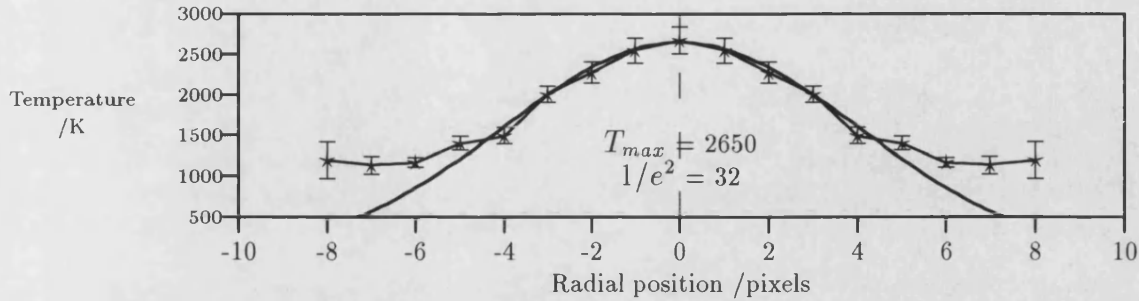
Figure 4.17: Temperature profile produced on uranium dioxide.

against the laser power supply current, as shown in table 4.4, then the different spectral emissivities cannot alone account for the disparity between T_{max}, and the $1/e^2$ width for different materials subjected to a similar laser power. This disparity suggests that the thermal conductivity of the material under test strongly influences the shape of the generated temperature profile.

Material	Flashlamp Current	$1/e^2$ /pixels	T_{max} /K	Emissivity		Ref.
				solid	liquid	
Si	30	80	1480	0.40		[66]
USe	23	85	1550			
W	28	200	2300	0.43		[63]
UO$_2$	24	32	2650	0.85		[63]
Fe	30	150	2700	0.35	0.37	[63]

Table 4.4: Effect of flash lamp current on peak temperatures and profile width.

This influence of the thermal properties of a material on the generated profile will be investigated in part II of this thesis.
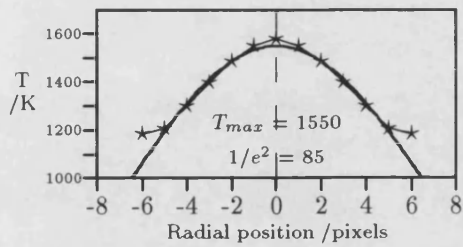
(a) Uranium selenide (23 A).
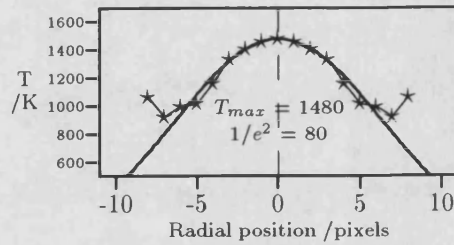
(b) Silicon wafer (30 A).
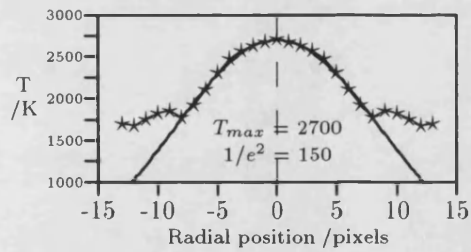
(c) Polycrystalline iron (30 A) - molten.
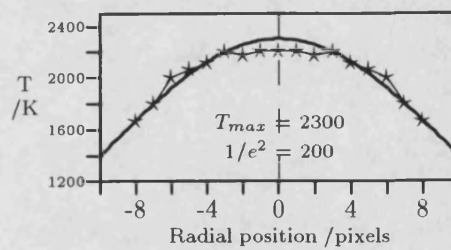
(d) Tungsten (28 A).

Figure 4.18: Temperature profiles produced on various samples.

Part II

Measurement of Thermal Properties.

Chapter 5

Methods for determining the Thermophysical Properties.

The ability to measure the melting points of materials remotely in itself is of use, although its applications are limited to the investigation of phase transitions under pressure or ambient conditions. We have developed techniques to measure the thermal properties and the melting point of a material remotely. The basis of these techniques derives from the heat conduction equation:

$$\rho C_p \frac{\partial T(\mathbf{r},t)}{\partial t} = \nabla \cdot [\kappa \nabla T(\mathbf{r},t)] + W(\mathbf{r},t). \tag{5.1}$$

In general, the thermal conductivity varies as a function of temperature, but to make the mathematics manageable, the temperature excursions are assumed to be small so that the value for κ can be assumed to be a constant. The heat conduction equation can then be simplified to the more familiar form shown below in equation 5.2.

$$\nabla^2 T(\mathbf{r},t) + \frac{W(\mathbf{r},t)}{\kappa} = \frac{1}{\alpha} \frac{\partial T(\mathbf{r},t)}{\partial t}. \tag{5.2}$$

Physical examination of this equation enables us to see how the thermal properties affect the heat distribution $T(\mathbf{r})$ in a material. The thermal diffusivity α determines the rate at which a sample heats up from the ambient temperature; therefore we can consider the thermal diffusivity to be synonymous with the transient response of the system. Likewise, the thermal conductivity κ determines the temperature distribution when the material has reached a steady state condition. As an example, consider a material with a small thermal conductivity and a small diffusivity subjected to a point source of heating; such a sample would take a long time to reach a steady state temperature distribution, and would have a much smaller spread of heat away from the source than for a material with a large thermal conductivity.

5.1 Steady state methods for determining the thermal conductivity.

5.1.1 Radial methods using thermocouples.

One of the most common configurations for thermal conductivity measurements is shown in figure 5.1. A long cylinder of material is used to reduce the analysis to a one dimensional problem, and the heat is supplied by a wire running down the middle of the cylinder so that the heat flows radially outwards from the centre. The temperature difference between two thermocouples situated at different radii is measured, which can then be used to obtain the thermal conductivity from
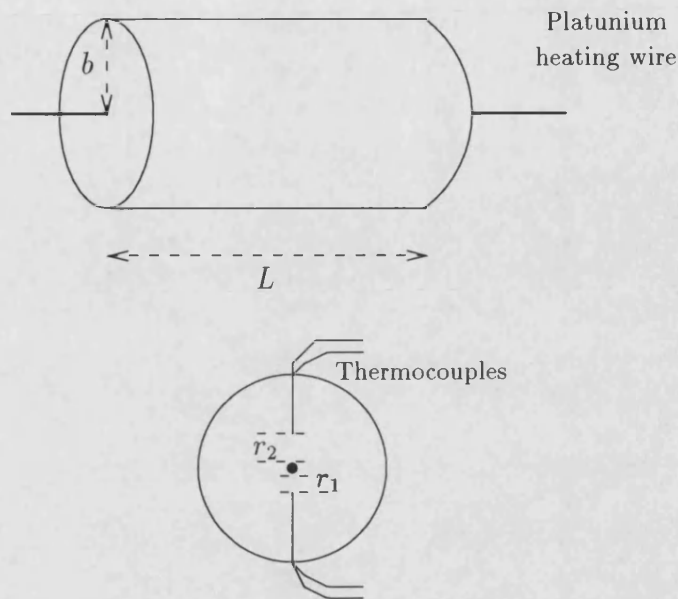
Figure 5.1: Configuration for radial heat flow measurements.

equation 5.3.

$$\kappa = \frac{W \ln(r_2/r_1)}{2\pi(T_1 - T_2)}. \tag{5.3}$$

W is the power density delivered to the sample by the platinum heating wire shown in figure 5.1.

Equation 5.3 is derived by considering two isothermal surfaces (T and $T + \delta T$) similar to those shown in figure 5.2, where the rate of heat flow (Q) through a small area (δA) is given by:

$$\frac{\partial Q}{\partial t} = -\kappa \, \delta A \cdot \frac{\partial T(r,t)}{\partial r}. \tag{5.4}$$

For an infinitely long cylinder, the area term equates to $\delta A = 2\pi r L$, and by using a typical length of $L = 1$m, equation 5.4 can be rewritten as:

$$\frac{\partial Q}{\partial t} = -\kappa \frac{\partial T(r,t)}{\partial r} \cdot 2\pi r. \tag{5.5}$$
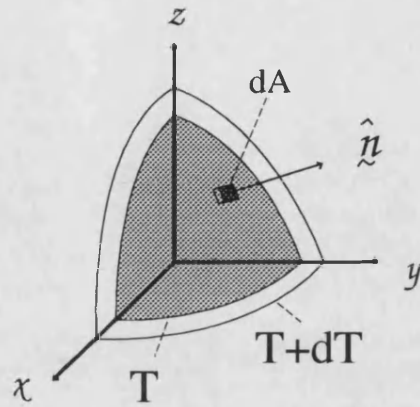
Figure 5.2: Two isothermal surfaces (T and T+∂T).

The rate of heat flow can also be written as the power delivered to the system (W). Substituting this into the above equation and rearranging, we can see that the thermal gradient is equal to a constant ($W/2\pi\kappa$) divided by the radial distance from the centre.

$$\frac{\partial T(r,t)}{\partial r} = -\frac{W}{\kappa 2\pi} \cdot \frac{1}{r}. \tag{5.6a}$$

The solution to this simple differential equation is well known:

$$T(r,t) = c \ln(r) + d. \tag{5.6b}$$

Due to the fact that we are measuring the temperature at two seperate radii, we now have two equations for $T(r,t)$. Taking the difference between them, we obtain an expression for the constant c which equates to the temperature difference divided by a ratio of the radii.

$$T_1 = c\ln(r_1) + d \tag{5.7a}$$

$$T_2 = c\ln(r_2) + d \tag{5.7b}$$

$$\Rightarrow \frac{(T_2 - T_1)}{\ln(r_2/r_1)} = c. \tag{5.7c}$$

Taking the expression for c above, and equating to the constant $-W/2\pi\kappa$, we arrive at the expression for the thermal conductivity stated earlier in equation 5.3.

$$\kappa = \frac{W}{2\pi} \cdot \frac{\ln(r_2/r_1)}{(T_1 - T_2)} \tag{5.7d}$$

$$\forall \quad r_2 > r_1.$$

5.1.2 Non-contact methods.

The method of determining the thermal conductivity outlined in section 5.1.1 requires thermocouples to measure the temperature at different radii, therefore it could not be used to measure the thermal conductivity of a material inside a Diamond Anvil Cell (DAC), or on any toxic material.

When a material is in thermodynamic equilibrium, the time derivative of the temperature becomes equal to zero and the heat conduction equation shown in equation 5.2 can be rewritten as:

$$\kappa = -\frac{W(\mathbf{r}, t)}{\nabla^2 T(\mathbf{r}, t)}. \tag{5.8}$$

This result implies that for a bulk material with no surfaces or defects to perturb the heat flow, the thermal conductivity can be directly evaluated by equating the heat input distribution to the differential of the temperature gradient.

The infra-red laser described in chapter 2 will produce heating at a depth below the surface of the sample. This depth is normally referred to as the skin depth of the laser, and if this depth is large enough to be able to ignore the perturbation of surface on the heat flow, then equation 5.8 would be valid. However, the

assumption that the thermal parameters do not vary with respect to temperature is likely to be violated by the large temperature gradients produced by the laser. The use of equation 5.8 to determine the thermal conductivity of a sample heated with the Nd:YAG laser will be discussed further in section 5.4.

5.2   Transient methods for determining thermal parameters.

Many different methods for determining the thermal properties, in particular the thermal diffusivity, have been devised [67–69]. To reduce complexity, all of the favoured methods use configurations which reduce the mathematical dimensions of the problem. For instance, if we use a long cylinder of material with axial heating, then we only have to consider one dimension. Similarly, if we consider a infinite slab, then the heat conduction problem reduces to a uni-directional problem.

Let us consider the radial heat flow configuration for a long cylinder described earlier and shown in figure 5.1, the governing heat conduction equation can be written in cylindrical coordinates as:

$$\frac{\partial^2 T(\mathbf{r},t)}{\partial r^2} + \frac{1}{r} \cdot \frac{\partial T(\mathbf{r},t)}{\partial r} + \frac{W(\mathbf{r},t)}{\kappa} = \frac{1}{\alpha} \cdot \frac{\partial T(\mathbf{r},t)}{\partial r} \qquad (5.9\text{a})$$

with the corresponding boundary condition

$$\frac{\partial T(\mathbf{r},t)}{\partial r} + \frac{h}{\kappa} T(\mathbf{r},t) = 0. \qquad (5.9\text{b})$$

The solution to this problem can be determined by using the Hankel transform,

which is a variation of the integral transform method described in Appendix A. The Hankel transform is sometimes referred to as the Fourier-Bessel transform, and deals explicitly with problems of cylindrical symmetry.

The Hankel integral transform is defined as,

$$\bar{T}(\lambda_m, t) = \int_0^b \mathbf{r}\, K(\lambda_m, \mathbf{r})\, T(\mathbf{r}, t) \cdot \partial r \tag{5.10a}$$

and its corresponding inversion formula by:

$$T(\mathbf{r}, t) = \sum_m K(\lambda_m, \mathbf{r})\, \bar{T}(\lambda_m, t). \tag{5.10b}$$

The analytical expression for temperature distribution $T(\mathbf{r}, t)$ can be obtained by using the appropriate kernel $K(\lambda_m, \mathbf{r})$ as determined by the relevant boundary condition, which in this case is shown by equation 5.9b. Then the temperature distribution can be shown [70] to be:

$$T(\mathbf{r}, t) = \sum_m K(\lambda_m, \mathbf{r})\, e^{-\alpha\lambda_m^2 t} \tag{5.11a}$$

$$\times \left[\bar{F}(\lambda_m) + \int_0^t A(\lambda_m, t)\, e^{\alpha\lambda_m^2 t} \cdot \partial t \right] \tag{5.11b}$$

where,

$$A(\lambda_m, t) = \frac{\alpha}{\kappa}\, \bar{W}(\lambda_m, \mathbf{r}) \tag{5.11c}$$

$$\bar{W}(\lambda_m, \mathbf{r}) = \int_0^b \mathbf{r}K(\lambda_m, \mathbf{r})W(\mathbf{r}, t) \cdot \partial r \tag{5.11d}$$

$$\bar{F}(\lambda_m) = \int_0^b \mathbf{r}K(\lambda_m, \mathbf{r})F(\mathbf{r}) \cdot \partial r. \tag{5.11e}$$

The appropriate kernel for the boundary conditions in equation 5.9b is,

$$K(\lambda_m, \mathbf{r}) = \frac{\sqrt{2}}{b}\, \frac{\lambda_m}{(H^2 + \lambda_m^2)^{1/2}}\, \frac{J_0(\lambda_m \mathbf{r})}{J_0(\lambda_m b)} \tag{5.12a}$$

with λ_m being the mth $+ve$ root of the transcendental equation :

$$\lambda J_1(\lambda b) = H J_0(\lambda b). \tag{5.13}$$

The implementation of the integral transform to determine the thermal properties

of a sample will be discussed later in section 5.3.3.

5.2.1   Non-contact techniques - application of "boxcar" integration.

It is not practicable to measure the temperature rise of a material inside a DAC

using thermocouples, but optical access to the sample is possible. To obtain the

temperature history of the sample, we build up the temperature at a given radius

from progressively time delayed data scans. This is illustrated in figure 5.3, where
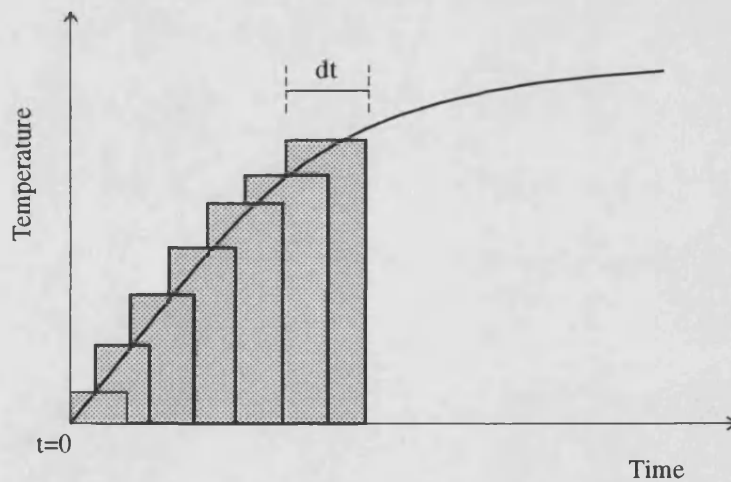
Figure 5.3: Development of temperature history using "boxcar" integration.

dt represents the exposure time of the CCD detector used in our experiment.

The temperature history can then be used to fit to the integral transform theory

described in the previous section.

5.3   Problems involving periodic boundary conditions - Ångström's method.

The steady state solution of heat conduction problems subjected to a boundary condition which is a periodic function of time is of interest in many engineering applications. If one end of a long cylinder is subjected to periodic variations of temperature, then the conductivity can be calculated from the phase of the thermal waves travelling down the cylinder, and the diffusivity calculated from the attenuation of the thermal waves. Ångström was the first to employ this method [71], which is distinguished by the neatness of the the experimental method and the mathematics.

There are two ways to consider this problem. Firstly, we could write the boundary conditions so that the ambient temperature varies as a function of time, or secondly, we could include heat generation on the surface of the sample. Both these approaches have been shown by the author to produce the same answer, but we shall only consider the second case where heat is generated in a small depth on the front surface.

5.3.1   Front face heat generation.

For some materials it is not possible to construct a long cylinder of the material, and keep its composition homogeneous. Therefore, we shall now consider the problem of heat conduction in a disc of material, as shown in figure 5.4. Let us
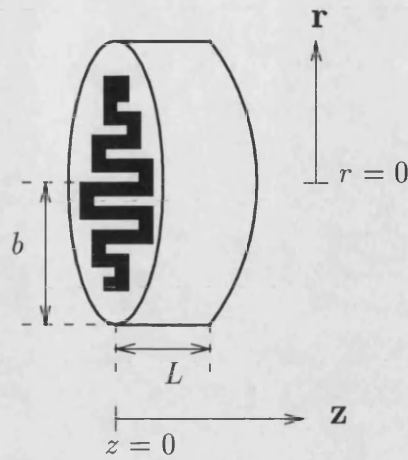
Figure 5.4: Configuration for Ångström's method.

consider the case where the heat generated is defined as a delta function δ_{0z}, at the front face of the sample ($z = 0$), and uniform in the radial direction. How this can be achieved experimentally is discussed in subsection 5.3.3. As we now have to consider two dimensions (radial and longitudinal) the governing equations for the configuration are slightly different from those shown earlier, and can be written as:

$$\nabla^2 T(\mathbf{r}, \mathbf{z}, t) + \frac{g(\mathbf{r}, \mathbf{z}, t)}{\kappa} = \frac{1}{\alpha} \frac{\partial T(\mathbf{r}, \mathbf{z}, t)}{\partial t} \tag{5.14}$$

where the boundary conditions are,

$$-\kappa \frac{\partial T(\mathbf{r}, 0, t)}{\partial \mathbf{z}} + hT(\mathbf{r}, 0, t) = hT_a \qquad |_{z=0} \tag{5.15a}$$

$$\kappa \frac{\partial T(b, \mathbf{z}, t)}{\partial \mathbf{r}} + hT(b, \mathbf{z}, t) = hT_a \qquad |_{r=b} \tag{5.15b}$$

$$\kappa \frac{\partial T(\mathbf{r}, L, t)}{\partial \mathbf{z}} + hT(\mathbf{r}, L, t) = hT_a \qquad |_{z=L} \tag{5.15c}$$

and the initial conditions are

$$F(\mathbf{r}, \mathbf{z}) = T(\mathbf{r}, \mathbf{z}, 0) = T_a. \tag{5.16}$$

The integral transform solution can then be written as the sums over the eigen-values:

$$T(\mathbf{r}, \mathbf{z}, t) = \sum_{n=1}^{\infty} \sum_{m=1}^{\infty} K(\lambda_n, \mathbf{z}) \, K(\beta_m, \mathbf{r}) \, \exp(-\alpha(\beta_m{}^2 + \lambda_n^2)t) \tag{5.17}$$

$$\times \quad \left[F(\mathbf{r}, \mathbf{z}) + \int_0^t \exp(\alpha(\beta_m{}^2 + \lambda_n^2)t') \cdot A(\beta_m, \lambda_n, t') \, \partial t' \right]$$

where

$$A(\beta_m, \lambda_n, t') = \frac{\alpha}{\kappa} \, \bar{g}(\beta_m, \lambda_n, t) + \alpha \sum_i \int_s \frac{K_i}{\kappa} hT_a \cdot \partial s \tag{5.18a}$$

$$\bar{g}(\beta_m, \lambda_n, t) = \int_{r=0}^{b} \int_{z=0}^{\infty} \mathbf{r} \, K(\beta_m, \mathbf{r}) \, K(\lambda_n, \mathbf{z}) \, g(\mathbf{r}, \mathbf{z}, t) \cdot \partial z \cdot \partial r \tag{5.18b}$$

$$F(\mathbf{r}, \mathbf{z}) = \int_{r=0}^{b} \int_{z=0}^{\infty} \mathbf{r} \, K(\beta_m, \mathbf{r}) \, K(\lambda_n, \mathbf{z}) \, T(\mathbf{r}, \mathbf{z}, 0) \cdot \partial z \cdot \partial r. \tag{5.18c}$$

The kernels for the boundary conditions in the $\mathbf{z}$ and $\mathbf{r}$ dimensions have been derived by Carslaw and Jaeger [72], and are:

$$K(\lambda_n, \mathbf{z}) = \sqrt{\frac{2}{\pi}} \cdot \frac{\lambda_n \cos(\lambda_n \mathbf{z}) + \frac{h}{\kappa} \sin(\lambda_n \mathbf{z})}{\left[\lambda_n^2 + (\frac{h}{\kappa})^2 \right]^{1/2}}$$

$$\equiv \quad Z \left(\lambda_n \cos(\lambda_n \mathbf{z}) + \frac{h}{\kappa} \sin(\lambda_n \mathbf{z}) \right) \tag{5.19a}$$

$$K(\beta_m, \mathbf{r}) = \frac{\sqrt{2}\beta_m}{b \left[(\frac{h}{\kappa})^2 + \beta_m{}^2 \right]^{1/2}} \cdot \frac{J_0(\beta_m \mathbf{r})}{J_0(\beta_m b)}$$

$$\equiv \quad R \, J_0(\beta_m \mathbf{r}) \tag{5.19b}$$

subject to the relevant transcendental equations for λ and β which are listed below:

$$\tan(\lambda L) = \frac{\lambda(\frac{2h}{\kappa})}{\lambda^2 - (\frac{h}{\kappa})^2} \tag{5.20a}$$

$$\beta \, J_1(\beta b) = \frac{h}{\kappa} J_0(\beta b). \tag{5.20b}$$

Note that R and Z above represent constants which are functions only of the eigenvalues, not position. The heating term $g(\mathbf{r}, \mathbf{z}, t)$ can be written as the product of three terms, shown below, which includes the sinusoidal time dependence of the heat input $g(t)$ as depicted in figure 5.5.

$$
\begin{aligned}
g(\mathbf{r}, \mathbf{z}, t) &= g(\mathbf{r}) \cdot g(\mathbf{z}) \cdot g(t) \\
&= 1 \cdot \delta_{0z} \cdot \left\{ (g_a + \delta g) + \delta g \sin(\omega t) \right\}.
\end{aligned}
\tag{5.21}
$$

Evaluating the integral transform of the heating term $(\bar{g}(\beta_m, \lambda_n, t))$, we use the
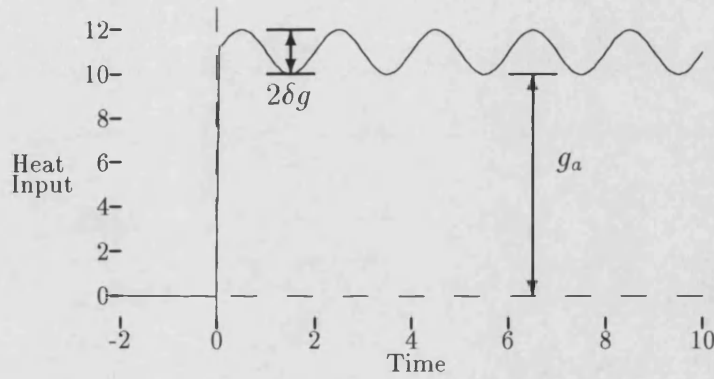
Figure 5.5: Time dependence for sinusoidal heating commencing at t=0.

properties of the delta function δ_{0z} for the heat input in the z direction, and the uniformity over the radial direction at the $z = 0$ face to simplify the expression.

$$
\begin{aligned}
\bar{g}(\beta_m, \lambda_n, t) &= g(t) \, K(\lambda_n, 0) \cdot \int_0^b r' \, K(\beta_m, r') \, g(\mathbf{r}) \cdot \partial r' \\
&= g(t) \, K(\lambda_n, 0) \, \frac{bR}{\beta_m} \, J_1(\beta_m b).
\end{aligned}
\tag{5.22}
$$

Before we calculate the $A(\beta_m, \lambda_n, t)$ term, we can simplify the second term on the right hand term of equation 5.18a, namely

$$
\sum_i \int_s \frac{K_i}{\kappa} h T_a \cdot \partial s = \frac{h T_a}{\kappa} \left\{ b \cdot K(\beta_m, b) - K(\lambda_n, 0) + K(\lambda_n, L) \right\}.
\tag{5.23}
$$

Therefore the term $A(\beta_m, \lambda_n, t')$ in equation 5.18a can be written in the form

$$A(\beta_m, \lambda_n, t) = C + D\sin(\omega t) \tag{5.24a}$$

where,

$$C = \frac{\alpha}{\kappa} \left[(g_a + \delta g)\frac{bR}{\beta_m} J_1(\beta_m b)\lambda_n Z \right. \tag{5.24b}$$

$$\left. + hT_a \left\{ RbJ_0(\beta_m b) + Z\left(\lambda_n \cos(\lambda_n L) + \frac{h}{\kappa}\sin(\lambda_n L) - \lambda_n\right) \right\} \right]$$

and

$$D = \frac{\alpha}{\kappa}\delta g\frac{bR}{\beta_m} J_1(\beta_m b)\lambda_n Z. \tag{5.24c}$$

The final term we need to evaluate is the integral transform of the initial conditions.

$$F(\mathbf{r}, \mathbf{z}) = T_a \int_0^b \int_0^L r\, K(\beta_m, \mathbf{r})\, K(\lambda_n, \mathbf{z}) \cdot \partial z \cdot \partial r \tag{5.25}$$

$$= \text{constant} = I_c$$

When these expressions (equations 5.22, 5.24a, 5.25) are substituted into the integral transform solution (equation 5.17), the analytic expression for the temperature can be finally written as

$$T(\mathbf{r}, \mathbf{z}, t) = \sum_{n=1}^{\infty}\sum_{m=1}^{\infty} K(\beta_m, \mathbf{r})\, K(\lambda_n, \mathbf{z})\, \exp(-et)$$

$$\times \left[I_c + \int_0^t \exp(et)\,(C + D\sin(\omega t))\,\partial t \right] \tag{5.26}$$

where $e = \alpha(\beta_m{}^2 + \lambda_n^2)$.

The time integral can be now evaluated as

$$\int \partial t = \left(\frac{C}{e}\exp(et) - \frac{C}{e}\right) + \left(\exp(et)\left[\frac{D}{e^2 + \omega^2}\left(e\sin(\omega t) - \omega\cos(\omega t) + \omega\right)\right]\right).$$

After multiplying through, the expression for the temperature distribution in a slab subjected to a periodic heat input can be simplified to

$$
\begin{aligned}
T(\mathbf{r}, \mathbf{z}, t) \;=\; & \sum_{n=1}^{\infty} \sum_{n=1}^{\infty} K(\beta_m, \mathbf{r}) \cdot K(\lambda_n, \mathbf{z}) \\
\times \quad & \{M - N \exp(-et) + P\,(e \sin(\omega t) - \omega \cos(\omega t))\}
\end{aligned}
\tag{5.27}
$$

where

$$
M \;=\; \frac{C}{e} + P\omega
\tag{5.28a}
$$

$$
P \;=\; \frac{D}{e^2 + \omega^2}
\tag{5.28b}
$$

$$
N \;=\; \frac{C}{e} - I_c.
\tag{5.28c}
$$

5.3.2   Physical interpretation.
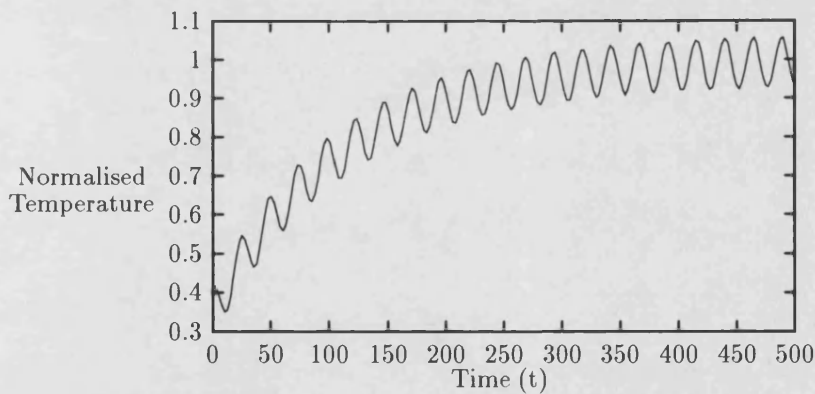
Figure 5.6: Theoretical temperature profile obtained by Ångström's method.

Closely inspecting equation 5.27, we can see that the temperature response takes the form of the $(1 - e^{-t})$ rise seen in radial heat flow experiments, but with a sinusoidal ripple imposed upon it, similar to that shown in figure 5.6.
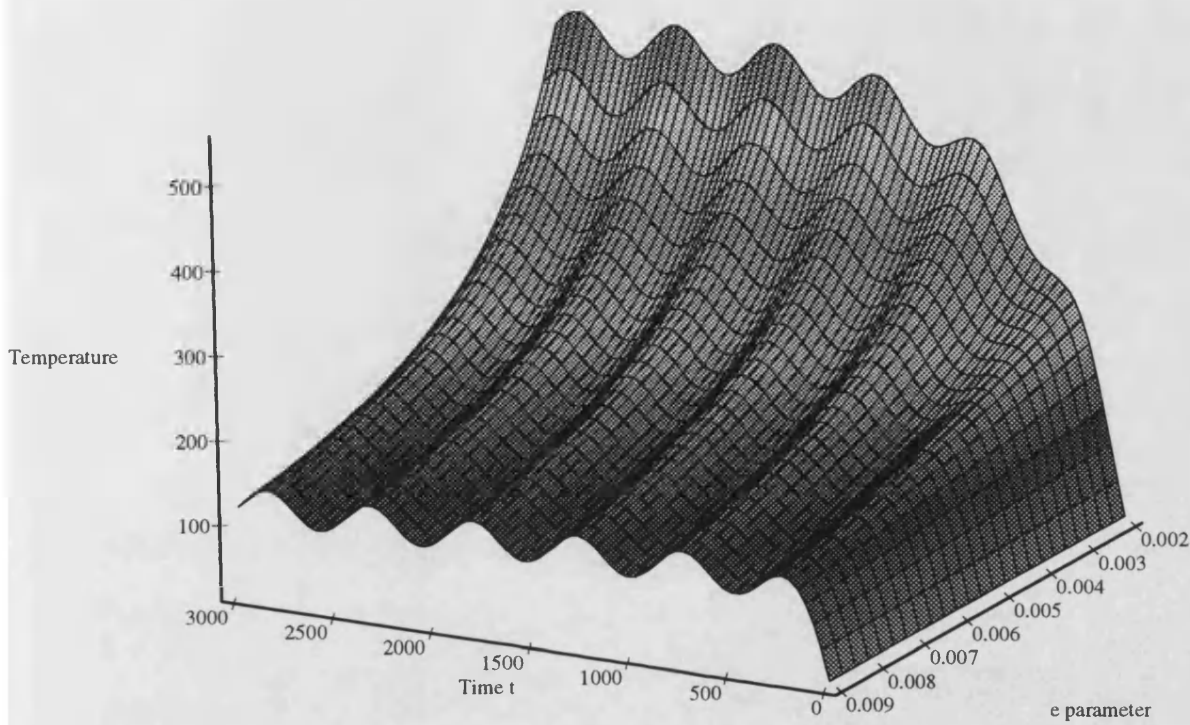
Figure 5.7: Theoretical temperature response with varying parameter $e = \alpha(\beta_m{}^2 + \lambda_n^2)$; setting $a = 1, b = 2, \omega = 1/84$.

The thermal diffusivity only appears in the terms in equation 5.27 containing the parameter e, and by plotting how the temperature response varies with the parameter e, we can determine how the thermal diffusivity effects the temperature history for this configuration. As can be seen from figure 5.7, the diffusivity not only effects the the rate of temperature rise, but also the magnitude of the temperature, which varies as $\frac{\kappa}{\alpha}$. This result is different from that obtained by the steady heating methods discussed previously, where the thermal diffusivity only affected the rate of temperature rise, with the thermal conductivity alone
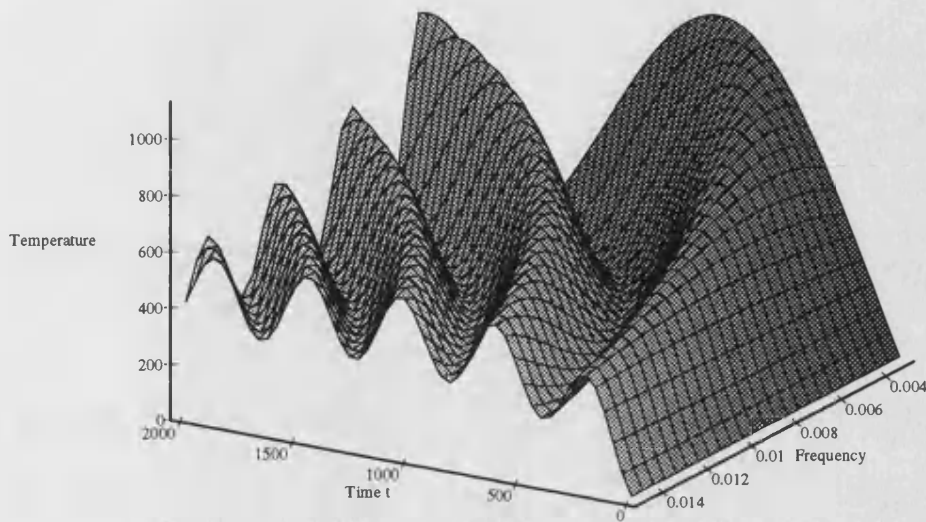
Figure 5.8: Temperature response with varying frequency;setting $a = 1, b = 2, e = 0.003$.

determining the magnitude of the temperature.

The effect of changing the driving frequency ω by a small percentage is very marked. Figure 5.8 shows that the driving frequency affects not only the number of troughs in a given time period, which would be expected, but also dramatically affects the magnitude of the temperature. This dependence of the temperature history on the driving frequency illustrates the need for a frequency stable power supply to be used, and even more importantly, accurate determination of the driving frequency.

5.3.3　Experimental implementation of Ångström's method.

A gold resistive element strip was evaporated onto a disc of Pyroceram 9606 which had dimensions 15.9 mm thick by 3.54 mm in diameter. The voltage generated across the thermocouple attached to the rear face of the sample was recorded by a digital multimeter linked to a PC using specialised software associated with the PC mounted GPIB interface board.

Initially, to establish that the system was working correctly, a finite heat pulse of 10 milliwatts was applied to the front face via the resistive heating strip, and the rear face temperature measured. This is essentially the same situation as used in laser flash methods, but here the sample cannot be considered to be an infinite slab. Theory predicts the temperature response for this system to be:

$$T(\mathbf{r}, t) = \sum_{n=1}^{\infty} \sum_{m=1}^{\infty} K(\beta_m, \mathbf{r}) K(\lambda_n, \mathbf{z}) \exp(-et) \int_0^t \exp(et) \left(A\, g(t) + B \right) \partial t. \quad (5.29)$$

For a heat pulse $g(t)$ which was turned on at a time t_1 and turned off a fixed time later, the shape of the expected temperature response should have that of a sharp rise in the temperature, followed by a steady cooling starting a small time after the heater was switched off. The thermocouple output voltage recorded is shown in figure 5.9, and seems to agree well that predicted by equation 5.29.

To generate the modulating heat input, a function generator was used as the power supply, and heat was delivered to the sample through the resistive strip at a nominal driving frequency of 0.01 Hz. As has been shown earlier (figure 5.8), the form of the temperature history is very susceptible to the driving frequency, and therefore it must be known accurately. The driving frequency can be obtained
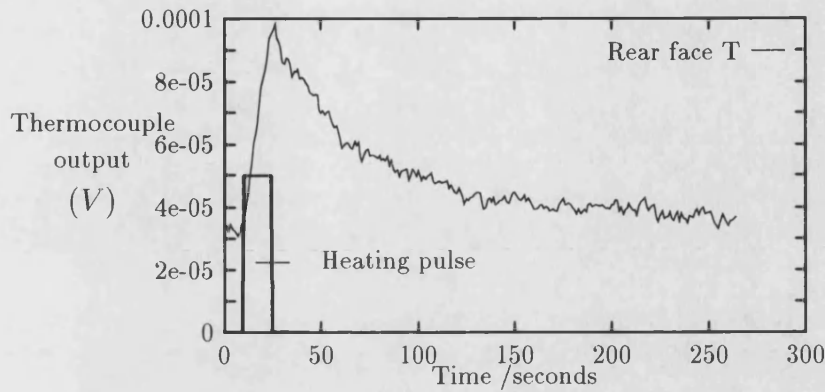
Figure 5.9: Heating and cooling curve for a finite heat pulse.
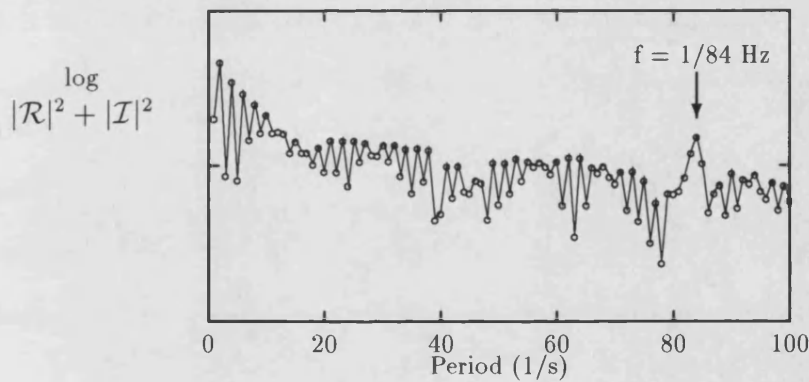
Figure 5.10: Power spectrum of sinusoidal temperature response.

from the measured data by taking the power spectrum, and recording the period of the prominent spike. This is shown in figure 5.10, with the driving frequency being 1/84 Hz (0.0119 Hz), which compares with the nominal frequency on the signal generator reading being 0.01 Hz.

For this particular experiment, the temperature response was recorded at the rear face of the sample using a thermocouple, and the sample was at ambient conditions. The normalised temperature recorded at the rear face is plotted in

figure 5.11.
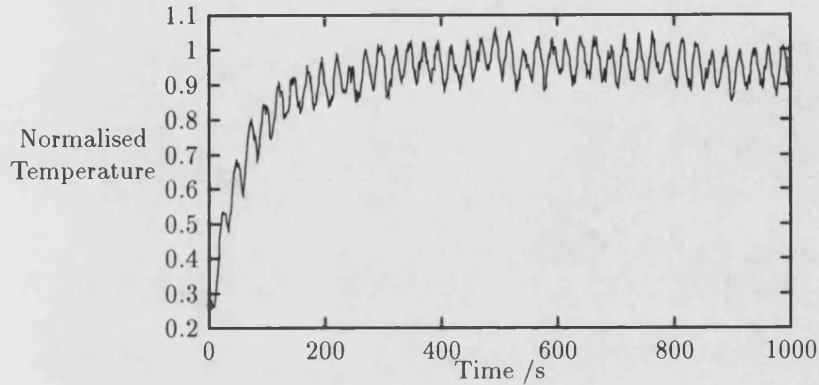
Figure 5.11: Measured temperature response for sinusoidal heat input.

It would be as easy to measure the rear face temperature with an optical pyrometer, with the sample mounted inside either a furnace or a cryostat, and the heat being supplied by a laser with its output modulated by an electro-optic device, so as to produce a sinusoidal heat input.

5.3.4 Fitting to parameters using nonlinear techniques.

To extract the thermal constants (thermal conductivity and diffusivity) from the measured data, we need to fit the data to the integral transform theory represented by equation 5.27. As this expression is not linearly reducible, the most efficient scheme to use is the Modified Gauss-Newton nonlinear fitting method, which has been outlined earlier in section 3.4.3. With the radial heat flow method described in section 5.2, the fitting routine converged quickly and the transcendental equation 5.20 was continuous, so the program used to fit to the thermal
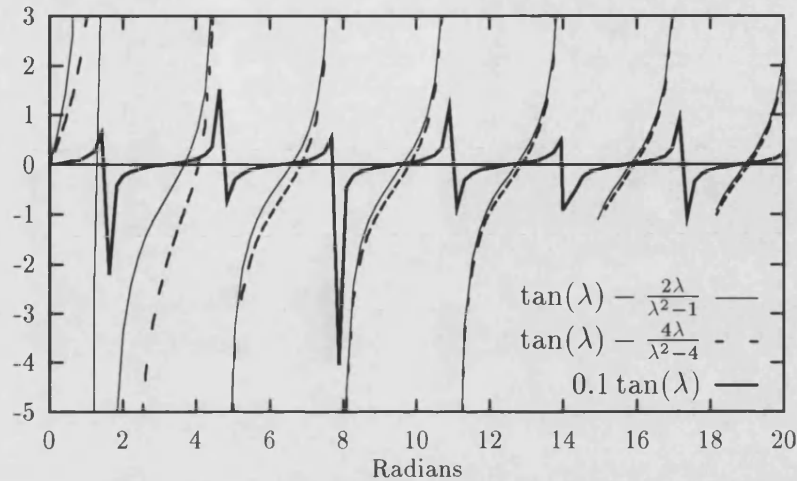
Figure 5.12: Roots of the linear transcendental equation.

parameters was relatively simple. Now that we are considering a finite slab, we have to solve the transcendental equation for the z direction (equation 5.20), as well as the radial transcendental equation. As this involves a function of tan, the equation is discontinuous at multiples of $\pi/2$ (see figure 5.12) and therefore we cannot employ conventional root finding algorithms such as bisection or Runge-Kutta methods without carefully selecting the ranges over which they operate.

5.4 Parameter determination using a regression method in conjunction with Finite-Element Analysis.

Because of the large temperatures gradients involved in generating a 'hot-spot' with a laser, and the effect of thermal radiation loss from the sample, it would be inaccurate to assume that the thermal conductivity remains constant. The heat

conduction equation could be rewritten to incorporate the thermal conductivity as a function of temperature, but the effect of thermal radiation from the sample introduces a highly nonlinear boundary condition and the problem becomes analytically insoluble.

To model these effects, a finite element analysis (FEA) program was written to reproduce theoretically the temperature profiles generated experimentally by the laser on the surface of a sample of stoichiometric Uranium Dioxide. Initially, FEA program used the thermal conductivity distribution recommended by Harding and Martin [73] which is shown in figure 5.13. The two theoretically generated
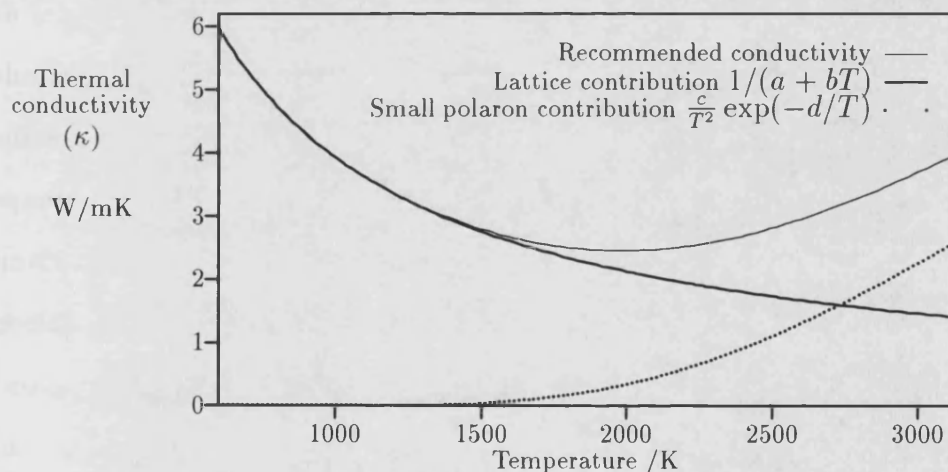
Figure 5.13: Recommended form of the thermal conductivity (κ) of UO_2 .

temperature profiles in figure 5.14 show the difference between the analysis using solely convective boundary conditions, and the analysis incorporating radiation from the surface. Even at these relatively low temperatures, the difference is quite marked.
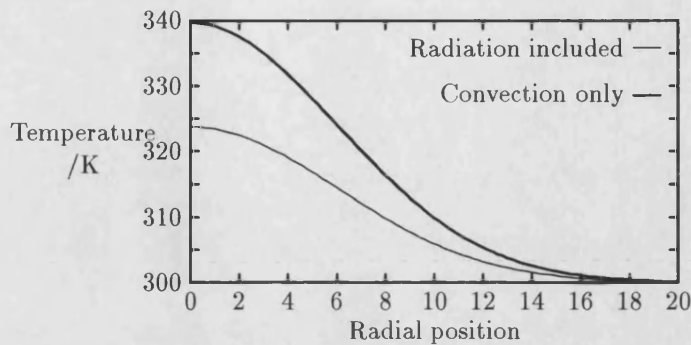
Figure 5.14: Generated temperature profiles using different boundary conditions.

Using this finite element analysis routine, it is easy to check the effect that a finite sample radius size has on the final temperature profile. This is achieved by starting with a temperature profile generated on a sample with a large radius to length ratio by the laser with a beam width much smaller than the radius of the sample, and then calculating the difference by sum of square residuals for subsequent profiles as the edges are 'rolled' in. The magnitude of the sum of squares is greater than unity because the profiles were not normalised, but left unaltered so that a change in the peak temperature, as well as the shape of the profile could be monitored. A radius to length ratio of approximately 5:1 was the previously accepted minimum value, but from figure 5.15 it can be seen that ratios as low as 2:1 could be used before any edge effects start to detrimentally affect the generated temperature profiles. A similar result can be seen in figure 5.15, where the radius to sample length was kept constant at 5:1, and the radius to laser beam width ratio was varied.

The generated profiles shown in figure 5.14 have a Gaussian temperature distribution with respect to position, which would produce a discontinuity in the
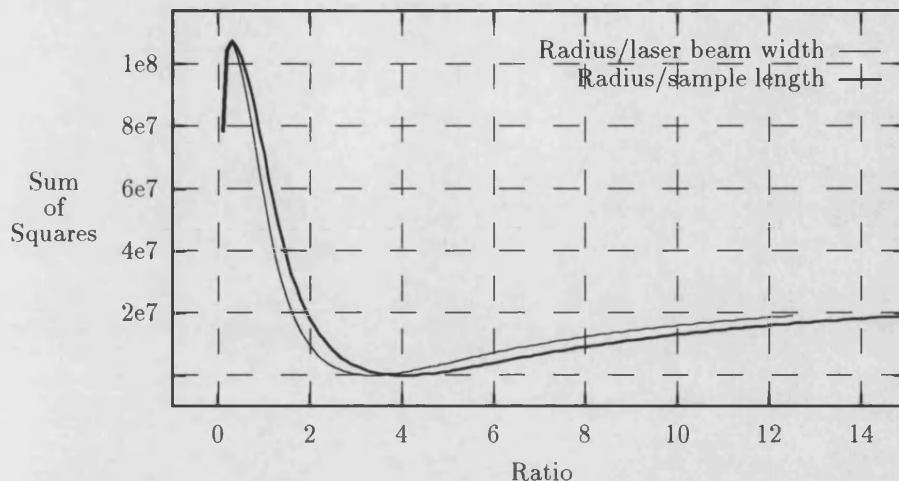
Figure 5.15: Effect of 'infinite' slab analysis.

thermal conductivity calculated according to equation 5.30:

$$\kappa \;=\; -W(\mathbf{r}) \,/\, \nabla^2 T(\mathbf{r}, t). \tag{5.30}$$

This discontinuity is shown in figure 5.16, and is not the shape of the thermal conductivity used to generate these temperature profiles, namely the function shown in figure 5.13. This result is not surprising when you consider the fact that the laser produces heat close to the front surface of the sample, therefore, in no way could this situation be considered a 'bulk' situation where equation 5.30 would be valid. We propose that it is possible to obtain the parameters (a, b, c and d in figure 5.13) related to the thermal conductivity by fitting the measured steady state temperature profile to the FEA generated temperature profiles.

If the peak temperature of the profile is less than 1600 K, from figure 5.13, we can see that the lattice contribution to the thermal conductivity dominates, and hence a and b are the dominant parameters we should try to fit to. A plot
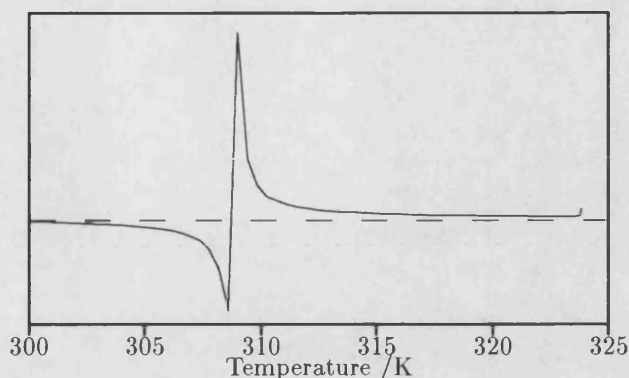
Figure 5.16: Calculated thermal conductivity!

of the residual sum of squares for such a case is shown in figure 5.17. The presence of a clear minimum, and the absence of localised minima, indicates that a nonlinear fitting routine can converge quickly to the desired values. Once the peak temperature exceeds 2000 K, the effect of small polarons becomes significant (figure 5.13). As we can see from figure 5.18, the minimum is not as obvious as for the lattice component case, and some localised minima are also present. To avoid convergence to the wrong minima, a good initial guess for c and d parameters is needed. Alternatively, sum of square residual contour maps similar to figures 5.17 and 5.18 can be constructed for each measured temperature profile to suggest the best starting values for the parameters, which are then passed to the nonlinear fitting routine to assist rapid convergence.

If the effect of scattering by dislocations is included, the form of the thermal conductivity should be written as shown in equation 5.31:

$$\kappa(T) \;=\; \frac{1}{a+bT} \;+\; \frac{c}{T^2}\exp(-d/T) \;+\; e\exp(-f/T). \tag{5.31}$$

For polycrystalline samples, it is thought that this effect will be swamped by
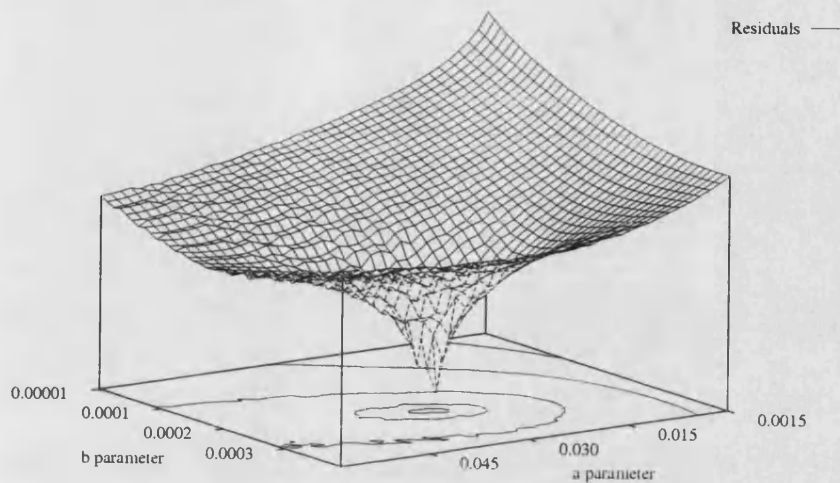
Figure 5.17: Sum of square residuals for lattice contribution,$1/(a + bT)$.
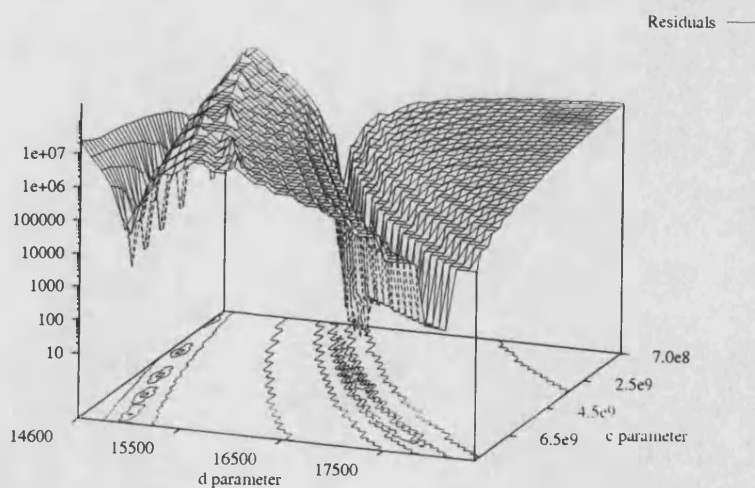
Figure 5.18: Sum of square residuals for small polaron contribution,$(c/T^2)\exp(-d/T)$.
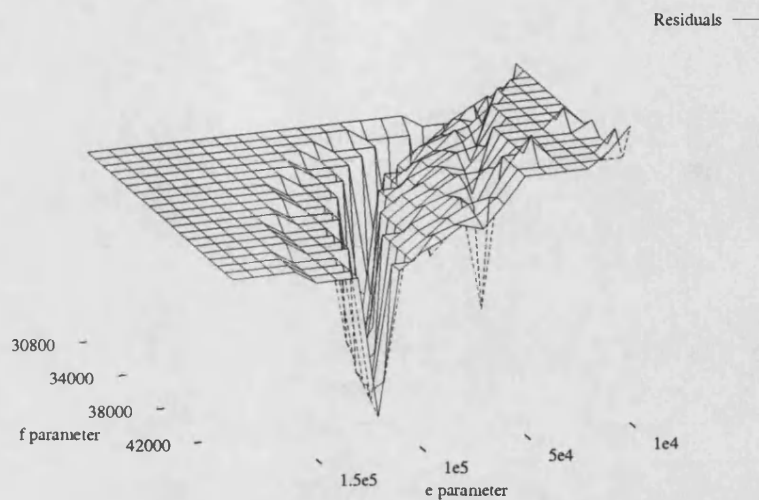
Residuals ——

Figure 5.19: Sum of squares residuals for the dislocation contribution.

the other two mechanisms, and therefore it was not incorporated into the final analysis. This is fortunate, as the sum of square residual contour map for the dislocation contribution shown in figure 5.19 is confused, with more than one obvious minimum. This would result in an unstable convergence in the Gauss-Newton nonlinear fitting routine.

5.5   The effect of noise on non-linear regression method.

In the previous sections we have considered the effect that each mechanism of heat conduction has on the final temperature profile. All the residual maps shown in section 5.4 were calculated using perfectly smooth data sets, but the effect of adding noise to these profiles could have easily masked the desired minima. To

investigate this effect, we recalculated the residual maps shown previously, but for temperature profiles with various amounts of Poisson noise added to them. These radial temperature profiles are shown in figure 5.20.
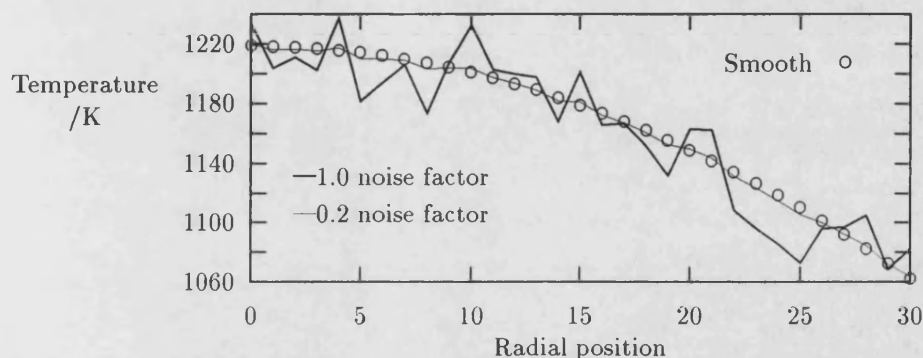
Figure 5.20: Temperature profiles with added Poisson noise.

The effect of noise on the residual plot for the lattice contribution to the thermal conductivity is quite marked, with residual plots for temperature profiles with noise factors of 1.0 and 0.2 shown in figure 5.21. The residual plot corresponding to a noise factor of 1.0 is the upper one of the two curves, and even though a slight dip in the curve exists, it is very shallow and is unlikely to produce the correct answer in any subsequent regression. The lower graph corresponding to a noise factor of 0.2 is imperfect when compared to figure 5.17, but would result in a converged result for the regression analysis, as it possesses a definite minimum.

When we consider the effect noise has on the residual plot for the small polaron contribution, we can see from figure 5.22 that the effect of noise is not as marked as for the lattice contribution. As the small polaron contribution dominates

Noise factor 0.2 ——
Noise factor 1.0 ······

a parameter
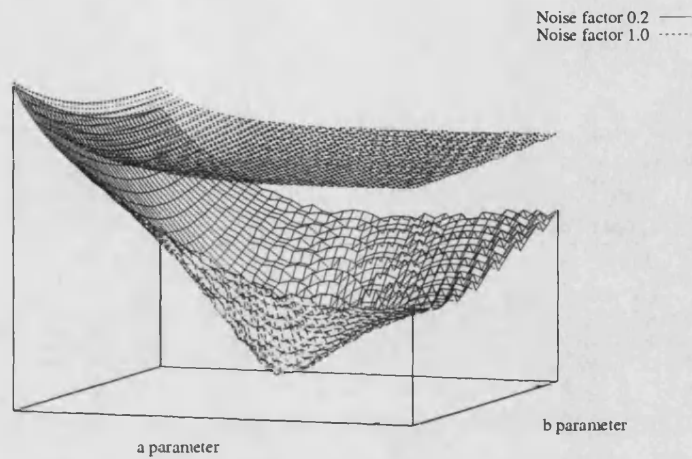
b parameter

Figure 5.21: Effect of noise on the lattice contribution of thermal conductivity.

the thermal conductivity at higher temperatures, we would expect to be able to converge to the correct parameters for the polaron contribution even for noisy temperature profiles, as long as the peak temperature is large enough.

The calculated sum of square residuals for the lattice contribution of the thermal conductivity has been shown to be quite susceptible to noise, so to characterise fully the thermal properties of a material from a single temperature profile, we need to know the level of noise present in the temperature profile to facilitate efficient smoothing. The determination of the level of noise will be investigated in the next section.
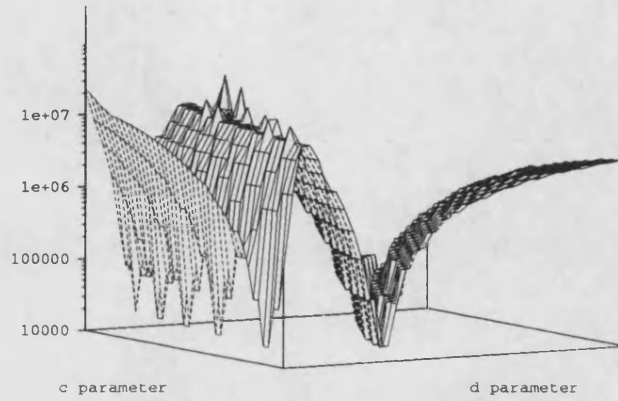
(a) Noise factor 0.2.
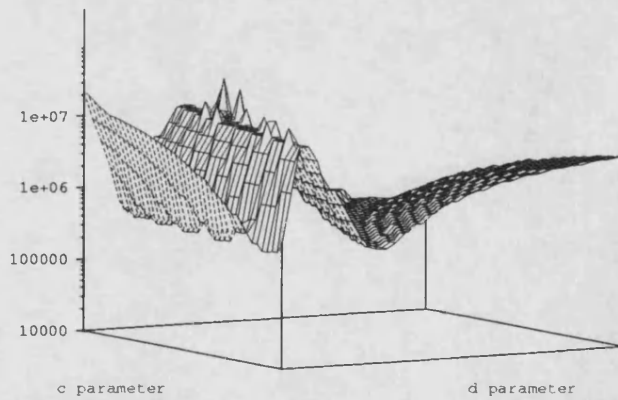
(b) Noise factor 1.0.

Figure 5.22: Effect of noise on small polaron contribution.

5.5.1 Determination of noise factors.

The power spectrum $S(\omega)$ of a function can be determined from its real and imaginary Fourier components,

$$S(\omega_j) = |\mathcal{R}_j|^2 + |\mathcal{I}_j|^2. \qquad (5.32)$$

Here $\mathcal{R}$ and $\mathcal{I}$ are the respective real and imaginary Fourier components of the real space function under investigation. For a noisy function, we can expect the power spectrum to be biased towards the higher frequencies, as the noise will have a basis comparable to the sampling length. This can be seen in figure 5.23 where the power spectrum of a smooth data set is compared with a data set with an applied noise with a Poisson factor of 1.0. If we calculate the ratio of the sum
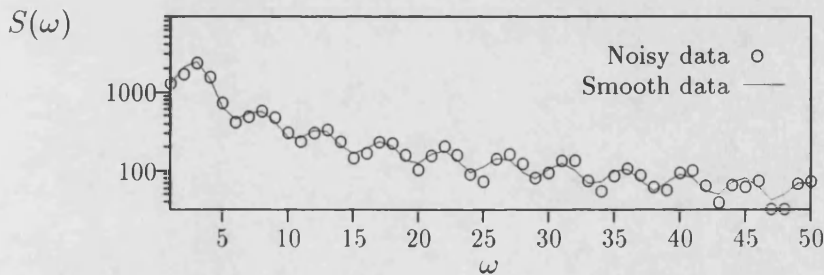
Figure 5.23: Power spectra for two radial temperature profiles, one of which is noisy.

of the high frequency components to the sum of the low frequency components, and compare this to the Poisson noise factor, we obtain a linear relationship. This enables us to calculate the amount of noise on any given data set, which in turn is used calculate the size of the lag window needed to smooth the data set efficiently. This method bears some resemblance to Wiener filtering [74], except

that it does not require any input from the user (for example an idealized signal) once the method has been coded into an analysis program.

Chapter 6

Results of thermodynamical analysis.

In the previous chapter, several approaches which could be used to measure the thermal properties of materials were discussed. Results obtained by some of these methods will be presented in this chapter, but emphasis will be placed on those techniques which can determine the thermal properties of a material remotely.

6.1 Measurement of the radial heat flow using thermocouples.

In the determination of the thermal properties by measurement of the radial temperature distribution, the condition that the heat flow is purely radial is required for the mathematical analysis to be valid. The most effective way to ensure that this condition is met, is to use a long cylinder and measure the temperature

distribution in the middle. Theoretical consideration [75] has suggested that a length to radius ratio of at least 10:1 is required to ensure a laminar flow of heat in the centre of the cylinder.

For some materials, it is relatively easy to place the thermocouples in the the centre of the cylinder, but for others, it is only practicable to make discs. To ensure that laminar flow is obtained around the measurement points, discs are stacked tightly together to form a long cylinder. An additional advantage of using a stack of discs, is that the interfaces between successive discs provide resistance to the longitudinal flow of heat, hence isolating the centre disc further from any end effects.

6.1.1 Green phase yttrium barium copper oxide.

Discs made from the tetragonal non-superconducting green phase of yttrium barium copper oxide, were drilled and fitted with an Kanthal axial heating wire as shown in figure 6.1. $Y_2Ba_2CuO_5$ was chosen because of the ease of construction
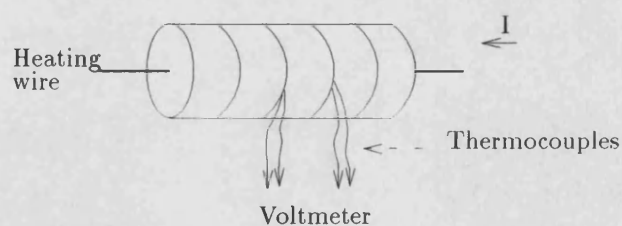
Figure 6.1: A long cylinder made from a stack of discs.

of the 12mm by 2mm discs, and also because this material is soft enough to be drilled using conventional drills. The green phase was chosen over the more

Ambient temperature = 573 K
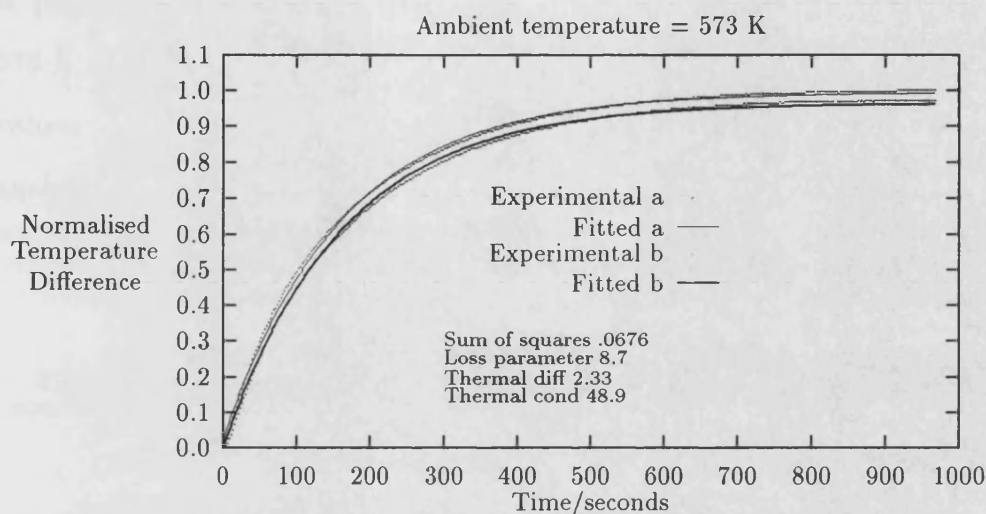
Figure 6.2: Measured temperature history curves for $Y_2Ba_2CuO_5$ at 573 K

commonly studied superconducting black phase ($YBa_2Cu_3O_{7-\delta}$) to prevent the need to pass oxygen over the sample when mounted in the furnace, which would present a significant safety risk.

A typical temperature response to a 'step' heating input for a sample maintained at an ambient temperature of 573 K is shown in figure 6.2. The temperature histories of two radial positions were recorded by a digital voltmeter, and the recorded histories were compared to the integral transform theory described in section 5.2. If the radial position of the thermocouples is accurately known, then a nonlinear fitting routine can be used to fit each measured temperature history to theory separately. However, it was found that greater accuracy in the fitting could be achieved by fitting the temperature histories from *both* thermocouples to the integral transform theory simultaneously, thus making the fitting routine converge to the same minimum for both curves.

A profile recorded with the sample maintained at an ambient temperature of 573 K is shown in figure 6.2, with the fitted thermal parameters also shown. The values for the thermal conductivity (κ) and diffusivity (α) obtained were collated against the ambient temperatures, and are shown in figures 6.3 and 6.4.
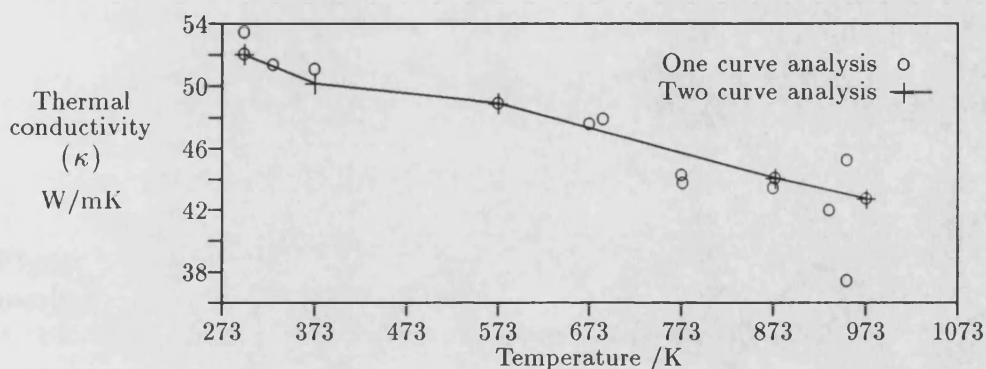
Figure 6.3: Thermal conductivity of $Y_2Ba_2CuO_5$ obtained using the radial heat flow method.
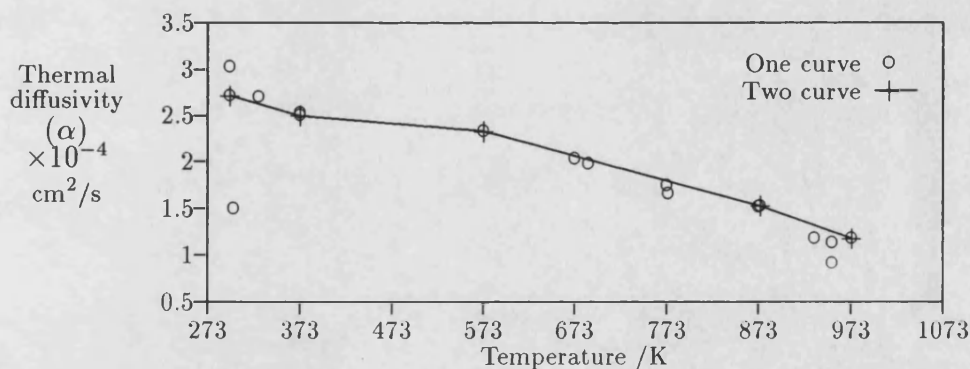
Figure 6.4: Thermal diffusivity of $Y_2Ba_2CuO_5$.

The convective heat loss parameter values (h) determined from the integral transform solution are shown in figure 6.5, which demonstrates a T^4 temperature dependence. This dependence indicates that convective cooling from the cylinder's
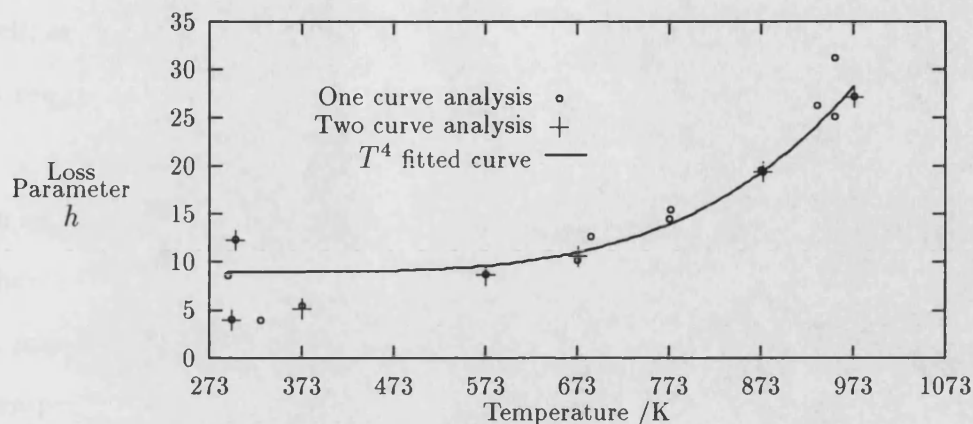
Figure 6.5: Values for the loss parameter obtained using the radial heat flow method compared to thermal radiation dependence.

surface is supported by thermal radiation transfer effects.

As far as we are aware, no measurements have been made of the thermal properties of the tetragonal compound $Y_2Ba_2CuO_5$, so no comparison can be made with published data. However, the temperature dependence of both the thermal conductivity (figure 6.3) and diffusivity (figure 6.4) suggest that 'Umklapp' phonon scattering and grain boundary scattering processes dominate the conduction methods, which would be expected from a porous granular material.

6.2   Thermal parameters extracted from measured temperature profiles.

The results shown in section 6.1 were obtained using thermocouples attached to the sample to measure the temperature. If we wish to measure the thermal

properties of materials under the extreme pressures generated by a diamond anvil cell, or measure the thermal properties of toxic materials, a non-contact method is required.

In section 5.4, a method of fitting a measured temperature profile to a theoretical thermal conductivity dependence was described. The thermal conductivity of a material usually controlled by three dominant mechanisms, which affect the temperature dependence of the conduction of heat in different ways:

1. Scattering of phonons, mainly by grain boundary scattering (a) and three phonon 'Umklapp' processes (b), but also could include four phonon scattering (β).

$$\kappa_{latt}(T) \;=\; 1/\left(a + bT + \beta T^2\right). \tag{6.1}$$

2. Electronic contribution, namely small polarons.

$$\kappa_{elec} = cT \, \exp(-d/T). \tag{6.2}$$

3. A conduction decrease due to dislocations, normally only apparent at very high temperatures.

$$\kappa_{disc} \;=\; e\exp(-f/T). \tag{6.3}$$

To demonstrate the ability of the Gauss-Newton nonlinear fitting routine to fit to a measured temperature profile, a two parameter form of the conductivity was used to aid visualisation. Predetermined values for a and b were used to generate a theoretical temperature profile with the finite element (FEA) thermal analysis
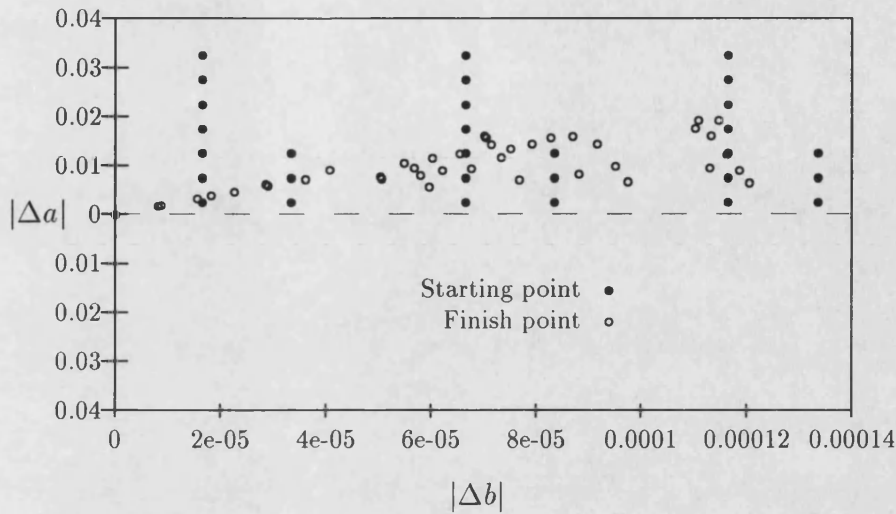
Figure 6.6: Convergence of nonlinear fitting routine.

program written by the author, which uses an implicit scheme to incorporate thermal radiation effects. Different starting values for a and b were chosen, and the final values for a and b determined by the fitting routine were recorded. Figure 6.6 shows the absolute difference between the 'true' values and the starting and finishing values of a and b. There is a cluster around the origin which demonstrates that the regression method described in section 5.4 can converge to the 'correct' values.

The temperature profiles generated by the laser are all measured when the test material has reached a steady state condition, so no temperature history of the material subjected to continuous laser heating is recorded. Therefore it is futile to try to extract any thermal diffusivity information from the measured temperature profiles. To generate the theoretical temperature profiles, the finite element analysis routine uses values for the thermal diffusivity measured using laser flash techniques [76, 77]. The use of thermal diffusivity values obtained by the laser

flash method does not violate the remote sensing criterion, as the flash method can be employed remotely [78] using optical pyrometers and thermal radiation detectors to measure the temperature history.

6.2.1 Measurements on Pyroceram 9606.

Pyroceram 9606 [79] is a hard white glass ceramic which is likely to be employed in the future as a 'standard' for low thermal conductivity materials.
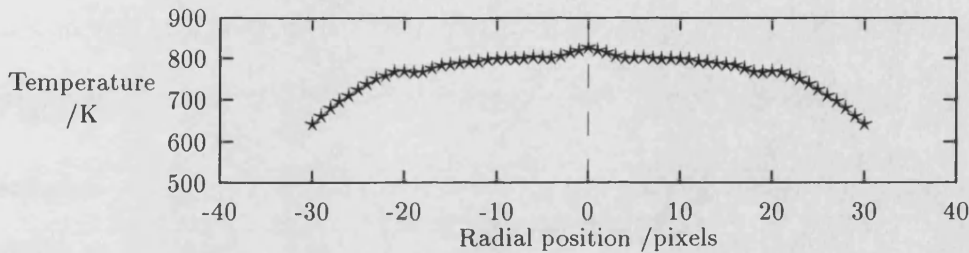
Figure 6.7: Temperature profile produced by the laser on Pyroceram.

A laser flashlamp current of 24 Amps was used to generate the temperature profile shown in figure 6.7. This profile, in conjunction with the recommended thermal diffusivity [80], was used to calculate the thermal parameters using the regression method. As Pyroceram is an electrically insulating ceramic, phonon scattering off grain boundaries and three phonon processes is expected to dominate, with little to no electronic contribution. The thermal conductivity then takes the form:

$$\kappa(T) \;=\; \frac{1}{a + bT} \;+\; cT \exp(-d/T). \tag{6.4}$$

Initial values for the coefficients a, b, c and d shown in table 6.1 were used by the fitting program, and initially the sum of square residual maps were generated
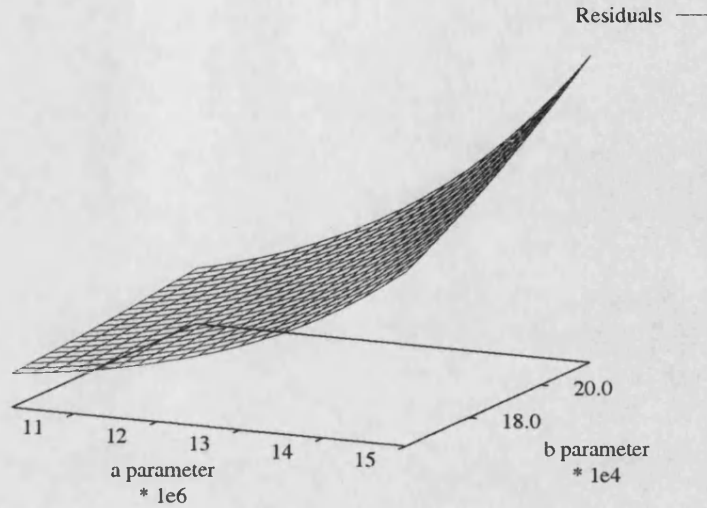
Figure 6.8: Sum of square residual plot for the lattice contribution of Pyroceram.

around these starting points. The residual map corresponding to the lattice contribution is shown in figure 6.8, and suggests that the values for a and b should lie in the region below $a = 10.0 \times 10^6$ and $b = 16.0 \times 10^4$. Similarly, the residual map for the polaron contribution is shown in figure 6.9, and its flatness suggests that the effects of small polarons are negligible in temperature region which we are considering ($T \leq 900K$).

Parameter	Start	Fitted	Error
a	13.0×10^6	9.56×10^6	0.04×10^6
b	19.0×10^4	5.47×10^4	0.5×10^4
c	41.0×10^5	9.56×10^6	Infinite
d	1400.0	264.0	Infinite
Sum of Squares $= 0.4 \times 10^{-9}$			

Table 6.1: Initial and fitted thermal coefficients for Pyroceram.

Table 6.1 shows the initial and the final values for the thermal coefficients that the fitting routine converged to. Using the fitted coefficient values, the thermal con-
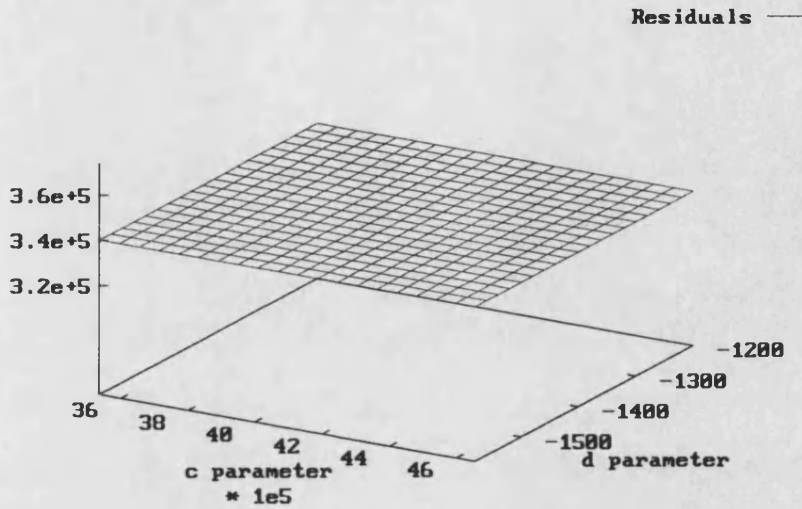
Residuals ———

Figure 6.9: Sum of square residual plot for the polaron contribution of Pyroceram.

ductivity derived using equation 6.4 can be compared to the TPRC recommended distribution [81], and both are shown in figure 6.10. Similarly, the temperature profile derived by the fitting routine is compared to the measured temperature profile in figure 6.11.
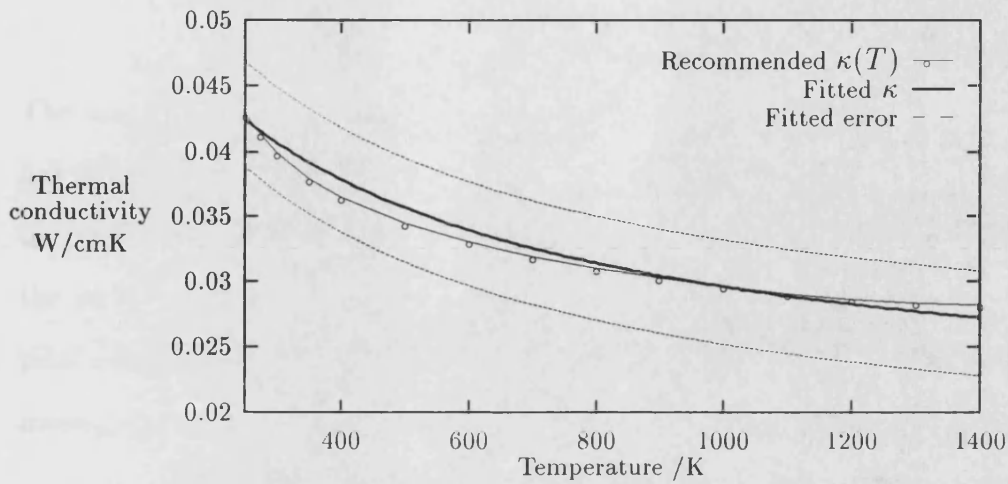
Figure 6.10: Comparison between the TPRC recommended conductivity for Pyroceram and that calculated from fitted coefficients.
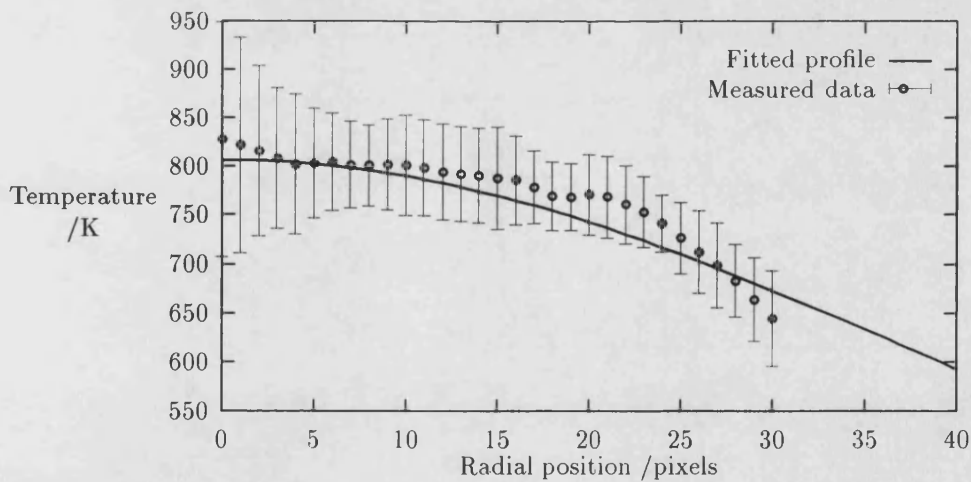
Figure 6.11: Comparison between measured data and that calculated from fitted thermal coefficients for Pyroceram.

6.2.2   Polycrystalline stoichiometric uranium dioxide.

The use of the actinide oxide UO_2 as a fuel in AGR and PWR nuclear reactors has stimulated considerable interest in the properties of this material. UO_2 in its unirradiated form presents no great safety hazard if handled correctly. However, the physical properties, and especially the thermal properties of irradiated fuel pins need to be known to model the effects of any reactor accidents. These measurements need to be made remotely.

Because of the interest in stoichiometric uranium dioxide, data for the thermal diffusivity measured by the laser flash method [82, 83] is readily available. From figure 6.12 it can be seen that the experimental data is well represented by the recommended diffusivity distribution [84]. This recommended distribution was
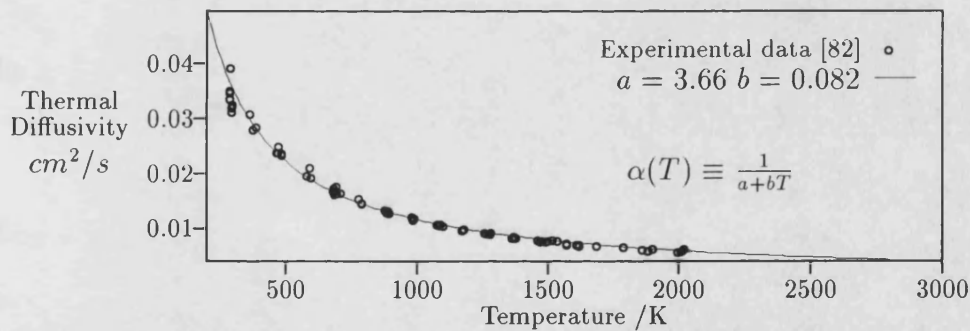
Figure 6.12: Recommended thermal diffusivity for UO_2 measured by the laser flash method.

used by the regression program, including an adjustment of the thermal diffusivity for the fractional porosity of the sample [82, 85].

The theoretical form of the thermal conductivity we have used is that recommended by Harding and Martin [73]. As the sample is polycrystalline, scattering from the grain boundaries would mask any four phonon effects, therefore the lattice contribution to the conductivity can be written:

$$\kappa_{latt}(T) \;=\; 1/(a + bT).\tag{6.5}$$

Below a temperature of 1500 K, experimental data [3,4] fits well to equation 6.5, and thus initial values for a and b are available.

As we are considering stoichiometric uranium dioxide, the fractional concentration of electrons and holes should be equal. This fact, used in conjunction with the equality of the hole and electron mobilities [5] results in an expression for the electrical conductivity shown in equation 6.6.

$$\sigma_{sp}(T) \;=\; \frac{V}{T}\,\exp(-W/kT).\tag{6.6}$$

The effect of the electrical conductivity on the thermal conductivity is given by the ambipolar contribution [86]:

$$\kappa_{elec}(T) \;=\; \frac{\sigma_{sp}}{4kT}\left[\frac{U}{e}\right]^{2}.\tag{6.7}$$

Here U represents the activation energy of electron-hole pairs. Comparing equations 6.6 and 6.7, the electronic contribution to the thermal conductivity can now be written:

$$\kappa_{elec}(T) \;=\; \frac{c}{T^{2}}\,\exp(-d/T).\tag{6.8}$$

Equations 6.5 and 6.8 are combined to give a total thermal conductivity expression of the form:

$$\kappa(T) \;=\; \frac{1}{(a + bT)} + \frac{c}{T^{2}}\exp(-d/T).\tag{6.9}$$
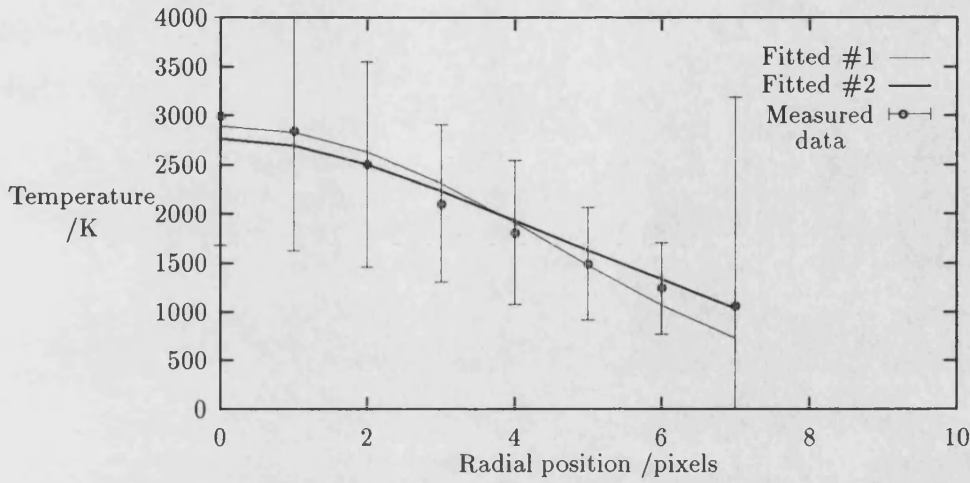
Figure 6.13: Comparison between measured data and that calculated from fitted thermal coefficients for UO_2 .

The values recommended by Harding and Martin [73] for the coefficients a, b, c and d were used as the starting point for the regression program. The fitted temperature profiles generated for two different gradient step lengths (denoted by *eta* [87]) are compared in figure 6.13 to the measured data set. The extracted thermal coefficients for both the fitted curves are shown in table 6.2.

	Fitted #1		Fitted #2		Starting values
a	1.733	$\pm$ 1.41	0.0813	$\pm$ 1.32	0.0375
b	0.369×10^{-3}	2.4×10^{-4}	0.324×10^{-3}	1.7×10^{-4}	2.165×10^{-4}
c	4.715×10^{9}	Infinite	4.715×10^{9}	Infinite	4.715×10^{6}
d	4.513×10^{5}	Infinite	5686	Infinite	16361
	Sum of squares = 7807.2		Sum of squares = 2881.7		

Table 6.2: Thermal coefficients extracted from the measured UO_2 temperature profile.

Several reasons can explain why the fitted temperature profiles do not exactly match the measured data, and why the extracted thermal coefficients show such

large uncertainties. The primary reason lies in the width of the measured temperature profile, which at eight pixels wide is too small to distinguish between slight changes in the fitted coefficients.
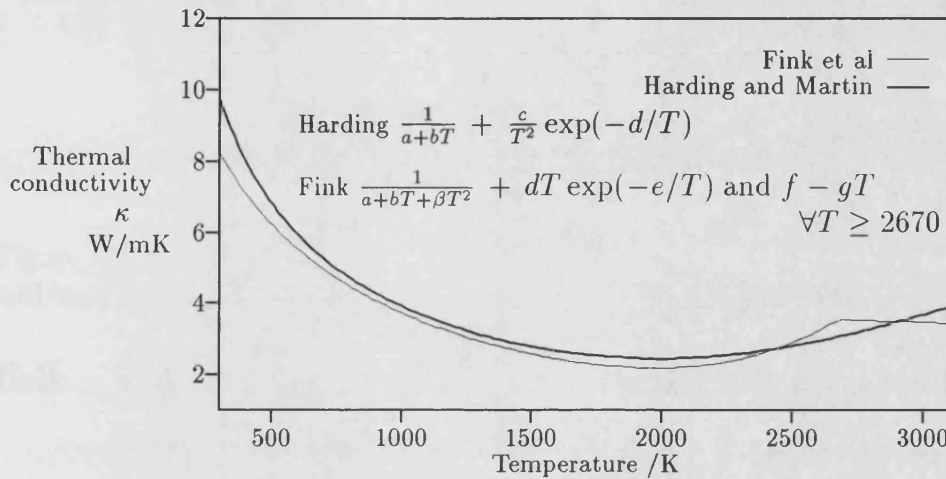
Figure 6.14: A comparison of recommended thermal conductivity values for UO_2
.

A secondary reason for the inaccuracy in the extracted thermal coefficients results from the magnitudes of the temperature generated on the sample. The peak temperature of 2994 K is below the melting point of UO_2 , but exceeds the temperature for 'Bredig' transition [88] which occurs at 84% of the melting point $(0.84T_m = 2610K)$ [89]. This transition has been attributed [90] to premelting of the oxygen sublattice, and therefore the finite element analysis program would need to be modified to incorporate this kind of phase transition, as well as modifying the predicted temperature dependence of the thermal conductivity to that recommended by Fink [91], shown in figure 6.14.
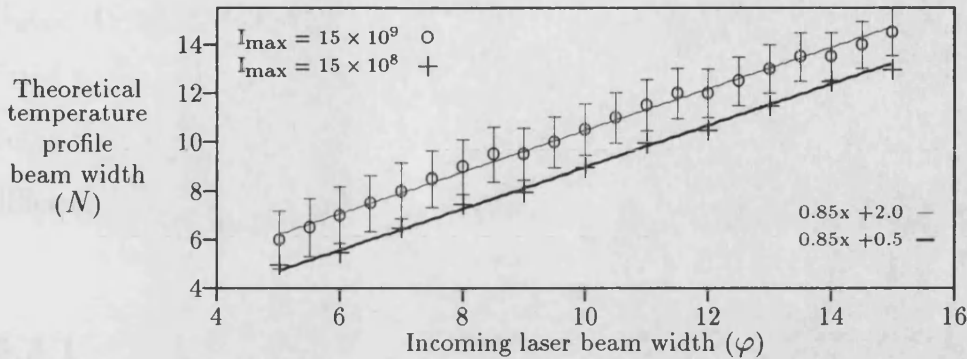
Figure 6.15: Relationship between beam width of theoretical temperature profile and input beam width.

6.3 Determination of heat conduction mechanism.

Whilst developing the finite element analysis program that calculates theoretical temperature distributions, it was noted that the theoretical temperature profiles were Gaussian in shape. This observation has already been applied to the measured radial temperature profiles shown in section 4.6. After fitting a Gaussian distribution ($Me^{-r^2/N}$) to the theoretical temperature profiles, it was found that the Gaussian beam width (N) was similar to the beam width of the incoming heat distribution (modeling a laser beam - $I_{max}e^{-r^2/\varphi}$) used by the finite element analysis (FEA) program.

The width of the 'theoretical' laser beam (φ) was varied, keeping the maximum intensity constant ($I_{max}=15 \times 10^9$); the dependence of the FEA temperature profile's beam width (N) with respect to the incoming beam width (φ) is shown

in figure 6.15, along with the results obtained for a different maximum intensity (I_{max}=15 × 10^8). It can be seen from figure 6.15 that a straight line can be fitted to the relationship between the two beam widths, with the gradient (0.85) being the same for the two different power settings, but with the y-axis intercepts differing (0.5 and 2.0).

6.3.1 Effect of the thermal coefficients on the beam width ratios.

In generating the theoretical temperature profiles described above, the finite element analysis program uses the thermal conductivity temperature dependence of UO_2 recommended by Harding and Martin (shown previously in equation 6.9). From this conductivity dependence, the thermal coefficients a and b are associated with lattice effects in the thermal conductivity, and the coefficients c and d are linked to the electronic or small polaron conduction of heat.

Using a maximum incident intensity of 15 × 10^9, the thermal coefficient a was varied from 0.001 to 0.125 whilst the other thermal coefficients were kept fixed. For each value of a, the linear dependence shown in figure 6.15 between the theoretical temperature profile's beam width (N) and the incoming laser's beam width (φ) was extracted by fitting to a straight line using a linear least squares regression method. The values for the gradient and intercept of the straight line obtained from the linear least squares analysis were then recorded as a function of the thermal coefficient being varied.
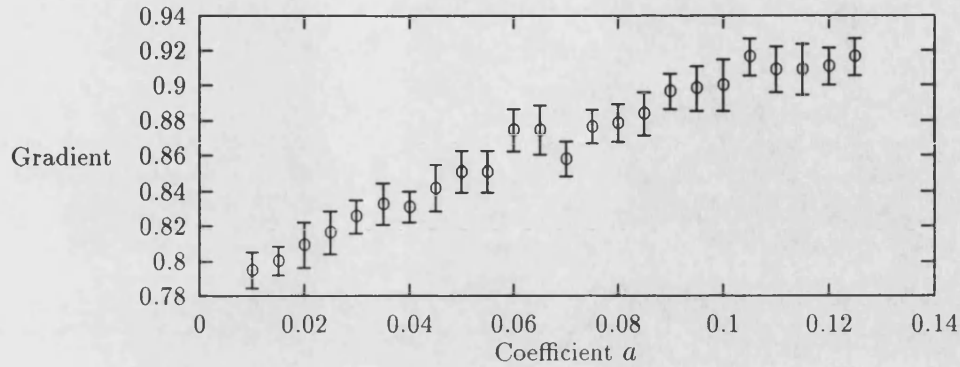
(a) Change of the beam width ratio's gradient with varying coefficient a
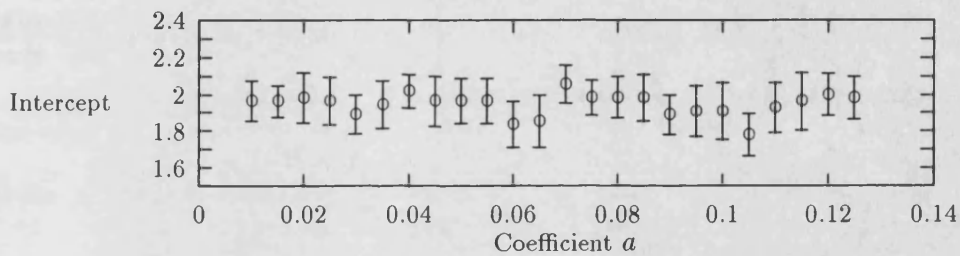
(b) Change of the beam width ratio's y-axis intercept with varying coefficient a

Figure 6.16: Effect of varying the thermal coefficient a on them width ratio's gradient and intercept.

Figure 6.16a shows how the gradient of the beam width ratios varies as a function of the thermal coefficient a, and figure 6.16b shows the dependence of the y-axis intercept on the coefficient a. Similarly, figure 6.17 shows how the beam width ratio's gradient and intercept varies as a function of b with the other thermal coefficients being held constant.

From figures 6.16 and 6.17 we can deduce that the lattice contribution to the thermal conductivity affects the gradient of the beam waist ratios leaving the
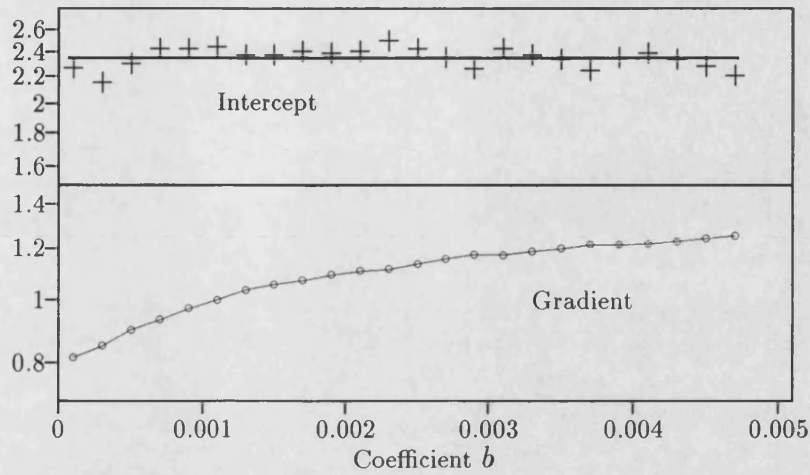
Figure 6.17: Effect of varying coefficient b on the gradient and intercept of the beam width ratio.

intercept constant, while figure 6.18 demonstrates that the electronic contribution affects the beam width ratio intercepts.

If we were to change the beam width of the heating laser used in our experiment, but keep the maximum intensity constant, it would be possible to isolate the mechanisms of heat conduction affected by external forces, such as applied pressure.
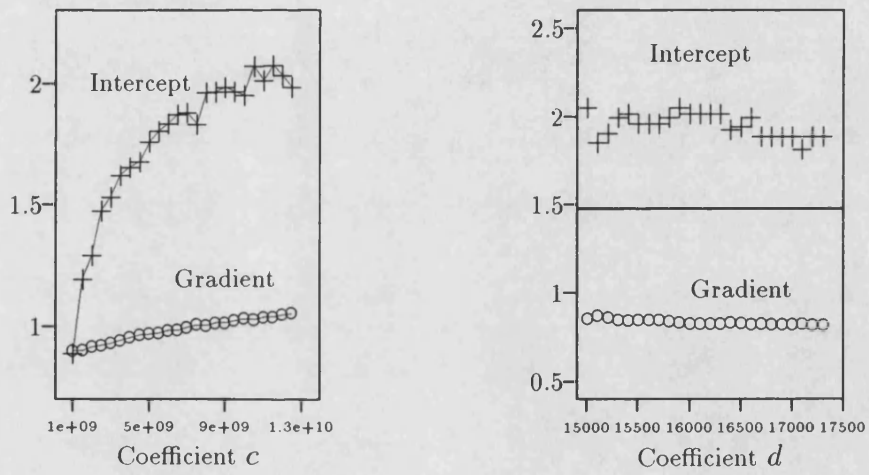
(a) Gradient and intercept variation with respect to thermal coefficient c.

(b) Gradient and intercept variation with respect to thermal coefficient d.

Figure 6.18: Effect of varying the c and d thermal coefficients on the gradient and intercept of the beam width ratio.

Chapter 7

Discussion of thermodynamic results obtained and conclusions.

The apparatus used to experimentally produce and measure radial temperature profiles has been described in part I of this thesis, along with the mathematical basis of the OMA2T computer analysis program. It has been demonstrated in section 4.5 that the melting points of materials can be measured remotely, with the measured melting points of polycrystalline samples of iron and uranium dioxide agreeing well with the published values. Hence this remote sensing capability now makes it possible to measure the solid-liquid phase transition as a function of pressure, extending the maximum obtainable pressures into the megabar region only obtainable using a diamond anvil cell (DAC). The Berkeley system [26] for obtaining melting points involves physical inspection of the sample quenched after heating, and then cross-referencing to the measured temperature profile to determine the melting point; determination of melting points directly from measured temperature profiles as described in this thesis does not involve the

inaccuracies introduced by cross-referencing the radius of the quenched melt to the recorded temperature profile.

Remote methods for accurately determining the melting point of a material are of particular interest, because this facilitates the measurement of the melting curve (melting point as a function of pressure). One of the first materials whose melting curve was closely studied was hydrogen which was of interest because of its simple electronic structure. Experimental study of the melting of hydrogen [92, 93] at medium pressures (P> 150 kbar) has found that the melting temperature and the volume of the solid can be related along the melting curve by an equation of the form:

$$V = A - B\ln(T_m). \tag{7.1}$$

This approach has been extended to simple metals, and analysis of the experimental melting curve data [94] for simple metals shows good agreement with equation 7.1. These experiments have been restricted to moderate pressure and temperatures due to the limitations of the apparatus and measurement techniques. The ranges of temperature and pressure could be extended by using modern techniques as described in this thesis, which would enable accurate comparison to theoretical predictions [95] based on Monte Carlo computer techniques. It is often more convenient to write equation 7.1 in the form,

$$\ln(T_m) = \ln(T_0) + \vartheta\frac{\Delta V_m}{V_0}, \tag{7.2}$$

where ϑ is an adjustable parameter, which is approximately constant for a given class of solids. The change in volume along the melting curve $(\Delta V_m/V_0)$ can be calculated from the applied pressure by Tait's equation of state [96] if the bulk

modulus B_m and its pressure derivative B'_m are known:

$$\frac{\Delta V}{V_0} = \frac{1}{B'_m + 1} \ln\left(1 + P\frac{B'_m + 1}{B_m}\right). \tag{7.3}$$

By combining equations 7.2 and 7.3 with the Clausius-Clapeyron equation, a scheme (Lindemanns Law) for determining the thermodynamic Grüneisen parameter (γ_{th}) from the accurate measurement of the pressure dependence of the melting point can be employed.

$$\frac{\partial \ln(T_m)}{\partial \ln(V_m)} = -2\gamma_{th} + \frac{2}{3}. \tag{7.4}$$

The accuracy of any method for determining the thermal properties of a material lies in the precise representation of the heat losses [97] in the mathematical solution of Fourier's law [98]. A well favoured technique for measuring the thermal conductivity of soft materials is the radial heat flow method [99], because the symmetry of the system reduces the mathematics of the problem to a one dimensional problem. The thermal conductivity can be calculated by measuring the temperature difference between two radial points when the sample has reached a steady state condition. Applying integral transform mathematics to the radial heat flow configuration (section 5.2), it has been shown that the thermal conductivity, diffusivity and loss parameter can be determined by fitting the temperature history curves measured at two radii to that predicted by the integral transform theory. To ensure accurate convergence of the fitting routine, sufficient data needs to be collected in the temperature history curves to ensure that the sample has reached its steady state distribution. Measurements made on a granular ceramic ($Y_2Ba_2CuO_5$) have produced temperature dependencies in the thermal conductivity and diffusivities which are consistent with strong

phonon-defect and phonon-phonon scattering. It is interesting to note that the temperature dependence of the loss parameter can be well represented by a T^4 dependence, which is consistent with heat loss by radiative transfer, as would be expected at high temperatures.

The measurement of the thermal properties of materials by the radial heat flow method has traditionally required electrical contact to be maintained with the sample. In part II of this thesis, a regression scheme for remotely determining the thermal coefficients related to the thermal conductivity of a material was described (section 5.4). Results obtained using this scheme were presented in section 6.2 for two contrasting materials. The first material studied (Pyroceram) has a well documented and understood thermal conductivity, with the scattering of phonons by grain boundaries and phonon-phonon interactions dominating the temperature dependence of the thermal conductivity. The regression method successfully converged to values for the thermal coefficients, which were then used to calculate the temperature dependence of the thermal conductivity. The thermal conductivity dependence replicates, within experimental error, the Thermophysical Properties Research Centre's (TPRC) recommended values.

The second material studied (stoichiometric uranium dioxide UO_2) has a thermal conductivity temperature dependence which is well documented but complicated. Grain boundary and phonon-phonon 'Umklapp' scattering processes dominate the conduction up to a temperature of 1500 K, above this, the effects of phonon scattering by small polarons becomes dominant. The existence of a 'phase' change (Bredig transition) around 2670 K has caused much contention as to the form the recommended thermal conductivity should take between 2670 K and the melt-

ing point due to the debate over the mechanisms causing this 'phase' change.
A thermal conductivity with a temperature dependence which incorporated the
effects of small polaron scattering, as well as the grain boundary and 'Umklapp'
effects, was used by the regression scheme used to determine the thermal coeffi-
cients related to the conductivity. Thermal coefficients were extracted from the
measured temperature profile, but the regression routine could not converge to a
global minimum, and produce an accurate result for UO_2 .

Comparison of the accuracies of the fitting to the expected thermal conductivities
of these two materials has highlighted some points that need to be considered in
any future work.

1. To extract the thermal coefficients from a measured radial temperature
   profile produced by laser heating a sample, the temperature profile needs
   to be wide enough to enable the regression routine to accurately identify
   the global minimum, and hence converge to the correct coefficients.

2. The processes contributing to the thermal conductivity should be well estab-
   lished from room temperature to the melting point. This criterion suggests
   that the regression technique is most suited to the investigation of the ther-
   mal properties of insulators, metals, and simple ionic materials, but falters
   when applied to materials with complex heat conduction mechanisms.

The need for a technique to measure the thermal conductivity of a material re-
motely can be justified by considering the implications the pressure dependence
of the thermal conductivity has on the understanding of the overall thermody-

namic properties of the material. For materials which can be classed as insulators, phonon-phonon and grain boundary scattering dominate the conduction of heat, especially at intermediate and high temperatures (T > 300 K > T_m). The pressure dependence of the thermal conductivity resulting from lattice effects alone has been measured [100], and takes the general form predicted by theory [101]:

$$-\frac{\partial \ln(\kappa_{latt})}{\partial \ln(V)} = 3\gamma_{th} + 2\frac{\partial \ln(\gamma_{th})}{\partial \ln(V)} + \lambda, \qquad (7.5)$$

where γ_{th} is the thermodynamic Grüneisen parameter, and λ is a constant related to the thermal properties of the material, usually unity.

When investigating the thermal conductivity of pure metals [21], the contribution of electrons to the total thermal conductivity needs to be considered, as the electron contribution will normally be approximately ten times greater than the lattice contribution for metals. As we are considering the conduction of heat at high temperatures, we can expect the Wiedemann-Franz law to be obeyed for simple metals. Therefore the pressure dependence of the electron thermal conductivity should be related to the pressure dependence of the electrical conductivity [102].

$$-\frac{\partial \ln(\kappa_e)}{\partial \ln(V)} = -\frac{\partial \ln(\sigma_e)}{\partial \ln(V)} \equiv A + 2\gamma_{th}. \qquad (7.6)$$

Distinguishing how the mechanisms of electron and lattice heat conduction manifest themselves in the total thermal conductivity is of great interest, but it is hard to achieve. By measuring the pressure derivative of the thermal conductivity at a given temperature, it might be possible to resolve the influences of the electron and lattice conduction methods [21], but only if the thermodynamic Grüneisen parameter is previously known.

Data exists for the temperature dependence of the thermal conductivity of uranium dioxide up to its melting point, but problems in fitting the measured thermal conductivity data to theories based around differing heat conduction mechanisms has led to dispute over the validity of these mechanisms. This discrepancy has occurred due to the experimental errors present in the measured thermal conductivity data at high temperatures. A method has been suggested in section 6.3 of this thesis to isolate the effects of external forces on the individual mechanisms involved in the conduction of heat. By studying the dependence of the width of the measured temperature profile as the width of the heating laser's focussed beam is varied, it has been shown that it is possible to distinguish between the electronic (κ_{elec}) and lattice (κ_{latt}) contributions to the total thermal conductivity. Further work is required to incorporate the effects of scattering by defect structures into the temperature dependence of the thermal conductivity. The effect of varying the heating laser's beam width on the width of the generated temperature profile can then be studied, and the characteristic dependencies of the gradient and the intercept of the beam waist ratio to the effect that defect structures have on the heat conduction can then be established.

To isolate the heat conduction mechanisms experimentally, the equipment used to remotely measure the temperature profiles described in chapter 2 of this thesis would need to be slightly modified. A variable magnification beam expander would need to be constructed so that a range of laser beam widths could be selected to be incident on the sample. This beam expander would take the place of the fixed magnification 10:1 beam expander shown in figure 2.1. The current supplied to the laser flashlamps would have to be adjusted in conjunction with the beam expander, to ensure that the maximum intensity incident on the sample

is constant for all of the variable laser beam widths. These modifications would enable the measurement of the gradient and intercept of the relationship between the two beam widths. Subjecting the sample to an external force, such as pressure or a magnetic field, the beam width ratio would then be recalculated. From the changes in the the gradient and intercept of the beam width ratio, the mechanisms of heat conduction affected by the external force can be isolated. For example, the presence of electron-phonon interactions have been studied by subjecting the sample to a magnetic field [103] and monitoring the reduction of the total conductivity. This method would be best applied to semiconductors [104], where the electron mobility is high, and the applied magnetic field has a significant effect on the electrical resistivity. Therefore, using the Wiedemann-Franz law to represent the electronic contribution to the thermal conductivity, the effect of an applied magnetic form on the thermal conductivity can be as shown in equation 7.7.

$$\kappa(B) \quad = \quad \frac{\mathcal{L}T}{\rho(B)} + \kappa_{latt}. \tag{7.7}$$

If the thermal conductivity of a metal were to be measured at low temperatures as a function of applied magnetic field, an effect similar to the De Haas van Alphen effect would be observed [105], which gives information about the material's Fermi surface.

In summary, the apparatus needed to remotely record a radial temperature distribution generated by a heating laser has been built and tested. Analysis of the recorded temperature profiles has made the determination of the melting points of materials by non-contact methods possible, with the measured melting points of polycrystalline iron and urania agreeing with the literature. Further analysis

of the recorded temperature profiles has also resulted in the temperature dependence of the thermal conductivity for the ceramic Pyroceram being obtained. With knowledge of the pressure dependence of the melting point and the thermal conductivity, the thermodynamical properties of a material can be better understood.

Appendix A

Integral Transform Techniques.

A.1 Homogeneous problem.

Start with the heat conduction equation, and boundary conditions equivalent to radiation into surroundings at a fixed temperature.

$$\nabla^2 T(\mathbf{r},t) = \frac{1}{\alpha}\frac{\partial T(\mathbf{r},t)}{\partial t} \qquad t>0 \tag{A.1}$$

with the relevant boundary and initial conditions;

$$k\frac{\partial T(\mathbf{r},t)}{\partial \mathbf{r}} + hT(\mathbf{r},t) = 0 \qquad t>0 \tag{A.2a}$$

$$T(\mathbf{r},t) = F(\mathbf{r}) \qquad t = 0 \tag{A.2b}$$

If we now separate the temperature into time and space variables;

$$T(\mathbf{r},t) = \psi(\mathbf{r})\Gamma(t)$$

$$\Rightarrow \frac{\nabla^2\psi(\mathbf{r})}{\psi(\mathbf{r})} = \frac{1}{\alpha}\frac{\partial\Gamma(t)}{\partial t}\cdot\frac{1}{\Gamma(t)} \tag{A.3}$$

The left-hand side is a function of $\mathbf{r}$ only, and similarly, the right-hand side is only a function of t. If equation A.3 is to be true, then both sides can be set equal to a constant.

$$\frac{\nabla^2\psi(\mathbf{r})}{\psi(\mathbf{r})} = -\lambda^2 = \frac{1}{\alpha\Gamma(t)}\frac{\partial\Gamma(t)}{\partial t} \tag{A.4}$$

The time dependent equation can be written as

$$\frac{\partial\Gamma(t)}{\partial t} + \lambda^2\alpha\Gamma(t) = 0 \tag{A.5a}$$

Which has solution of the form;

$$\Gamma(t) = e^{-\alpha\lambda^2 t} \tag{A.5b}$$

Similarly, the space equation can be written as the Helmholtz equation (eq. A.6);

$$\nabla^2\psi(\mathbf{r}) + \lambda^2\psi(\mathbf{r}) = 0 \tag{A.6}$$

This only has a solution for certain eigenvalues of λ, which then enables Helmholtz equation to be separated into ordinary differential equations, which can then be solved.

Once the eigenfunction $\psi_m(\mathbf{r})$ for the eigenvalues λ_m is evaluated, the solution for the temperature can be evaluated by;

$$T(\mathbf{r},t) = \sum_m C_m \, \psi_m(\mathbf{r}) \, e^{-\alpha\lambda_m^2 t} \tag{A.7}$$

To determine C_m put $t = 0$ into equation A.7, which then represents the temperature distribution at time $t = 0$, namely the Initial conditions.

$$F(\mathbf{r}) = \sum_m C_m \, \psi_m(\mathbf{r}) \tag{A.8}$$

If the orthogonal properties of eigenfunctions are used, namely;

$$\int_R \psi_m(\mathbf{r}) \, \psi_n(\mathbf{r}) \, \partial\mathbf{r} = 0 \qquad \forall \, m \neq n \tag{A.9a}$$

then,

$$\int F(\mathbf{r}) \, \psi_n(\mathbf{r}) \, \partial\mathbf{r} = \int \sum_m C_m \, \underbrace{\psi_m(\mathbf{r}) \, \psi_n(\mathbf{r})}_{=0 \, \forall \, m \neq n} \, \partial\mathbf{r} \tag{A.9b}$$

$$C_m = \frac{\int_R \psi_m(\mathbf{r}) \, F(\mathbf{r}) \, \partial\mathbf{r}}{\int_R \psi^2(\mathbf{r}) \, \partial\mathbf{r}} \tag{A.9c}$$

By then substituting into equation A.7, but using N as the normal of $\psi_m(\mathbf{r})$;

$$\Rightarrow T(\mathbf{r},t) = \sum_m \psi_m(\mathbf{r}) \frac{\int \psi_m(\mathbf{r}) \, F(\mathbf{r}) \, \partial\mathbf{r}}{N} \, e^{-\alpha\lambda_m^2 t} \tag{A.10}$$

If the eigenfunctions are normalised such that $\frac{\psi_m(\mathbf{r})}{\sqrt{N}} = K(\lambda_m, \mathbf{r})$ then;

$$T(\mathbf{r},t) = \sum_m K(\lambda_m,\mathbf{r}) \, e^{-\alpha\lambda_m^2 t} \cdot \int_R K(\lambda_m,\mathbf{r}) \, F(\mathbf{r}) \cdot \partial\mathbf{r} \tag{A.11}$$

Inspecting the integral in the equation A.11 , it is integrated with respect to $\mathbf{r}$, and therefore we can use the initial conditions to substitute $T(\mathbf{r}, t)$ for $F(\mathbf{r})$ as $F(\mathbf{r})$ is time independent.

$$\int_R K(\lambda_m, \mathbf{r}) F(\mathbf{r}) \partial \mathbf{r} \;=\; \int_R K(\lambda_m, \mathbf{r}) T(\mathbf{r}, t) \partial \mathbf{r} \;=\; \bar{T}(\lambda_m, t) \qquad \text{(A.12)}$$

Where $\bar{T}(\lambda_m, t)$ is the *Integral transform* of $T(\mathbf{r}, t)$, and $T(\mathbf{r}, t)$ can be subsequently determined by the *Inversion formula*;

$$T(\mathbf{r}, t) \;=\; \sum_m K(\lambda_m, \mathbf{r}) \bar{T}(\lambda_m, t) \qquad \text{(A.13)}$$

A.2 Non-homogeneous problem.

Now reconsider the original problem, but now with an arbitrary heat source;

$$\nabla^2 T(\mathbf{r}, t) + \frac{g(\mathbf{r}, t)}{\kappa} \;=\; \frac{1}{\alpha} \frac{\partial T(\mathbf{r}, t)}{\partial t} \qquad \text{t>0 in region R}$$

with boundary conditions on surface i;

$$k_i \frac{\partial T(\mathbf{r}, t)}{\partial \mathbf{r}} + h_i T(\mathbf{r}, t) \;=\; f_i(\mathbf{r}, t) \qquad \text{t>0} \qquad \text{(A.14a)}$$

$$T(\mathbf{r}, t) \;=\; F(\mathbf{r}) \qquad t = 0 \qquad \text{(A.14b)}$$

If we now apply the integral transform to the heat conduction problem above, and rearrange it, we arrive at;

$$\int_R K(\lambda_m, \mathbf{r}) \, \nabla^2 T(\mathbf{r}, t) \cdot \partial \mathbf{r} \;+\; \frac{\bar{g}(\lambda_m, t)}{\kappa} \;=\; \frac{1}{\alpha} \frac{\partial \bar{T}(\lambda_m, t)}{\partial t} \qquad \text{(A.15)}$$

where $\bar{g}(\lambda_m, t)$ is the integral transform of the heating term.

To evaluate the integral transform of $\nabla^2 T(\mathbf{r}, t)$, we have to use Greens' theorem which changes volume integrals into surface integrals.

$$\int_R K(\lambda_m, \mathbf{r}) \, \nabla^2 T(\mathbf{r}, t) \cdot \partial \mathbf{r} \;=\; \int_R T(\mathbf{r}, t) \nabla^2 K(\lambda_m, \mathbf{r}) \cdot \partial \mathbf{r} \qquad \text{(A.16)}$$

$$+ \; \sum_{i=1}^{s} \int_s K(\lambda_m, \mathbf{r}) \frac{\partial T(\mathbf{r}, t)}{\partial n} - T(\mathbf{r}, t) \frac{\partial K(\lambda_m, \mathbf{r})}{\partial n} \cdot \partial s$$

where n is the direction normal to s.

The first term on the RHS can be evaluated using Helmholtz equation, whilst the second is found by using the boundary conditions.

$$\int_R T(\mathbf{r}, t) \, \nabla^2 K(\lambda_m, \mathbf{r}) \cdot \partial \mathbf{r} \;=\; -\lambda^2 \, \bar{T}(\lambda_m, t) \qquad (A.17a)$$

$$K(\lambda_m, \mathbf{r}) \frac{\partial T(\mathbf{r}, t)}{\partial n} - T(\mathbf{r}, t) \frac{\partial K(\lambda_m, \mathbf{r})}{\partial n} \;=\; \frac{K(\lambda_m, \mathbf{r}) \, f_i(\mathbf{r}, t)}{k_i} \qquad (A.17b)$$

Substituting these results into Greens' theorem, and rearranging, we obtain a linear differential equation of the integral transform.

$$\frac{\partial \bar{T}(\lambda_m, t)}{\partial t} + \alpha \lambda_m^2 \bar{T}(\lambda_m, t) =: \frac{\bar{g}(\lambda_m, t)}{\kappa} + \sum_i \int_s \frac{K(\lambda_m, \mathbf{r}) \, f_i(\mathbf{r}, t)}{k_i} \cdot \partial s \qquad (A.18)$$

If we call the RHS of the equation above $A(\lambda_m, t)$, and let $\bar{F}(\lambda_m)$ be the integral transform of the initial conditions, then a solution to the linear differential equation is;

$$\bar{T}(\lambda_m, t) \;=\; e^{-\alpha \lambda_m^2 t} \left(\bar{F}(\lambda_m) + \int_0^t e^{\alpha \lambda^2 t} \, A(\lambda_m, t) \cdot \partial t \right) \qquad (A.19)$$

Therefore to find the solution to the temperature distribution, we have to apply the inversion formula to $\bar{T}(\lambda_m, t)$ as found above. All that remains is to find a suitable form of the eigenfunction solution to Helmholtz equation. The boundary
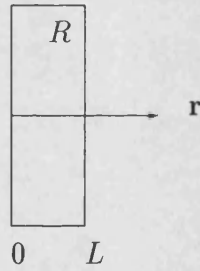
Figure A.1: Schematic diagram of a 'thin' slab.

conditions for the homogeneous system above are;

$$-k_1 \frac{\partial \psi(\mathbf{r})}{\partial \mathbf{r}} \;+\; h_1 \psi(\mathbf{r}) = 0 \qquad \mathbf{r}=0 \qquad (A.20a)$$

$$k_2 \frac{\partial \psi(\mathbf{r})}{\partial \mathbf{r}} \;+\; h_2 \psi(\mathbf{r}) = 0 \qquad \mathbf{r}=L \qquad (A.20b)$$

One particular solution is $\psi_m(\mathbf{r}) = a\cos(\lambda_m\mathbf{r}) + b\sin(\lambda_m\mathbf{r})$. By applying the boundary conditions at L and 0, we obtain the solution for the eigenvalues, where $\lambda_m = m^{th}$ positive root of;

$$Tan(\lambda L) = \frac{\lambda(H_1 + H_2)}{\lambda^2 - H_1 H_2} \tag{A.21}$$

where $H_i = \frac{h_i}{k_i}$.

Therefore the eigenfunction solution we are looking for is;

$$\psi_m(\mathbf{r}) = \cos(\lambda_m\mathbf{r}) + \frac{H_1}{\lambda_m}\sin(\lambda_m\mathbf{r}) \tag{A.22}$$

but the normalised solution $K(\lambda_m, \mathbf{r})$ requires evaluation of the norm.

$$N = \int_0^L \psi^2(\mathbf{r}) \cdot \partial\mathbf{r} \tag{A.23}$$

This has been evaluated by Carslaw and Jaeger [72], and becomes;

$$N = \frac{1}{2}\left[\frac{\lambda_m^2 + H_1^2}{\lambda_m^2} \cdot \left(L + \frac{H_2}{\lambda_m^2 + H_2^2}\right) + \frac{H_1}{\lambda_m^2}\right] \tag{A.24}$$

References

[1] M Kurzmann V Stöhr J Tochtrop and R Kassing. Interferometric measurement of thermal expansion. *Mater.Sci. and Eng.*, A122:117, 1989.

[2] R W Ostensen. A sensitivity study on the damage potential of a LMFBR core disassembly. *Nucl. Technol.*, 43:301, 1979.

[3] A B G Washington. Preferred values for the thermal conductivity of sintered ceramic fuel for fast reactor use. *UKAEA report*, TRG-2236(D), 1973.

[4] G Brandt, R Haufler and G Neuer. Thermal conductivity and emittance of solid UO_2. *CINDAS Purdue University, West Lafayette*, 1976.

[5] G J Hyland. Thermal-conductivity of solid UO_2 - Critique and recommendation. *J.Nuc.Mater.*, 113:125, 1983.

[6] W Marshall. *Nuclear power technology*. Clarendon Press, Oxford, 1983.

[7] W Schroter and J Nolting. Specific heat of crystals with the fluorite structure. *J.Phys.Colloq.*, 41(C6):20, 1980.

[8] A S Dworkin and M A Bredig. Heat content and entropy of strontium chloride from 298 K to 1200 K. *J.Chem.Eng.Data*, 8:416, 1963.

[9] K Naito. High temperature heat capacities of UO_2 and doped UO_2. *J.Nuc.Mater.*, 167:30, 1989.

[10] P J D Lindan and M J Gillan. A molecular dynamics study of the thermal conductivity of CaF_2 and UO_2. *J.Phys.:Condens.Matter*, 3:3929, 1991.

[11] Hampton R N H Saunders G A Harding J H and A M Stoneham. The pressure dependence of the dielectric constant and electrical conductivity of single crystal uranium dioxide. *J.Nuc.Mater.*, 150:17, 1987.

[12] C R A Catlow. Recent problems and progress in the study of UO_2 and mixed UO_2-PuO_2. *J.Chem.Soc.,Faraday Trans. 2*, 83:1065, 1987.

[13] G J Hyland and R W Ohse. The heat-capacity and enthalpy of condensed UO_2 - critical review and assessment. *J.Nuc.Mater.*, 140(2):149, 1986.

[14] R A Jackson et al. The calculation of defect parameters in UO_2. *Philos. Mag. Part-A*, 53(1):27, 1986.

[15] C J Glassbrenner and G A Slack. Thermal conductivity of silicon and germanium from 3 K to the melting point. *Phys.Rev.*, 134(4A):1058, 1964.

[16] R Berman. Heat conduction in non-metallic crystals. *Sci.Prog.Oxf.*, 55:537, 1967.

[17] D R Nysten B Issi J P Barton R Boyington and J G Lavin. Determination of lattice defects in carbon fibers by means of thermal-conductivity measurements. *Physical Review B*, 44(5):2142, 1991.

[18] N Wiser. Electron-electron scattering and the heat transport properties of metals. *High Temperature-High Pressure*, 21:25, 1989.

[19] N W Ashcroft and N D Mermin. *Solid State Physics.* Saunders College, Philadelphia, 1976.

[20] P Jacobsson and B Sundqvist. Pressure dependence of the thermal and electrical conductivities of intermetallic compounds $AuCu$ and $AuCu_3$. *J.Phys.Chem.Solids*, 49(4):441, 1988.

[21] B Sundqvist. The thermal conductivity of metals under pressure. *Mat.Res.Soc.Symp.Proc.*, 22:261, 1984.

[22] J M Ziman. *Electrons and phonons.* Oxford Univ. Press, Oxford, 1960.

[23] S Andersson and G Bäckstrom. The thermal conductivity and heat capacity of single crystal Si under hydrostatic pressure. *J.Phys.C: Solid State Phys.*, 21:3727, 1988.

[24] A B Lincoln R C Donaldson and R C Heckman. High temperature thermal diffusivity measurement by a negative pulse technique. *J.Appl.Phys.*, 45(5):2321, 1974.

[25] R G Ross and P Andersson. Thermal conductivity and heat capacity of ammonium halides under pressure:NH_4Br, NH_4I and a comparison with NH_4Cl. *J.Phys.C: Solid State Phys.*, 20:4745, 1987.

[26] R Jeanloz. Physical chemistry at ultrahigh pressures and temperatures. *Ann.Rev.Phys.Chem.*, 40, 1989.

[27] A Jayaraman. Diamond anvil cell and high pressure physical investigations. *Rev. Sci.Instrum.*, 55:65–108, 1983.

[28] X Y Li and R Jeanloz. Phases and electrical conductivity of a hydrous silicate assemblage at lower-mantle conditions. *Nature*, 350(6316):332, 1991.

[29] E Knittle and R Jeanloz. Synthesis and equation of state of (Mg,Fe)SiO_3 perovskite to over 100 gigapascals. *Science*, 235:668, 1987.

[30] D C O'Shay. *Elements of Modern Optical Design*. Wiley, New York, 1985.

[31] F L Pedrotti and L S Pedrotti. *Introduction to Modern Optics*. Prentice-Hall International, London, 1987.

[32] R Jeanloz and D L Heinz. Experiments at high temperatures and pressure: Laser heating through the diamond cell. *Journal de Physique*, 45(C8), 1984.

[33] E Hecht. *Optics*. Addison-Wesley, Reading, Massachusetts, 2 edition, 1989.

[34] K D Mielenz et al. *Applied Optics*, 7:89, 1968.

[35] International Committee of Weights and Measures. Secondary standards for use in spectroscopy. *Trans. IAU*, XII A, 1965.

[36] National Physical Laboratory. *Certificate of Calibration*. Reference Number 127460/0P3.

[37] M G Cox. A survey of numerical methods for data and function approximation. In *The State of the Art in Numerical Analysis.*, page 627. Academic Press, London, 1977.

[38] P M Hemley, R J Bell and H K Mao. Laser techniques in high-pressure geophysics. *Science*, 237(4815):605, 1987.

[39] A Jayaraman. Ultrahigh pressures (review article). *Rev. Sci.Instrum.*, 57:1013–1031, 1986.

[40] G J Piermarini et al. Calibration of the pressure dependence of the R_1 ruby fluorescence line to 195 kbar. *J.Appl.Phys.*, 46(6):2774, 1975.

[41] Y Sato-Sorensen. Measurements of the lifetime of the ruby R_1 line and its application to high temperature and high pressure calibration in the diamond anvil cell. In M H Manghnani and Y Syono, editors, *High Pressure Research in Mineral Physics*, page 53. American Geopyhsical Union, Washington D.C., 1987.

[42] Y M Gupta and X A Shen. Potential use of the ruby R_2 line shift for static high pressure calibration. *Appl.Phys.Lett.*, 58(6):583, 1991.

[43] N J Hess and D Schiferl. Pressure and temperature dependence of laser-induced fluorescence of Sm:YAG to 100 kbar and 700°C and an empirical model. *J.Appl.Phys.*, 68(5):1953, 1990.

[44] A Lacam and C Chateau. High pressure measurements at moderate temperatures in a diamond anvil cell with a new optical sensor: $SrB_4O_7:Sm^{2+}$. *J.Appl.Phys.*, 66(1):366, 1989.

[45] P A Jansson. *Deconvolution, with applications in spectroscopy*. Academic Press, New York, 1984.

[46] S R Deans. *The Radon Transform and some of its Applications*. Wiley Interscience, New York, 1983.

[47] J Radon. Über die bestimmung von funktionen durch ihre integralwerte längs gewisser manningfaltigkeiten. *Berichte Sächsische Akademie der Wissenshaften.*, 69:262–267, 1917.

[48] M Kalal and K A Nugent. Abel inversion using fast Fourier transforms. *Applied Optics*, 27(10):1956, 1988.

[49] C D Macdonado and H N Olsen. New method for obtaining emission coefficients from emitted spectral intensities. *J.Opt.Soc.Am.*, 56(10):1305, 1966.

[50] J Dong and R J Kearney. Symmetrizing, filtering and Abel inversion using fourier transform techniques. *J.Quant.Spectrosc.Radiat.Transfer*, 46(3):141, 1991.

[51] E W Hansen and P Law. Recursive methods for computing the Abel transform and its inverse. *J. Opt. Soc. Am.*, 2(4):510–520, 1985.

[52] M P Freeman and S Katz. Determination of a radiance-coefficient profile from the observed asymmetric radiance distribution of an optically thin radiating medium. *J.Opt.Soc.Am.*, 53(10):1172, 1963.

[53] R N Bracewell. *The Fourier Transform and its Applications*. McGraw-Hill, New York, 2 edition, 1971.

[54] O H Nestor and H N Olsen. Numerical methods for reducing line and surface probe data. *SIAM rev.*, 2:200–207, 1960.

[55] P Ding, M Yingkui and P Shofu. An interpolation solution of the Abel transformation for use in optically thick cylindrically symmetric plasmas. *J.Quant.Spectosc.Radiat.Transfer*, 45(2):115, 1991.

[56] C J Cremers and R C Birkebak. Application of the Abel integral equation to spectroscopic data. *Applied Optics*, 5(6):1057–1064, 1964.

[57] H Brunner. The numerical solution of a class of Abel integral equations by piecewise polynomials. *J.Comp.Phys.*, 12:412, 1973.

[58] K Bockasten. Transformation of observed radiances into radial distribution of the emission of the plasma. *J. Opt. Soc. Am.*, 51(9):943–947, 1961.

[59] W L Barr. Method for computing the radial distribution of emitters in a cylindrical source. *J. Opt. Soc. Am.*, 52:885–888, 1962.

[60] E T Whittaker and G N Watson. *A course in modern analysis*. The Macmillan Company, New York, 1948.

[61] C W Clenshaw. Curve fitting with a digital computer. *Comp.J.*, 2:170, 1960.

[62] R Piessens. Calculation of the radial distribution of emitters in a cylindrical source. *Comp.Phys.Comm.*, 5:294, 1973.

[63] G W C Kaye and T H Laby. *Tables of Physical and Chemical constants and some mathematical functions*. Longman, London, 15 edition, 1986.

[64] R P Weast. *Handbook of Chemistry and Physics. Ready reference book of chemical and physical data*. CRC Press Inc., Cleveland, Ohio, 57 edition, 1976.

[65] M H Rand et al. The thermodynamic properties of the urania phase. *Rev.Int.Hautes.Refact.*, 15:355, 1978.

[66] T Sato. Spectral emissivity of silicon. *Jpn.J.Appl.Phys.*, 6(3):339, 1967.

[67] V V Mirkovich. The measurement of thermal diffusivity by three methods. *Proc.3rd.ICTA, Davos*, Thermal Analysis, Vol 1:525, 1971.

[68] R C Heckman. Finite pulse-time and heat-loss effects in pulse thermal diffusivity measurements. *J.Appl.Phys.*, 44(4):1455, 1973.

[69] G Eichler, H Salje and H Stahl. Thermal diffusion measurements using spatially periodic temperature distributions induced by laser light. *J.Appl.Phys.*, 44(12):5383, 1973.

[70] M N Ozişik. *Boundary value problems of heat conduction*. International Textbook Company, Scranton,Pennsylvania, 1968.

[71] A Ångström. *Ann.Physik.Lpz*, 114:513, 1861.

[72] H S Carslaw and J C Jaeger. *Conduction of heat in solids.* Oxford University Press, New York, 2 edition, 1959.

[73] J H Harding and D G Martin. A recommendation fot the thermal conductivity of uranium dioxide. *J.Nucl.Mater.*, 166:223, 1989.

[74] D F Elliott and K R Rao. *Fast Transforms: Algorithms, Analyses, Applications.* Academic Press, New York, 1982.

[75] A H Harker. Private communication, September 1991.

[76] W J Parker et al. Flash method of determining thermal diffusivity, heat capacity, and thermal conductivity. *J.App.Phys.*, 32(9):1679, 1961.

[77] F Righini and A Cezairliyan. Pulse method of thermal diffusivity measurements (A review). *High Temperatures - High Pressures*, 5:481, 1973.

[78] J C Weilbacher. Diffusivité thermique de l'oxide d'uranium et de l'oxide de thorium à haute température. *High Temperatures - High Pressures*, 4:431, 1972.

[79] O A Troitskii and S Z Shmurak. Distribution of infrared absorption bands in the spectrum of crystallising glasses in the region of absorption by water. *Russ.J.Phys.Chem.*, 40(6):701, 1966.

[80] H W Flieger. The thermal diffusivity of Pyroceram at high temperatures. *Proc.3rd.Conf.on Thermal Conductivity*, Oct.(16–18):769, 1963.

[81] C Y Touloukin Y S Powell, R W Ho and P G Klemens, editors. *Thermophysical properties of matter, the TPRC data seris. Thermal conductivity*, volume 2, page 939. Plenum, New York, 1970.

[82] M Hirai. Thermal diffusivity of UO_2-Gd_2O_3 pellets. *J.Nuc.Mater.*, 173:247, 1990.

[83] S D Preston et al. Thermal diffusivities and thermal conductivity of UO_2 and $U_{1-x}Gd_xO_2$ solid solutions. *High Temperatures - High Pressures*, 21:287, 1989.

[84] Y S Touloukin and C Y Ho, editors. *Thermophysical properties of matter, the TPRC data seris. Thermal diffusivity*, volume 10, page 402. Plenum, New York, 1973.

[85] D G Martin. A reappraisal of the thermal-conductivity of UO_2 and mixed (U,Pu) oxide fuels. *J.Nuc.Mater.*, 110(1):73, 1982.

[86] I T Collier et al. Electrical conductivity of polycrystalline uranium dioxide. *J.Nuc.Mater.*, 168:268, 1989.

[87] Numerical Algorythms Group. *E04FCF* -NAG *Fortran library routine document*. Reference Number NAGFLIB:1652/0:Mk11.

[88] M A Bredig. The order-disorder (lambda) transition in uranium dioxide: calculation of the Frenkel energy. *Colloq.Int.CNRS*, 205:183, 1971.

[89] J Ralph. Recent developments in the study of the high temperature thermophysical properties of UO_2. *Nucl.Energy*, 26(4):259, 1987.

[90] K Clausen et al. Investigation of oxygen disorder, thermal parameters, lattice-vibrations and elastic-constants of UO_2 and ThO_2 at temperatures up to 2930 K. *Revue de Physique Appliquee*, 19(9):719, 1984.

[91] M G Fink, J K Chasanov and L Leibowitz. Thermo-physical properties of uranium-dioxide. *J.Nuc.Mater.*, 102(1-2):17, 1981.

[92] V V Kechin et al. Melting curve of hydrogen up to 10 kbar. *Sov.Phys.JETP*, 45(1):182, 1977.

[93] V Diatschenko et al. Melting curves of molecular hydrogen and molecular deuterium under high pressures. *Phys.Rev.B*, 32(1):381, 1985.

[94] V V Kechin. The melting law at high pressures. *High Temperatures - High Pressures*, 21:297, 1989.

[95] D A Moriarty, J A Young and M Ross. Theoretical study of the aluminium melting curve to very high pressure. *Phys.Rev.B*, 30(2):578, 1984.

[96] J R MacDonald. Review of some experimental and analytical equations of state. *Rev.Mod.Phys.*, 41:316, 1969.

[97] L M Clark and R E Taylor. Radiation loss in the flash method for thermal diffusivity. *J.Appl.Phys.*, 46(2):714, 1975.

[98] D A Watt. Theory of thermal diffusivity by pulse technique. *Brit.J.Appl.Phys.*, 16:231, 1966.

[99] C J Glassbrenner. High temperature, small diameter, radial heat flow thermal conductivity apparatus. *Rev.Sci.Instrum.*, 36(7):984, 1965.

[100] S Andersson and G Bäckström. The thermal conductivity and heat capacity of single-crystal Si under hydrostatic pressure. *J.Phys.C:Solid State Phys.*, 21:3727, 1988.

[101] G A Slack. The thermal conductivity of nonmetallic crystals. *Solid State Physics*, 34:316, 1969.

[102] L Bohlin. Thermal conduction of metals at high pressure. *Solid State Commun.*, 19:389, 1976.

[103] G K White and S B Woods. The thermal and electrical resistivity of bismuth and antimony at low temperatures. *Phil.Mag.*, 3:342, 1958.

[104] D Armitage and H J Goldsmid. The thermal conductivity of cadmium arsenide. *J.Phys.C: Solid State Phys.*, 2:2139, 1969.

[105] M C Steele and J Babiskin. Oscillatory thermomagnetic properties of a bismuth single crystal at liquid helium temperatures. *Phys.Rev.*, 98:359, 1955.